

1 **Measurement of Tagged Deep Inelastic**  
2 **Scattering (TDIS)**

3  
4 May 18, 2015

5 **Hall A and SBS Collaboration Proposal**

6 Dasuni Adikaram, Alexandre Camsonne, Dave Gaskell, Doug Higinbotham, Mark Jones,  
7 Cynthia Keppel (Spokesperson)<sup>1</sup>, Wally Melnitchouk, Christian Weiss, Bogdan  
8 Wojtsekhowski (Spokesperson)  
9 *JEFFERSON LAB*

10 John Arrington, Roy Holt, Paul Reimer  
11 *ARGONNE NATIONAL LAB*

12 Paul King (Spokesperson), Julie Roche  
13 *OHIO UNIVERSITY*

14 Krishna Adhikari, Jim Dunne, Dipangkar Dutta (Spokesperson), Lamiaa El-Fassi,  
15 and Li Ye  
16 *MISSISSIPPI STATE UNIVERSITY*

17 Charles Hyde, Sebastian Kuhn, Lawrence Weinstein  
18 *OLD DOMINION UNIVERSITY*

19 John Annand (Spokesperson), David Hamilton, Derek Glazier, Dave Ireland, Kenneth  
20 Livingston,  
21 Ian MacGregor, Bryan McKinnon, Bjoern Seitz, Daria Sokhan  
22 *UNIVERSITY OF GLASGOW*

23 Jen-Chieh Peng  
24 *UNIVERSITY OF ILLINOIS AT URBANA CHAMPAIGN*

25 Gordon Cates, Kondo Gnanvo, Richard Lindgren, Nilanga Liyanage, Jixie Zhang  
26 (Spokesperson)  
27 *UNIVERSITY OF VIRGINIA*

28 Todd Averett, Keith Griffeon  
29 *COLLEGE OF WILLIAM AND MARY*

30 Tim Hobbs, Thomas Londergan  
31 *INDIANA UNIVERSITY*

32 Xiaodong Jiang  
33 *LOS ALAMOS NATIONAL LABORATORY*

34 Michael Christy, Narbe Kalantarians, Michael Kohl, Peter Monaghan, Liguang Tang  
35 *HAMPTON UNIVERSITY*

36 Ioana Niculescu, Gabriel Niculescu  
37 *JAMES MADISON UNIVERSITY*

38 Boris Kopeliovich, Nuruzzaman, I. Potashnikova  
39 *UNIVERSIDAD TECNICA FEDERICO SANTA MARIA*

40 Andrew Puckett  
41 *UNIVERSITY OF CONNECTICUT*

42 Garth Huber  
43 *UNIVERSITY OF REGINA*

---

<sup>1</sup>Contact person

## Abstract

We propose to investigate tagged deep inelastic scattering (TDIS) by measuring high  $W^2$ ,  $Q^2$  electrons scattered from hydrogen and deuterium targets in coincidence with low momentum recoiling protons. This is a pioneering experiment that will probe the elusive mesonic content of the nucleon, using the tagging technique to scatter for example from the pion in proton to pion fluctuations. This approach will also provide access to the pion structure function via the Sullivan process.

The experiment utilizes the Hall A Super BigBite spectrometer for electron detection, in conjunction with a low density target, and, a radial time projection chamber (RTPC) with GEM-based readout, inside a large diameter 5T solenoid. These combined systems, along with the CEBAF high current CW beam, leverage the high luminosity and unique kinematics required to access the proposed physics.

The low momentum tagging technique is crucial for the experimental separation of competing processes, leading to the isolation of the electron-meson scattering contribution. The  $D(e, e'np)$  process will be used to calibrate the RTPC, allowing absolute TDIS cross section measurement. The low density target, as demonstrated in BONuS, will allow the use of an effective free neutron target, essential for the study of the virtual photon - charged meson interaction, which has significant advantage for theoretical interpretation. Complementary data on the neutral meson interaction will also be collected for the first time.

# 64 Contents

65	<b>1</b>	<b>Physics Motivation</b>	<b>5</b>
66	1.1	Tagged Deep Inelastic Scattering (TDIS) . . . . .	12
67	1.1.1	Predictions of a Pion Cloud Model . . . . .	12
68	1.2	Extraction of the Pion Structure Function . . . . .	16
69	1.3	Dyson-Schwinger Equation Inspired Models . . . . .	16
70	1.3.1	Corrections to the Extraction of Pion Structure Function . . . . .	18
71	1.3.2	Comparison of Neutron and Proton Data . . . . .	21
72	1.4	Impact for the Jefferson Lab 12 GeV Program and Beyond . . . . .	22
73	1.5	Physics Motivation Summary . . . . .	23
74	<b>2</b>	<b>Experiment</b>	<b>25</b>
75	2.1	Overview . . . . .	25
76	2.2	Experiment Luminosity . . . . .	25
77	2.2.1	Accidental Rates . . . . .	26
78	2.3	Recoil Detector . . . . .	30
79	2.3.1	Target cell . . . . .	35
80	2.3.2	RTPC Calibration . . . . .	35
81	2.4	The Super Bigbite Spectrometer . . . . .	38
82	2.4.1	CLAS6 Large Acceptance Calorimeter . . . . .	39
83	2.4.2	Super Bigbite Trigger and DAQ . . . . .	41
84	2.5	Simulations of the Radial Time Project Chamber . . . . .	43
85	2.5.1	Kinematics . . . . .	50
86	<b>3</b>	<b>Projected Results</b>	<b>53</b>
87	3.1	Beam Time Request . . . . .	56
88	3.2	Expected Experimental Accuracy . . . . .	58
89	<b>4</b>	<b>Summary</b>	<b>58</b>
90	<b>A</b>	<b>A Phenomenological Model of Tagged Deep Inelastic Scattering</b>	<b>60</b>
91	A.0.1	Meson Cloud Contributions to Inclusive DIS . . . . .	60
92	A.0.2	Tagged Structure Functions . . . . .	62

# 1 Physics Motivation

The concept of a composite nucleon structure may be tracked as far back as 1933 to the discovery of the anomalous magnetic moment of the proton [1]. This was explicitly formulated by Fermi and Marshall who noted in a 1947 paper [2] that experimental evidence pointed to the nucleon existing approximately 20% of the time in a virtual meson-nucleon state. The virtual meson "cloud" of the nucleon plays an important role in the understanding of the nucleon-nucleon interaction and the pion cloud in particular has always been considered critical to understanding the nucleon's long-range structure. At shorter ranges, the role of mesons in electron-nucleon deep inelastic scattering (DIS) have also been investigated. In 1972 Sullivan [3] suggested that some fraction of the nucleon's anti-quark sea distribution may be associated with this pion content of the nucleon. For many decades these and numerous other theories that describe and/or utilize the meson cloud of the nucleon have advanced significantly (see [4, 5, 6] for some review). From partially conserved axial current to the success of chiral quark models, it is considered known that the nucleon has an associated meson cloud. In very stark contrast to the substantial body of theory associated with the meson cloud, however, experimental results remain few and far between. In a 1983 paper, Thomas commented that "...it is rather disturbing that no one has yet provided direct experimental evidence of a pionic component in the nucleon" [7]. Even with results becoming available from Drell-Yan experiments at Fermilab, W production at RHIC, and diffractive DIS at HERA and COMPASS, all discussed below, the "disturbing" situation is not yet been substantially improved.

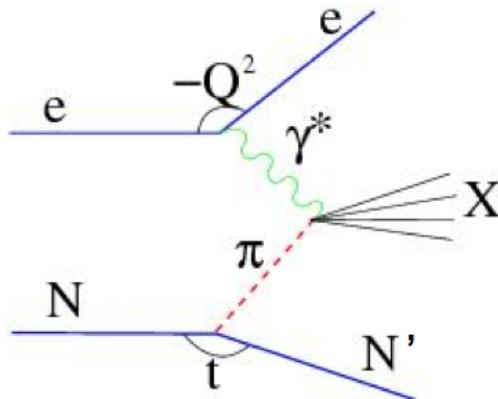


Figure 1: Feynman diagram for electron scattering from the pion cloud of the nucleon  $N$ , with the initial nucleon at rest (the Sullivan process).

The 12 GeV upgrade of JLab presents new opportunities to study the mesonic structure of the nucleon. One such technique is to measure the contribution to electron Deep Inelastic Scattering (DIS) off the meson cloud of a nucleon target, as pointed out by Sullivan [3] (Fig. 1). This so-called Sullivan process was shown to persist even at large  $Q^2$  scales. An immediate consequence of the Sullivan process is that the nucleon parton distributions contain a component which can be attributed to the meson cloud. This

121 intriguing idea remained untested for many years. In the early 1980s, Thomas [7] pre-  
 122 dicted several implications of the Sullivan process for nucleon parton distributions using  
 123 a cloudy-bag model for describing the meson cloud. In particular, it was predicted that  
 124 the nucleon sea should have an up/down sea-quark flavor asymmetry, as well as an  $s/\bar{s}$   
 125 asymmetry for the strange quark sea. The earliest parton models assumed that the proton  
 126 sea was flavor symmetric, even though the valence quark distributions are clearly flavor  
 127 asymmetric. The assumption of flavor symmetry was not based on any known physics,  
 128 and it remained untested by experiments. A direct method to check this assumption is to  
 129 compare the sea in the neutron to that in the proton by measuring the Gottfried integral  
 130 in DIS. The Gottfried Sum Rule (GSR) gives the following relation for the proton and  
 131 neutron structure functions  $F_2^p$  and  $F_2^n$ :

$$I_{\text{GSR}} = \int_0^1 [F_2^p(x) - F_2^n(x)]/x dx = \frac{1}{3} + \frac{2}{3} \int_0^1 [\bar{u}(x) - \bar{d}(x)] dx = \frac{1}{3}. \quad (1)$$

132 In the early 1990s, the NMC collaboration reported [8] an observation of the violation of  
 133 the GSR[9],  $I_{\text{GSR}} = 0.235 \pm 0.026$ . Since the GSR is derived under the assumption of  
 134  $\bar{d}(x) = \bar{u}(x)$ , the NMC result strongly suggests that this assumption is invalid. Indeed,  
 135 Eq. 1 and the NMC result imply that

$$\int_0^1 (\bar{d}(x) - \bar{u}(x)) dx = 0.148 \pm 0.039 \quad (2)$$

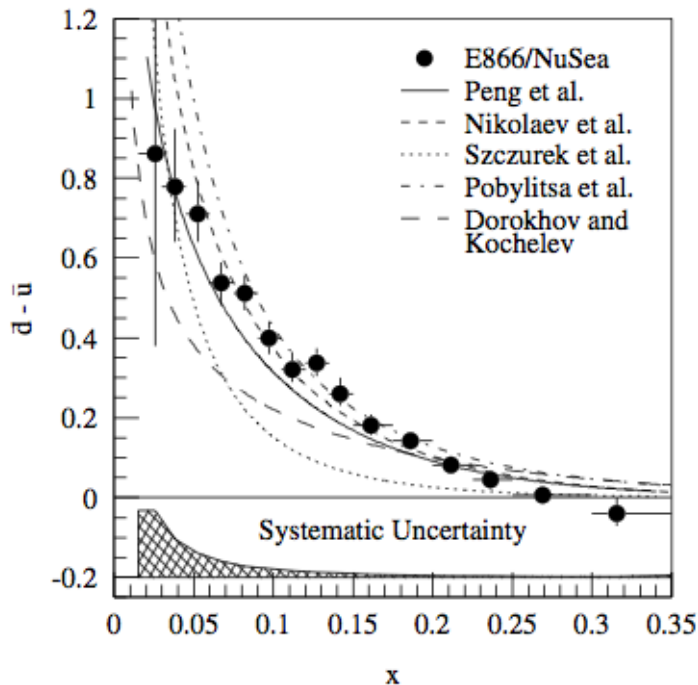


Figure 2: Comparison of the E866  $\bar{d}\bar{u}$  data with various model calculations [13]

136 Independent confirmation of the  $\bar{d}/\bar{u}$  flavor asymmetry was later provided by Drell-Yan  
 137 experiments [10, 11, 12, 13] and the semi-inclusive DIS experiment [14]. Figure 2 shows

138 the E866 result on  $\bar{d}(x) - \bar{u}(x)$  at  $Q^2 = 54 \text{ GeV}^2/c^2$ . The surprisingly large asymmetry  
 139 between  $\bar{d}$  and  $\bar{u}$  is observed over a broad range of  $x$ . The E866 data provide a direct  
 140 evaluation of the  $d - u$  integral, namely,  $\int_0^1 (\bar{d}(x) - \bar{u}(x)) dx = 0.118 \pm 0.012$ , which is in good  
 141 agreement with the NMC result shown in Eq. 2. The observation of  $\bar{u}$ ,  $\bar{d}$  flavor asymmetry  
 142 has inspired many theoretical works regarding the origin of this asymmetry. Perturbative  
 143 QCD, in which the  $q\bar{q}$  sea is generated from the  $g \rightarrow q\bar{q}$  splitting, has difficulties explaining  
 144 such an asymmetry. The small  $d, u$  mass difference (actually,  $m_d > m_u$ ) of 2 to 4 MeV  
 145 compared to the nucleon confinement scale of 200 MeV does not permit any appreciable  
 146 difference in their relative production by gluons.

147 Regardless, one observes a surplus of  $\bar{d}$  which is the heavier of the two species. Field  
 148 and Feynman long time ago speculated that the  $g \rightarrow u\bar{u}$  process would be suppressed  
 149 relative to  $g \rightarrow d\bar{d}$  due to a Pauli-blocking effect arising from the presence of two  $u$ -  
 150 quarks as compared to a single  $d$ -quark in proton. The consequences of Pauli-blocking  
 151 have, however, been shown to be small [15]. Thus, another, presumably non-perturbative,  
 152 mechanism must account for the large measured  $\bar{d}$ ,  $\bar{u}$  asymmetry. Many of the non-  
 153 perturbative approaches to explain the  $\bar{d}$ ,  $\bar{u}$  asymmetry involve the use of isovector mesons  
 154 (particularly the pion). Recent reviews [16, 17, 18] have extensive discussions on various  
 155 theoretical models. In the meson-cloud model, the virtual pion is emitted by the proton  
 156 and the intermediate state is pion + baryon. More specifically, the proton is taken to be a  
 157 linear combination of a “bare” proton plus pion-nucleon and pion-delta states, as below,

$$\begin{aligned}
 |p\rangle \rightarrow & \sqrt{1-a-b}|p_0\rangle + \sqrt{a}\left(-\sqrt{\frac{1}{3}}|p_0\pi^0\rangle + \sqrt{\frac{2}{3}}|n_0\pi^+\rangle\right) \\
 & + \sqrt{b}\left(\sqrt{\frac{1}{2}}|\Delta_0^+\pi^-\rangle - \sqrt{\frac{1}{3}}|\Delta_0^+\pi^0\rangle + \sqrt{\frac{1}{6}}|\Delta_0^0\pi^+\rangle\right)
 \end{aligned} \tag{3}$$

158 The subscript zeros on the virtual baryon states indicate that they are assumed to have  
 159 symmetric seas, so the asymmetry in the antiquarks must be largely generated from the  
 160 pion valence distribution. The coefficients  $a$  and  $b$  are the fractions of the  $\pi N$  and  $\pi\Delta$   
 161 configurations, respectively, in the proton. These fractions can be calculated using the  
 162  $\pi NN$  and  $\pi N\Delta$  couplings, and form factors may be obtained from experiment. The  
 163 asymmetry in the proton sea then arises because of the dominance of  $\pi^+$  among the  
 164 virtual configurations. Figure 2 shows that the pion-cloud model can reproduce the  $x$ -  
 165 dependence of the  $\bar{d}\bar{u}$  distribution very well. The success of the meson-cloud model in  
 166 explaining the  $\bar{d}$ ,  $\bar{u}$  asymmetry suggests that a direct measurement of the meson cloud  
 167 in DIS, such as that proposed here, is feasible. The idea is that the meson cloud in the  
 168 nucleon could be considered *as a virtual target* to be probed by various hard processes,  
 169 including DIS.

170 We here propose to measure the semi-inclusive reactions  $H(e, e'p)X$  and  $D(e, e'pp)X$   
 171 in the deep inelastic regime of  $8 < W^2 < 18 \text{ GeV}^2$ ,  $1 < Q^2 < 3 \text{ GeV}^2$ , and  $0.05 < x < 0.2$ ,  
 172 for very low proton momenta in the range 60 MeV/c up to 400 MeV/c. The key to  
 173 this experimental technique is to measure the low-energy outgoing “recoil” proton in  
 174 coincidence with a deeply inelastically scattered electron from the hydrogen target. In the  
 175 deuterium case, an *additional* low energy spectator proton will be identified at backward  
 176 angle to identify the neutron target. The inclusive electron kinematics determine that

177 a DIS event has occurred, i.e. that the reconstructed  $Q^2$  and missing mass,  $W^2$ , of the  
 178 recoiling hadronic system are sufficiently large. However, unlike the standard inclusive  
 179 case, the low momentum protons  $N'$  measured in time and vertex coincidence with the  
 180 DIS event ensure that the deep inelastic scattering occurred from partons within the  
 181 meson cloud (here identified as a pion) surrounding the nucleon. This can be achieved  
 182 by employing the Super Bigbite Spectrometer to detect the scattered electrons in time  
 183 and vertex coincidence with low momentum proton(s) measured in a low mass radial time  
 184 projection chamber (RTPC, a BONUS experiment type detector).

185 The idea of considering the meson cloud as a virtual pion target was used at the HERA  
 186  $e-p$  collider to measure the pion structure functions at low- $x$  in a hard diffractive process,  
 187 where forward-going neutrons or protons were tagged in coincidence with the DIS events,  
 188 as shown in Fig. 1. While the HERA experiments have provided very interesting first data  
 189 on the extraction of pion structure functions using the Sullivan process, there are many  
 190 reasons for extending such measurements to JLab energies. The pion, being the lightest  
 191 and simplest hadron, has a central role in our current description of nucleon and nuclear  
 192 structure. The pion has been used to explain the long-range nucleon-nucleon interaction,  
 193 making it a fundamental component of the Standard Model of Nuclear Physics [19, 20, 21].  
 194 The pion is also used to explain the flavor asymmetry of the quark sea in the nucleon.  
 195 Moreover, the masses of light mesons such as the pion are believed to arise from dynamical  
 196 chiral symmetry breaking [22], and thus models of the pion must account for both its role  
 197 as the Goldstone boson of quantum chromodynamics (QCD) and as a quark-antiquark  
 198 system.

199 Experimental knowledge of the partonic structure of the pion is very limited due to the  
 200 lack of a stable pion target. Most of the current knowledge of the pion structure function  
 201 in the valence region is obtained primarily from pionic Drell-Yan scattering [23]-[25], and  
 202 in the pion sea region at low Bjorken- $x$ , from hard diffractive processes measured on  $e-p$   
 203 collisions at HERA [27]. The existing data on the pion structure function from Drell-Yan  
 204 scattering is shown in Fig 3. Also shown, in Fig. 4, is the pion structure function data at  
 205 low  $x$  from HERA, where forward-going neutrons or protons were tagged in coincidence  
 206 with the DIS events. These results seem to indicate that the pion sea has approximately  
 207 one-third of the magnitude of the proton sea, while from the parton model one expects  
 208 the pion sea to be two-thirds of the proton sea.

209 There are several theoretical calculations of the pion structure in the valence region,  
 210 however they tend to disagree with each other. The parton model [28], perturbative QCD  
 211 based models [29, 30] and some non-perturbative models such as those based on the Dyson-  
 212 Schwinger Equation [26]-[33] predict a  $(1-x)^a$  dependence with  $a \geq 2$ . On the other hand  
 213 relativistic constituent quark models [34, 35], Nambu-Jona-Lasinio models [36]-[39], the  
 214 Drell-Yan-West relation [40, 41] and even arguments based on quark-hadron duality [42]  
 215 favor a linear  $(1-x)$  dependence of the pion structure function at high- $x$ . Calculations  
 216 of the pion structure function in the pion sea region, such as those of the chiral quark  
 217 model [43], also disagree with the extraction from the HERA data, in fact these models  
 218 predict that the momentum fraction of pion sea is larger than the proton sea. These  
 219 discrepancies tell us that it is essential to measure the pion structure function over a wide  
 220 range of  $x$  using new techniques.

221 The HERA kinematics are limited to the very low  $x$  region, where no independent

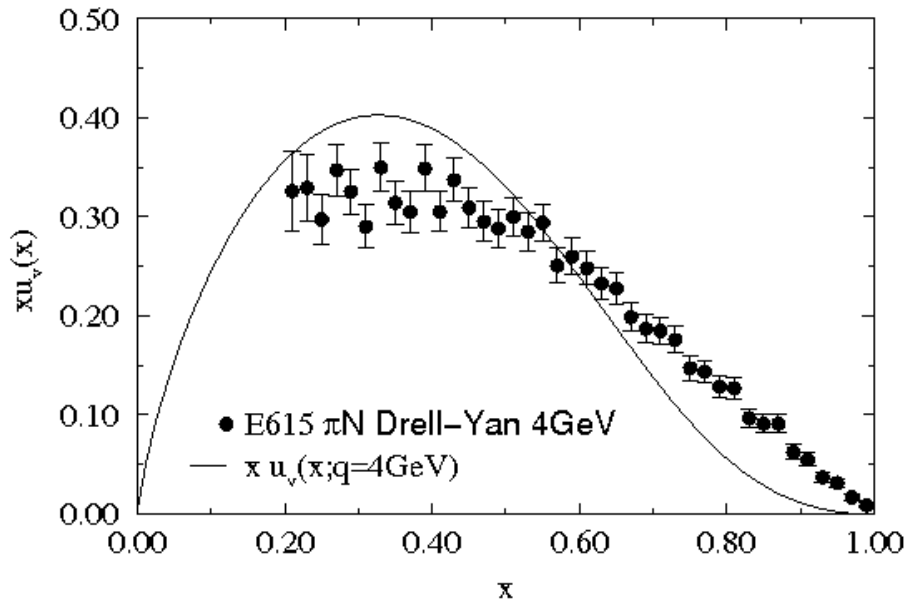


Figure 3: Existing data for the pion structure function from Drell-Yan Experiment E615 [23]. The solid curve is the calculation from Ref. [26].

222 measurement of pion structure functions exists. This makes it difficult to check the  
 223 validity of the interpretation of the HERA data in terms of the meson-cloud model. The  
 224 12 GeV upgrade of JLab will allow access kinematics of  $|t| < 0.2 \text{ GeV}^2$ ,  $Q^2 > 1 \text{ GeV}^2$   
 225 and  $M_x > 1.0 \text{ GeV}/c^2$ , which will enable us to probe the high and intermediate  $x$  region  
 226 of the pion, where some data on the structure functions already exist from the pion-  
 227 induced Drell-Yan experiments. A comparison of the  $x$ -dependence of the pion structure  
 228 function deduced from the Sullivan process and the Drell-Yan process would provide a  
 229 very stringent test of the pion-cloud model.

230 Other advantages of this measurement as here proposed for Jefferson Lab are: (1)  
 231 The large angular and kinematic coverage for the recoiling proton (or recoil and spectator  
 232 proton pair) detected using the proposed GEM-based detector, in coincidence with the  
 233 scattered electron, will facilitate a detailed study of the Sullivan process as a function  
 234 of several variables including the proton momenta and angles. (2) It is important to  
 235 determine in one experiment the magnitude of the Sullivan process by detecting *both* the  
 236  $p(e, e'p)X$  and  $d(e, e'pp)X$ , i.e. the  $n(e, e'p)X$ , reactions. The charged pion exchange  
 237 process has the advantage of less background from Pomeron and Reggeon process [44]  
 238 and the charged pion cloud is, moreover, double the neutral pion cloud in the proton.  
 239 The measurements of the pion parton distribution in the Drell-Yan (Fermilab E615 and  
 240 possibly at COMPASS in the future) is limited to charged pions. The proposed experiment  
 241 will measure both the charged and neutral pion. This will facilitate a check of the validity  
 242 of isospin symmetry and any other dynamical effects. Generally, the complementarity of  
 243 the  $p \rightarrow p$  and  $n \rightarrow p$  reactions will assist in the identification of pion exchange and other  
 244 contributions. Lastly, (3) The HERA measurements were obtained at small  $x$  and rather  
 245 large  $Q^2$ . The Jefferson Lab kinematics, at larger  $x$  and smaller  $Q^2$ , will help study the

$$F_2^{LN(3)}(x_L = 0.73)/\Gamma_\pi, \Gamma_\pi = 0.13$$

H1

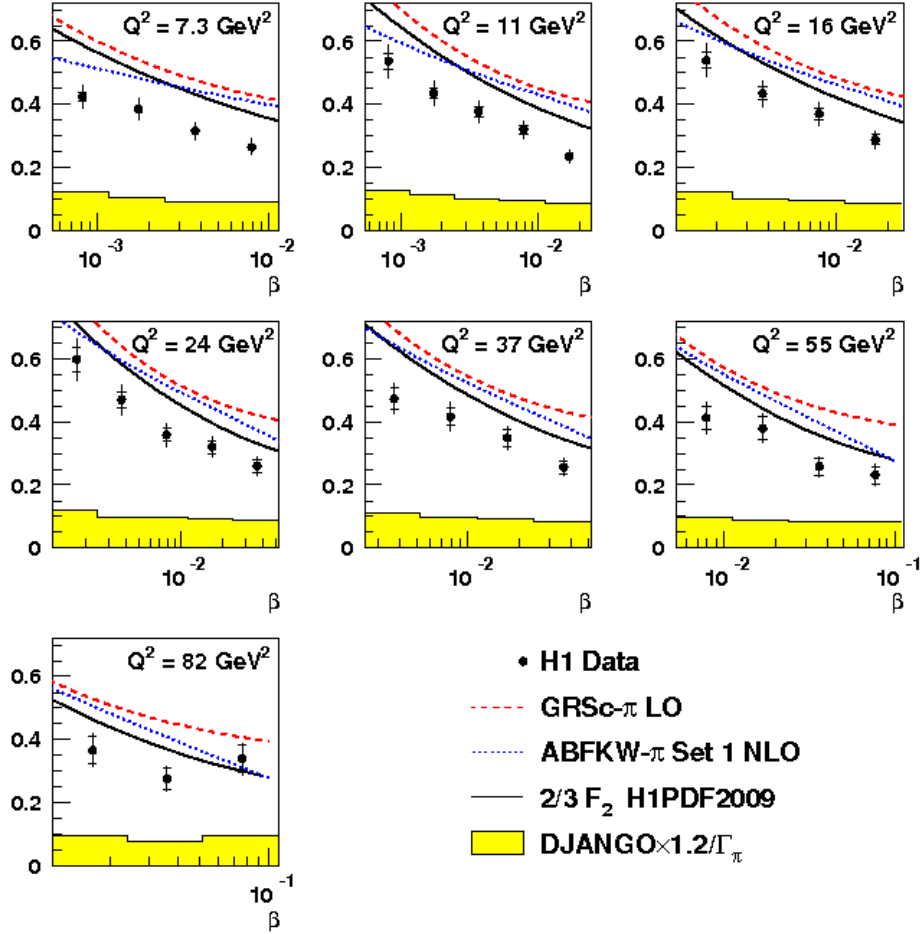


Figure 4: Pion structure functions measured by H1 [27] in comparison with parameterizations of various pion parton distribution functions. The Bjorken- $x$  of the pion is denoted as  $\beta$ .

246 evolution of these effects between the two experiments.

247 The physics motivation for this experiment is, in summary, this: to pioneer a measure-  
 248 ment of the Deep Inelastic Scattering (DIS) cross section, while tagging low-momentum  
 249 recoil and spectator protons for the purpose of probing the elusive mesonic content of the  
 250 nucleon structure function. The extraction of the mesonic structure of the nucleon from  
 251 the tagged DIS cross section is inherently model dependent, and hence we will endeavor  
 252 to examine all reasonable models that are currently available (such as Regge models of  
 253 baryon production and Dyson-Schwinger equation (DSE) inspired models) or that may  
 254 be available in the future. There is vibrant interest in this physics, as evidenced by recent  
 255 workshops on the topic, for instance "Flavor Structure of the Nucleon Sea", held in July

256 2013 in Trento, Italy, "Exploring Hadron Structure with Tagged Structure Functions",  
257 held in January 2014 at Jefferson Lab, and "The Structure of the Pion", an invited session  
258 at the APS April Meeting held in 2015 in Baltimore, MD. Previous proposals to access this  
259 physics have been hindered largely by lack of low momentum reach, large backgrounds, or  
260 both [45]. It should be stressed that the measurement of the tagged DIS cross section is  
261 a worthy goal on its own right as there is scant existing data, particularly in the valance  
262 quark region, but the ultimate goal of the experiment is to extract information on the  
263 specific mesonic content of the nucleon from these tagged DIS cross sections.

264 To describe and further motivate the proposed measurement, we begin below with a  
265 description of tagged DIS kinematics and predictions from a phenomenological model for  
266 the mesonic component of the nucleon structure function (1.1). We then move on to a  
267 discussion of possible avenues for extraction of the pion structure function via the Sullivan  
268 process (1.2). Lastly, we discuss the broader impact of the experiment (1.3), and finally  
269 summarize the motivations in (1.4).

## 1.1 Tagged Deep Inelastic Scattering (TDIS)

In specific regions of kinematics, the observation of low-momentum recoil protons in the semi-inclusive reaction  $eN \rightarrow eNX$  can reveal features associated with correlated  $q\bar{q}$  pairs in the nucleon, sometimes referred to as the nucleon’s “pion cloud”, or more generally, the five-quark component of the nucleon wave function. In particular, at low values of the four-momentum transfer squared  $t \equiv k^2 = (p - p')^2$ , where  $p$  and  $p'$  are the initial and final nucleon four-momenta, the cross section displays, according to current models, behavior characteristic of pion pole dominance. Here, contributions from the exchange of non-pseudoscalar quantum numbers ( $J^P = 0^-$ ), such as the vector  $\rho$  and  $\omega$  mesons, are suppressed, and the pole-effect of these heavier mesons is less pronounced in our kinematic reach, leading to a qualitatively different  $t$  dependence than that arising from the pion pole. Furthermore, the contribution from the three-quark component of the wave function is highly suppressed because the momentum of the recoiling nucleon peaks at  $\sim 1$  GeV/c.

### 1.1.1 Predictions of a Pion Cloud Model

Phenomenological models of the meson cloud [46, 47, 48] have been developed to study the contributions of the meson cloud to the structure function of the nucleon. The model [46] used in this proposal is described in some detail in Appendix A. Here we present the pion structure function and the tagged semi-inclusive structure function calculated using this model. The structure functions were studied as a function several kinematic variables, such as recoil proton momentum,  $t$  and  $x$  [46, 47, 48]. These studies form the basis for the projected experimental results, rates, and beam time request in this proposal.

According to the pion cloud model [3], the contribution to the inclusive  $F_2$  structure function of the nucleon from scattering off a virtual pion emitted from the nucleon can be written as

$$F_2^{(\pi N)}(x) = \int_x^1 dz f_{\pi N}(z) F_{2\pi}\left(\frac{x}{z}\right), \quad (4)$$

where  $z = k^+/p^+$  is the light-cone momentum fraction of the initial nucleon carried by the interacting pion. In the infinite momentum frame this coincides with the longitudinal momentum fraction.

While inclusive reactions require integration of the pion momentum over all possible values, detecting the recoil proton in the final state allows one to dissect the internal structure with significantly more detail and increase the sensitivity to the dynamics of the meson exchange reaction. The semi-inclusive structure function will be given by the unintegrated product

$$F_2^{(\pi N)}(x, z, k_\perp) = f_{\pi N}(z, k_\perp) F_{2\pi}\left(\frac{x}{z}\right), \quad (5)$$

where  $k_\perp$  is the transverse momentum of the pion, and the unintegrated distribution function  $f_{\pi N}(z, k_\perp)$  is defined by

$$f_{\pi N}(z) = \frac{1}{M^2} \int_0^\infty dk_\perp^2 f_{\pi N}(z, k_\perp^2). \quad (6)$$

The dependence of the tagged structure functions on the kinematical variables that are measured experimentally can be studied by relating the magnitude of the 3-momentum

306  $\mathbf{k}$  of the exchanged pion in the target rest frame to the pion's transverse momentum  $k_{\perp}$   
 307 and light-cone fraction  $z$ ,

$$\mathbf{k}^2 = k_{\perp}^2 + \frac{[k_{\perp}^2 + (1 - [1 - z]^2)M^2]^2}{4M^2(1 - z)^2}. \quad (7)$$

308 Experimentally, the quantities most readily measured are the momentum of the produced  
 309 proton,  $\mathbf{p}'$ , which in the rest frame is  $\mathbf{p}' = -\mathbf{k}$ , and the scattering angle  $\theta_{p'} = \theta$  of the  
 310 proton with respect to the virtual photon direction. In the limit  $k_{\perp}^2 = 0$ , the magnitude  
 311 of  $\mathbf{k}$  becomes

$$|\mathbf{k}|_{k_{\perp}^2=0} = \frac{zM}{2} \left( \frac{2 - z}{1 - z} \right), \quad (8)$$

312 which imposes the restriction  $z \lesssim |\mathbf{k}|/M$ . This relation is illustrated in Fig. 43 for values  
 313 of  $z$  up to 0.2.

314 This is a critical guiding parameter for the proposed experiment. Since we seek to mea-  
 315 sure the low momentum region where pseudo scalar production dominates, the region of  
 316 interest becomes  $z \lesssim 0.2$ . This corresponds to the measurable proton range,  $60 \lesssim \mathbf{k} \lesssim 400$   
 317 MeV/c, of the radial time projection chamber discussed in detail below. It is important  
 318 to note that, since  $x < z$ , this also determines both the  $x$  and  $Q^2$  (given the maximum  
 319 beam energy) of the experiment.

320 The predictions from the detailed study of the kinematic dependence of the pionic  
 321 contribution to inclusive and semi-inclusive structure functions (described in Appendix A)  
 322 are shown in Figs. 5 and 6. In Fig. 5 the  $x$  dependence of the inclusive structure function  
 323  $F_{2p}(x)$  for the proton is compared to both the structure function for the full pionic content  
 324 of the proton  $F_2^{\pi p}(x)$  and the tagged, semi-inclusive structure function  $F_2^{(\pi p)}(x, \Delta|\mathbf{k}|, \Delta\theta_{p'})$ ,  
 325 for the indicated ranges in tagged, recoil proton momentum. The lowest momentum  
 326 protons will be measured within the spectrometer acceptance, but clearly with lower  
 327 statistics. Each momentum range corresponds by definition to a range in  $t$ , causing these  
 328 low momentum protons to be of particular interest for extrapolation very close to the  
 329 pion pole. It is planned that a range of  $t$  (proton momentum) points will be obtained  
 330 at multiple values of  $x$  to map out this dependence. The full range of expected data are  
 331 shown in a similar plot, along with an example of  $t$  extrapolation, in section 3 of this  
 332 proposal.

333 Fig. 6 shows the equivalent neutron structure functions, but here compared to the  
 334 strength of other physics channels: the tagged structure functions for  $(\pi^- p)$ ,  $(\rho^- p)$ , and  
 335  $(\pi^0 \Delta^0 + \pi^- \Delta^+)$ . The neutron target is planned to be tagged by two protons in coincidence  
 336 with the scattered electron, one as was utilized successfully at backward angles in BONUS  
 337 to identify the nearly free neutron in deuterium, and the other the recoil, tagged, semi-  
 338 inclusive proton at more forward angles as discussed previously. The  $\rho$  component of this  
 339 process is nearly negligible in comparison to the  $\pi$ , and the already small intermediate  $\Delta$   
 340 resonance component to the process may be further reduced by a kinematic cut discussed  
 341 in Appendix A, leveraging the differences in  $t_{min}$  as in Fig. 44. The momentum ranges as  
 342 in Fig. 5 would appear nearly the same here for the neutron as they do for the proton and,  
 343 conversely the other channels depicted here for the neutron would appear quite similarly  
 344 for the proton. As with the proton, the full range of expected data are shown on a a  
 345 similar plot in section 3 of this proposal.

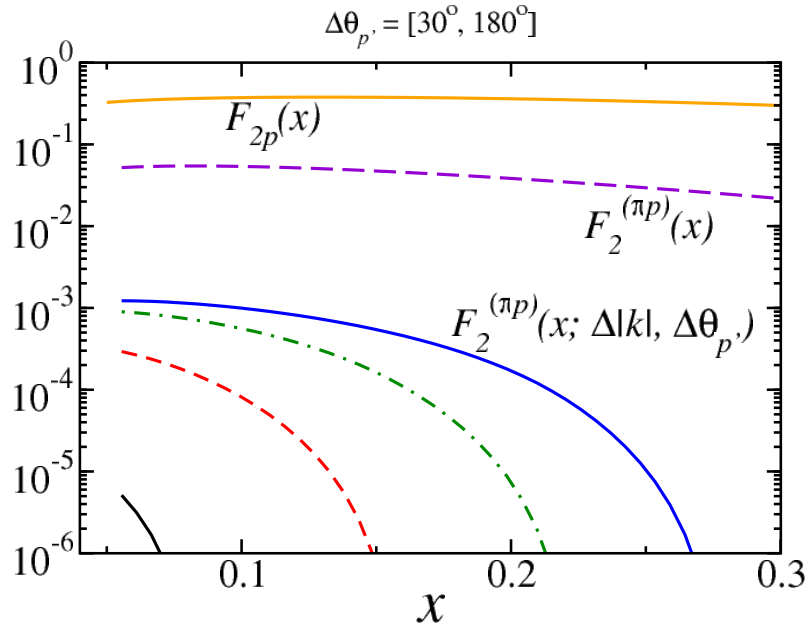


Figure 5:  $x$  dependence of the semi-inclusive structure function  $F_2^{(\pi p)}(x, \Delta|\mathbf{k}|, \Delta\theta_{p'})$  (blue curve). For comparison, the total integrated  $\pi p$  contribution  $F_2^{(\pi p)}$  to the inclusive proton structure function is shown (violet dashed), as is the total inclusive  $F_{2p}$  structure function (orange solid). The lower bands follow from varying the integration range  $\Delta|\mathbf{k}|$ ; they correspond to  $\Delta|\mathbf{k}| = [60, 100]$  MeV (black, solid),  $\Delta|\mathbf{k}| = [100, 200]$  MeV (red, dashed),  $\Delta|\mathbf{k}| = [200, 300]$  MeV (green, dot-dashed), and  $\Delta|\mathbf{k}| = [300, 400]$  MeV (blue, solid).

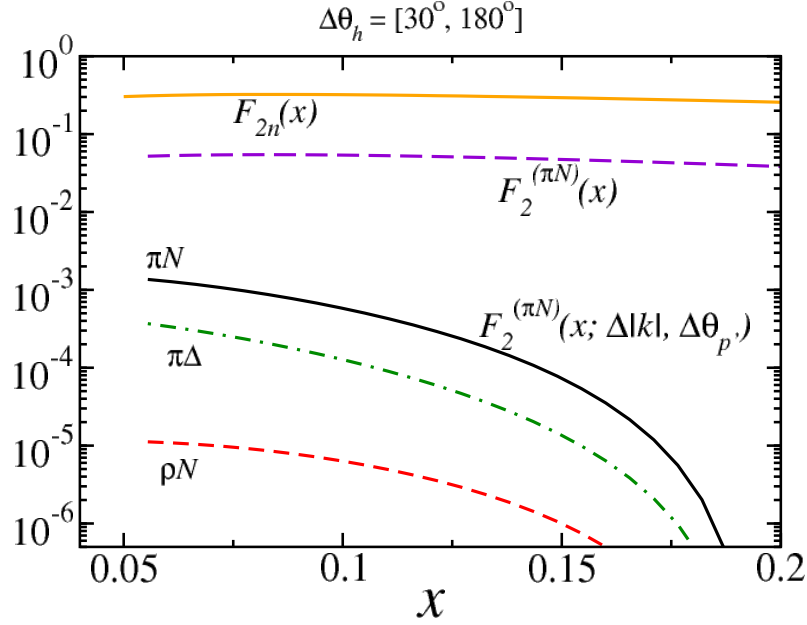


Figure 6: Structure functions as in Fig. 5, but now for the  $x$  dependence of  $F_2^{(\pi p)}(x, \Delta|\mathbf{k}|, \Delta\theta_{p'})$  for charge-exchange in, e.g., the  $n \rightarrow \pi^- p$  process. The tagged semi-inclusive structure function for  $(\pi^- p)$  (black, solid),  $(\rho^- p)$  (red, dashed), and  $(\pi^0 \Delta^0 + \pi^- \Delta^+)$  (green, dot-dashed) are compared with the inclusive structure function of the neutron  $F_{2n}(x)$  (orange), and the fully-integrated  $(\pi^- p)$  contribution  $F_2^{\pi N}(x)$  (violet, dashed).

## 1.2 Extraction of the Pion Structure Function

In this experiment we will measure the semi-inclusive structure function of the recoil proton (neutron), denoted as the tagged structure function,  $F_2^T$ . The expected kinematic coverage in  $z$  and  $x$  is shown in Figs. 33 and 34, along with the yield for 10 days of beam for the measurement of the TDIS cross section. We will form the ratio  $R^T$  of the tagged (coincidence) to the DIS (singles) cross sections to measure the tagged structure function  $F_2^T(x, Q^2, z, t)$ . The measured ratio of cross sections may be written as:

$$R^T = \frac{d^4\sigma(ep \rightarrow e' X p')}{dx dQ^2 dz dt} / \frac{d^2\sigma(ep \rightarrow e' X)}{dx dQ^2} \Delta z \Delta t \sim \frac{F_2^T(x, Q^2, z, t)}{F_2^p(x, Q^2)} \Delta z \Delta t. \quad (9)$$

Since the proton structure function  $F_2^p(x, Q^2)$  is known extremely well over a wide range of  $x$  and  $Q^2$ , we can extract the tagged structure function  $F_2^T(x, Q^2, z, t)$  as:

$$F_2^T(x, Q^2, z, t) = \frac{R^T}{\Delta z \Delta t} F_2^p(x, Q^2). \quad (10)$$

This ratio method reduces systematic uncertainties due to luminosity, electron trigger efficiency, and radiative corrections. We can, moreover, check many uncertainties by also measuring the cross section obtained from the DIS singles and comparing to the global  $F_2^p(x, Q^2)$  inclusive data set. The pion structure function  $F_2^\pi$  can then be determined from the measured tagged structure function  $F_2^T$  as in Equations (5) and (6) in Section 1.1.

The pion flux  $f_\pi(z, t)$  will be calculated using models of the mesonic content of the nucleon. All existing models will be examined for this purpose with the final choice determined by the model that best describe the data, with the ensuing model dependence addressed. Some of the current models that are available are:

- i. The phenomenological model described in Sec. 1.1 and Appendix A.
- ii. DSE inspired models. These have recently provided a prescription for a unified description of the pion's valence-quark distribution, its distribution amplitude, electromagnetic form factor and Generalized Parton Distribution function (GPD). This approach notably produces model independent quark distribution functions that are nearly independent of pion virtuality.
- iii. Regge models of baryon and meson production.

## 1.3 Dyson-Schwinger Equation Inspired Models

In the modern language of QCD, the pion is simultaneously described as a bound state in quantum field theory and a Goldstone boson associated with dynamical chiral symmetry breaking (DCSB) [22]. This implies that an accurate description of the partonic content of the pion is essential for a clear understanding of QCD. The Dyson-Schwinger equations (DSEs) provide a non-perturbative approach to QCD by describing the pattern of chiral symmetry breaking and connecting them to experimental observables. One of the early predictions of QCD was that the large  $x$  pion valence-quark distribution should be given by  $q^\pi(x) = (1-x)^2$  [49, 28]. However, leading order analysis of pion Drell-Yan data seemed to suggest a  $q^\pi(x) = (1-x)$  [23] dependence. Recently, it has been shown that

382 the impulse-approximation expression for the pion's dressed quark distributions that were  
 383 used in these analyses ignore the contributions from the gluons which bind the quarks.  
 384 When these gluonic contributions are accounted for in the framework of the Rainbow  
 385 Ladder (RL) truncation of the Dyson-Schwinger Equation, the corrected valance-quark  
 386 distributions are model independent and have well defined uncertainty [50]. The reanalysis  
 387 of the Drell-Yan data using the new corrected expression for the dressed-quark distribution  
 agrees well with the QCD prediction, as shown in Fig. 7. Using this RL truncation

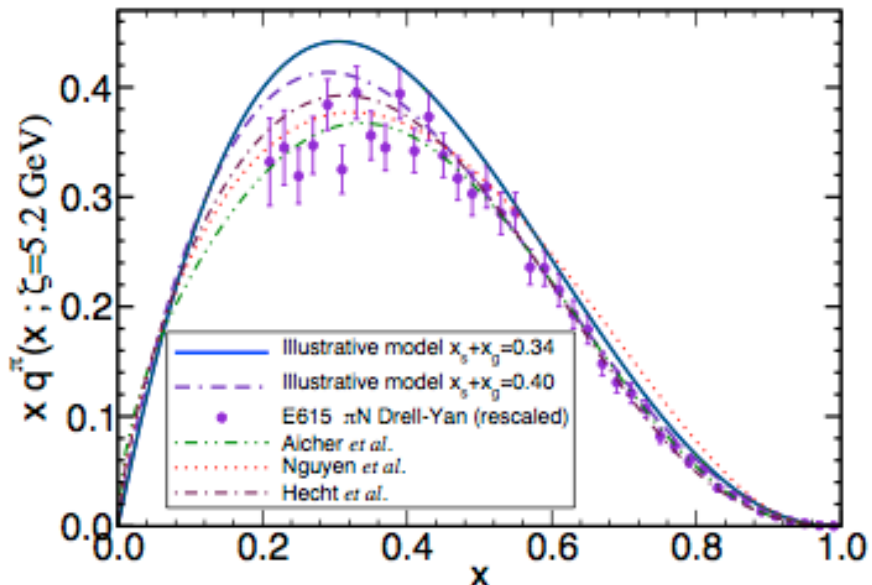


Figure 7: Several pion dressed-quark distributing functions and two illustrative models compared to the reanalyzed Drell-Yan data [50]

388  
 389 framework the authors have also outlined a procedure for the unification of the pion  
 390 valance-quark distribution, its distribution amplitude and its elastic electromagnetic form  
 391 factor. Recently, a procedure to obtain the pion's valance-quark GPD within the same  
 392 framework has also been described [51]. In this new framework it has been shown that  
 393 the form factor of a pion is essentially independent of its virtuality over a large range  
 394 of pion virtualities (  $0 - 7 m_\pi^2$  ), as shown in Figs. 8 and 9. Pion virtuality is defined  
 395 as,  $t_\pi = (P - P')$  where  $P(P')$  are the initial(final) nucleon 4 vectors following a pion  
 396 exchange.

397 It follows from this unified picture of the pion's valance-quark distribution that a  
 398 virtuality-independent result for the pion form factor entails a virtuality-independent pion  
 399 parton distribution function (PDF), based on Eqs. (5) & (6) in [51]. This is a powerful  
 400 indication that it should be feasible to extract the pion structure function from the tagged  
 401 DIS cross section measured at high pion virtualities, even substantially further from the  
 402 pole than is here proposed.

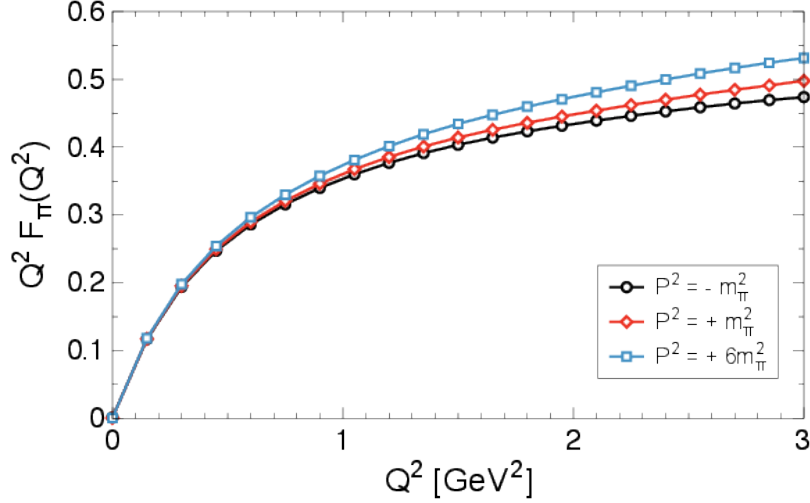


Figure 8: The pion electromagnetic form factor for pion virtuality ranging from 0 -  $7m_\pi^2$  [52].

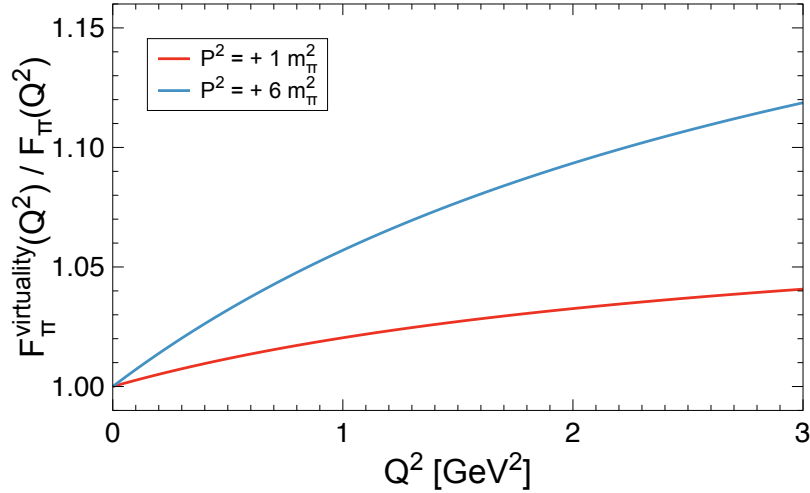


Figure 9: The ratio of off-shell to on-shell pion electromagnetic form factor for pion virtualities as indicated [52].

### 403 1.3.1 Corrections to the Extraction of Pion Structure Function

404 The extraction of the pion structure function will have to be corrected for a number of  
 405 complications, such as non-pion pole contributions,  $\Delta$  and other  $N^*$  resonances, absorp-  
 406 tive effects, and the uncertainties of the pion flux. These corrections are minimized by  
 407 measuring at the lowest recoil proton momenta possible. The low recoil proton momentum  
 408 minimizes the absorptive correction since at lower momenta the pion cloud is further from  
 409 the bare nucleon. The absorptive corrections are twice as large for the  $n \rightarrow p$  reaction

410 compared to the  $p \rightarrow n$ , but they are well known and have been recently calculated [53].  
 411 In addition, the low proton momentum ensures that the higher meson mass exchanges  
 412 are suppressed by the energy denominator. The ratio of the pion contribution to sum of  
 413 all exchange contributions for the phenomenological model (Sec. 1.1) is shown in Fig. 10,  
 414 for both neutral and charged pions and for 3 different choices of the form factors used  
 415 to suppress the wave function which controls the irregular behavior at large momenta  
 416 (exponential, dipole and covariant dipole form factors). Here, the total includes  $\rho$  meson  
 and Delta resonance contributions.

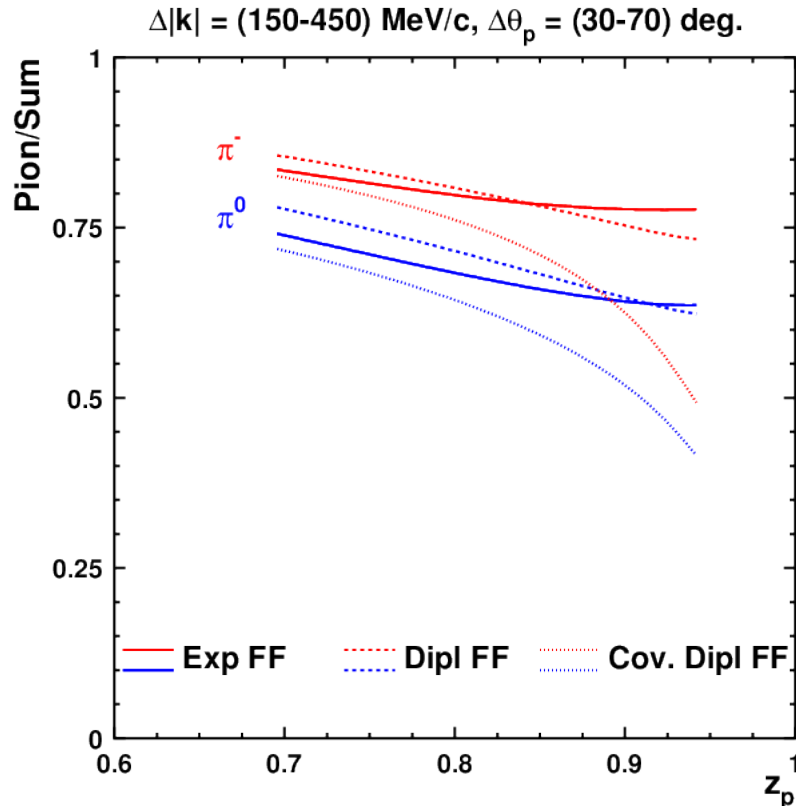


Figure 10: Ratio of pion to all contributions in the model of Ref. [46], for charged and neutral pions, shown for three different form factors used to control the irregular behavior at large momenta.

417

418 A somewhat analogous ratio plot is also shown in Fig. 11(left panel) for the charged  
 419 pion case from Regge model work described in [54]. In this case, the sum total in the  
 420 ratio denominator includes  $\rho$  meson and  $a$  Reggeon contributions, as are also shown  
 421 in Fig. 11 (right panel). This approach has provided a good description of ZEUS and  
 422 H1 data for leading neutron production in DIS [53], and has been calculated here by  
 423 the authors for the kinematics of this proposed Jefferson Lab experiment. In Fig. 10  
 424 and 11, the definition of  $z_p$  corresponds to  $1 - z$  used elsewhere in this proposal and  
 425 so the measurements will be performed at the plotted range  $z_p > 0.7$ . The solid purple  
 426 curve shows the pion fraction in the cross section. To get some feeling for the theoretical  
 427 uncertainty, a maximal uncertainty assumption that the  $a_1$  term was grossly overestimated

428 was employed. Assuming that it is much smaller, the dashed-blue curve was obtained. The  
 429 biggest uncertainty is here expected to be the  $a_1$  term because: (1) It relies on diffractive  
 430  $\pi + p \rightarrow p\rho + p$  data, which are available only at high energies; and (2) The  $a_1 - N$   
 431 coupling was calculated purely theoretically, employing PCAC and the 2d Weinberg sum  
 432 rule. The magnitude of this coupling has never been tested on data.

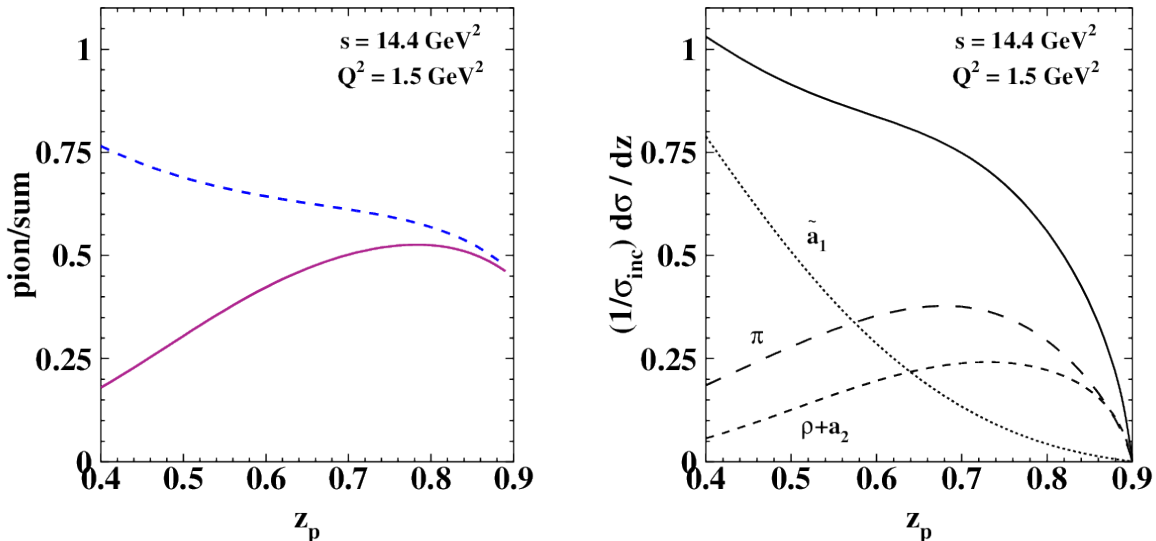


Figure 11: (left) Ratio of pion to all contributions in the Regge model of Ref. [53], for charged pions. The curves representing the range of theoretical uncertainty as described in the text. (right) Mesonic contributions to the nucleon in the Regge model of Ref. [53], for charged pions. Here and in the Figure above the  $z_p$  indicated is  $1 - z$  used elsewhere in this proposal. The proposed measurements will be performed at the (here) plotted  $z_p > 0.7$ .

433 While the models agree that the pion is the dominant contribution to the meson cloud  
 434 of the nucleon, the largest uncertainty in extracting the pion structure function arises  
 435 from lack of knowledge of the exact pion flux in the pion cloud. This can be stated,  
 436 alternatively, as the percentage of the measured structure function attributable to the  
 437 pion. One of the main issues is whether to use the  $\pi NN$  form factor or a Reggeized form  
 438 factor. The difference between these two methods can be as much as 20% [55]. From  
 439 the N-N data the  $\pi NN$  coupling constant is known to 5% [56]. If we assume that all  
 440 corrections can be performed with a 50% uncertainty and we assume a 20% uncertainty  
 441 in the pion flux factor, the overall systematic uncertainty on our proposed measurement  
 442 will be 24%.

443 However, by comparing to pionic Drell-Yan data at moderate  $x$  (where it is most

444 reliable), we can have a measurement of the pion flux factor and its dependence on  $z$  and  
 445  $t$ . For example the pion structure function at  $x = 0.5$  has been measured from the pionic  
 446 Drell-Yan data to an accuracy of 5% [23]-[25]. The proposed data will have significant  
 447 overlap with the Drell-Yan data, allowing us to leverage this precision and likely reduce  
 448 our projected uncertainty. Moreover, we can normalize to this data at  $x = 0.5$  to precisely  
 449 study the critical question of the shape of the structure function at the higher  $x$  values.

### 450 1.3.2 Comparison of Neutron and Proton Data

451 This experiment will allow us to compare the tagged semi-inclusive cross-section and  
 452 tagged structure functions of the proton and the neutron, for the first time in the valence  
 453 regime. Moreover, all previous measurements of the pion structure function have been  
 454 restricted to charged pions. This experiment will therefore be the first extraction of  
 455 the structure function of the neutral pion. Beyond the basic isospin factor of 2, these  
 456 measurements will provide kinematic reach to shed light on any dynamical effects that  
 457 may exist. For example, comparison of the measurements by the H1 [27] and ZEUS  
 458 collaborations by tagging forward-going neutrons or protons proved to be very informative.  
 459 While neutron data proved to be dominated by  $\pi^+$  exchange and could be used to extract  
 460 the pion structure function at low  $x$ , the proton data had large contributions from the  $f_2$   
 461 exchange in addition to  $\pi^0$  exchange and was unusable for extraction of the pion structure  
 462 function.

463 The measured cross sections from the proton and neutron in this experiment will be  
 464 compared to a Regge model. In the Regge model, the contribution of a specific exchange  
 465  $i$  (pion, Pomeron,  $\rho$ ,  $\omega$ ,  $a_2$ ,  $f_2$ ) is determined by the product of its flux  $f_i(z, t)$  and its  
 466 structure function  $F_2^i$  evaluated at  $(x_i, Q^2)$ . Thus, for recoil (tagged) nucleon production  
 467 at low  $p_T$ , we have;

$$F_2^T(x, Q^2, z) = \sum_i \left( \int_{t_0}^{t_{min}} f_i(z, t) dt \right) \cdot F_2^i(x_i, Q^2) \quad (11)$$

468 In the Regge model it is assumed that the neutral pion, the Pomeron and the  $f_2$  will be  
 469 the leading contributions to the cross section from a proton while the charged pion,  $\rho$   
 470 and  $a_2$  are the leading contributions for the neutron [57, 54]. But, Regge phenomenology  
 471 also predicts that the flux of Reggeons with isospin one ( $\rho$  and  $a_2$ ) is only  $\approx 3\%$  of  
 472 the flux of Reggeons with isospin equal to zero ( $\omega$  and  $f_2$ ) [57]. It also predicts for the  
 473 neutron that the contributions from charged pion exchange are an order of magnitude  
 474 larger than the contributions from  $\rho$  and  $a_2$  [58]. Pomeron exchange also does not give a  
 475 significant contribution since diffractive dissociation is believed to be here only  $\approx 6\%$  of  
 476 the pion exchange contribution [58]. Moreover, the pion absorption corrections are twice  
 477 as large for the neutron compared to the proton, but they are well known and have been  
 478 calculated [53].

479 The measured tagged cross section and extracted tagged structure function will be  
 480 compared to a Regge model where, assuming the dominance of a single Regge exchange,  
 481 the differential cross section for recoil baryon production as a function of  $z$  at fixed  $t$  should  
 482 be proportional to  $z^{-n}$ , where  $n = 2\alpha(t) - 1$ , and  $\alpha(t)$  specifies the Regge trajectory of  
 483 the dominant exchange. For pion exchange,  $n$  averaged over the  $t$  dependence is expected

484 to be  $n \approx -1$  while other Reggeons are expected to have  $n > -1$ . Thus, by comparing  
485 the  $z$  dependence of the cross-section from a proton and a neutron, we will be able to  
486 determine the dominant exchange mechanism. If the predictions for pion exchange are  
487 found to describe the data, the pion flux from the Regge model fits to hadron-hadron  
488 data will be used to extract the pion structure function. The comparison of data from  
489 hydrogen and deuteron (neutron) targets will serve as essential cross checks for the models  
490 used in the extraction of the pion structure function.

## 491 **1.4 Impact for the Jefferson Lab 12 GeV Program and Beyond**

492 The remarkably successful application of the quark-parton model in the description of  
493 deep-inelastic scattering (DIS) data over a very large kinematic domain has propelled  
494 this simple picture of the nucleon at high energies into becoming part of the common  
495 language employed by medium and high energy physicists. Massive and numerous global  
496 fitting efforts utilize perturbative QCD to extract the universal parton distribution func-  
497 tions from a host of high energy data including from decades of precision DIS experiments.  
498 Nevertheless, the QCD-improved parton model cannot, by itself, give a complete descrip-  
499 tion of the structure of the nucleon at high energies. It is unable to (nor was it intended  
500 to) explain the spectrum of the nucleon's non-perturbative features. Here, effective de-  
501 grees of freedom, for example in the form of a mesonic cloud of the nucleon, have been  
502 evoked to describe the long range structure of the nucleon. This has proved a reasonable  
503 approach in explaining for instance the deviation from the QCD-parton model predic-  
504 tion for the Gottfried sum rule and the flavor asymmetry in the sea quark distributions  
505 observed in Drell-Yan experiments. However, despite the various phenomenological suc-  
506 cesses of nucleon models which incorporate mesonic degrees of freedom, as yet there is  
507 scant experimental evidence unambiguously pointing to the existence of a mesonic cloud  
508 in high energy reactions. This experiment is designed to provide a clear signal of the  
509 presence of mesonic degrees of freedom in nucleon DIS, measuring where the pion con-  
510 tribution to the nucleon structure function should appear (i.e at relatively small Bjorken  
511  $x \sim 0.1$ ), while simultaneously measuring the well know DIS cross sections. Data from  
512 this experiment will, therefore, provide valuable input into high energy phenomenology  
513 and global fitting efforts for parton distribution functions by providing the size of the  
514 non-perturbative structure that needs to be addressed.

515 It is important to note also that this experiment may prove beneficial to a wide swath  
516 of the already-approved Jefferson Lab science program. There are multiple experiments  
517 planning to reach the factorization regime in semi-inclusive processes to access for instance  
518 transverse momentum dependent parton distribution functions as well as other semi-  
519 inclusive deep inelastic scattering physics such as flavor decomposition of the nucleon  
520 and single spin asymmetries. These experiments seek to measure at kinematics where the  
521 current fragmentation region may be cleanly separated from a target regime described as a  
522 nucleon via the well-known parton distribution functions. This latter aspect is not a valid  
523 approach if target fragmentation, is not also considered as a production mechanism that  
524 will impact the yield of measurable hadrons. Here, the mesonic component of the nucleon  
525 is likely for example to play an important role in final state interactions. Therefore, the  
526 proposed measurement may provide information valuable to precise interpretation of the

527 underlying phenomena involved in a host of semi-inclusive scattering experiments in the  
528 Jefferson Lab 12 GeV era.

529 Moving into the future, the tagging approach pioneered here may pave the way for  
530 programs to map out the non-perturbative, mesonic, component of the nucleon both at  
531 Jefferson Lab in the 12 GeV era and at the proposed EIC, mEIC, and LHeC colliders. In  
532 the near term, this experimental approach could be leveraged further to tag semi-inclusive  
533 scattering such as  $ep \rightarrow ep\pi X$ , or to probe the strange quark content via  $ep \rightarrow e\Lambda X$ . At  
534 higher energies, the hard diffractive scattering measurements at HERA demonstrate the  
535 wealth of interesting physics specifically in the regime of these proposed new colliders.  
536 Because of the typically small cross sections, high luminosity as well as dedicated tagging  
537 detectors will be required; these are currently being included into electron-ion collider  
538 planning. Such measurements will also complement the new Drell-Yan data that will  
539 become available from experiments at COMPASS and Fermilab, and also possibly at the  
540 J-PARC facility. In all, this proposed Jefferson Lab experiment will provide a permanent,  
541 lower energy anchor for a wealth of future experiments.

## 542 1.5 Physics Motivation Summary

- 543 • This experiment will provide a first measurement of the tagged structure functions  
544 of the proton and the neutron in the valence regime.
- 545 • There is a great need for an experimental technique to probe the mesonic content  
546 of the nucleon. Few experiments have been able to directly probe the partonic  
547 components of the meson cloud of the nucleon, basically only scant data from hard  
548 diffractive processes at HERA and Drell-Yan to date. A range of models and the-  
549 oretical work that predict the size and components of this cloud are available, but  
550 little data exists to constrain them.
- 551 • The well established quark flavor asymmetry in the nucleon sea can be explained in  
552 terms of the meson cloud model. The Sullivan process allows access to the meson  
553 cloud of the nucleon, and this direct measurement of this component will facilitate  
554 checks on the validity of this interpretation.
- 555 • Measuring the "recoil" proton at low momentum will facilitate reasonable extrapola-  
556 tion to the pion pole term, thereby facilitating a measurement of the pion structure  
557 function via the Sullivan process. The partonic structure of the pion, the lightest  
558 and simplest hadron, is not well measured over the entire Bjorken- $x$  range and the  
559 predictions of models describing pion structure differ significantly.
- 560 • Measurements of the pion parton distribution in the Drell-Yan (Fermilab E615 and  
561 possibly at COMPASS in the future) are limited to charged pions. The proposed  
562 experiment will measure both the charged and neutral mesonic component. This  
563 will facilitate a check of the validity of isospin symmetry and any other dynamical  
564 effects. Generally, the complementarity of the  $p \rightarrow p$  and  $n \rightarrow p$  reactions will assist  
565 in the identification of pion exchange and other contributions.

- 566 • The nucleon structure function has been measured to multiple orders of magnitude  
567 precisely in  $x$  and  $Q^2$ . The standard description is given by valence quarks which  
568 radiate gluons, thereby generating sea quarks - all well described by DGLAP evolu-  
569 tion. However, some part of the measured structure function data ( $\approx 20\%$  in total)  
570 comes from scattering from non-perturbative, bound mesonic or meson-like objects  
571 in the nucleon. This experiment will provide a direct measure of a part of this effect,  
572 tagging the latter while simultaneously measuring the former.
  
- 573 • The measurement of tagged DIS at HERA explored diffractive scattering and ex-  
574 tracted the pion parton distribution at small  $x$  and rather large  $Q^2$ . At JLab, one  
575 can measure this at larger  $x$  and smaller  $Q^2$  – advantageous kinematics for evolution  
576 between the two experiments.
  
- 577 • This is a potential gateway experiment to a broad program, in the near term at  
578 Jefferson Lab and in the far term at an electron-ion collider, to map out the non-  
579 perturbative, mesonic content of the nucleon.

## 2 Experiment

### 2.1 Overview

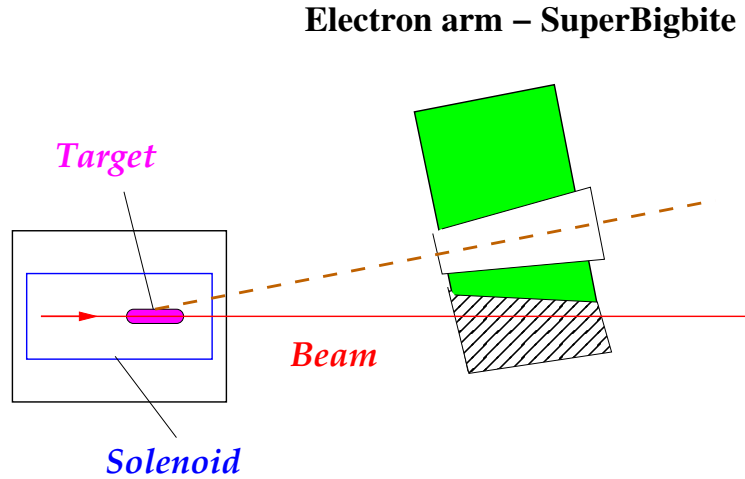


Figure 12: Schematic layout of the proposed experiment.

### 2.2 Experiment Luminosity

The subject of the proposed experiment is an essential feature of the nucleon internal structure, specifically, a quark-antiquark correlation related to the meson cloud associated with a (fluctuating/recoiling) nucleon. In spite of enormous developments in the field of nucleon structure over the last 65 plus years since the original Fermi and Marshall 20% number for the pion-nucleon component of the nucleon wave function, this estimate endures without significant change. However, the experimental signature of the pion in the nucleon remains under debate.

A fixed-target experiment at kinematics with modest momentum transfers and higher  $x$  will compliment the existing HERA measurements which investigated diffractive DIS in a collider regime with an 800 GeV proton beam on a 30 GeV positron beam. The proposed study of TDIS through detection of a very low energy proton "tag" in coincidence with a scattered electron DIS event will measure a very different part of the reaction space, one that may be rigorously evolved to the HERA kinematics, as well as related to the long-searched-for Sullivan process for accessing the pion structure function.

In this section we present a set of considerations concerning the Figure-of-Merit (FOM) for this experiment, a product of electron-nucleon luminosity ( $\mathcal{L}$ ), electron detector acceptance ( $\Omega_e$ ), and recoil proton detection efficiency ( $\eta_p$ ), required for TDIS investigation. The level of luminosity which may be used in the proposed experimental setup is constrained by the signal size and, critically, the experimental background rates.

The cross section of the inclusive DIS process for an 11 GeV electron beam scattered from a proton target is very well known, see e.g. the PDG report [59]. A traditional measurement of the DIS cross section with 1% precision and minimal DIS requirements

605 on  $Q^2$  and  $W^2$  does not require much time with any electron spectrometer at Jefferson  
 606 Lab, and experiments have been approved that will extend the existing body of such data  
 607 in this kinematic regime from SLAC and other laboratories. The (unmeasured) percentage  
 608 of such events coming from the meson cloud of the proton target should be approximately  
 609 20%. However, the fraction of DIS events in coincidence with a **low energy** proton is  
 610 much smaller than the total meson-nucleon part of the wave function. According to recent  
 611 calculations, described above, the fraction of DIS events with proton momenta below 400  
 612 MeV/c and at an angle within the detector acceptance ( $30 - 70^\circ$ ),  $F_{\pi p}(x_{Bj}, \Delta k, \Delta\theta)$ , is  
 613 about 1% [60] (see Fig. 13).

614 Such a small fraction leads to a low rate of true coincidence events between the DIS-  
 615 scattered electron and the recoiling, target proton. Therefore, the proposed experiment  
 616 requires a large FOM and good control of accidental coincidences. The high rate of  
 617 accidental coincidence events is the main problem for measurement of the TDIS cross  
 618 section. These events are mainly due to a large rate of low energy protons produced  
 619 in low momentum transfer reactions, such as small angle electron elastic scattering and  
 620 meson photoproduction. In the deuterium target, one needs to also consider deuteron  
 621 photodisintegration into low momentum proton-neutron pairs and the wider angular  
 622 distribution of the protons involved in quasi-elastic electron scattering. There are four  
 623 parameters which allow rejection of the accidental protons:

- 624 • The polar angle between the proton track and the beam direction.
- 625 • The correlation in time between an electron hit in the SBS and a proton hit in the  
626 RTPC.
- 627 • The correlation between the vertices of the electron and proton tracks.
- 628 • The correlation between the vertex of the spectator proton (tagging the neutron as  
629 a target, as in BONUS) and the recoil proton for the deuterium target.

### 630 2.2.1 Accidental Rates

631 **Hydrogen Case** There is a very high total rate of low momentum protons from low  
 632 momentum transfer elastic electron-proton scattering. In the momentum range  $k > 70$   
 633 MeV/c and luminosity  $2.9 \times 10^{36}$  cm<sup>-2</sup>/s, the rate is about  $\sim 170$  MHz. However, these  
 634 protons scatter predominantly in the angular range  $78 - 88^\circ$  (see Fig. 27 left panel). In  
 635 comparison, the proton data of interest will be in a range only up to  $65^\circ$  maximum. The  
 636 projected polar angle resolution of the RTPC of  $1^\circ$  will allow rejection of the range of  
 637 angles where most of the elastically scattered protons are located. The background rate  
 638 in the angular range to be used in the experiment,  $30 < \theta_p < 70^\circ$ , is relatively small  
 639 (0.2 MHz) as can be seen from Fig. 28.

640 The photoproduction mechanism leads to a higher rate in the angular range of interest,  
 641 which was found to be  $\sim 10$  MHz from the hydrogen target at the proposed luminosity  
 642 of  $2.9 \times 10^{36}$  cm<sup>-2</sup>/s in the momentum and angular range of interest. For additional infor-  
 643 mation about this background, see the discussion of background simulations in Sec. 2.5,  
 644 of this proposal.

645 The projected time resolution of the RTPC of 10 ns allows for a narrow 20 ns timing  
 646 cut in offline data analysis. The length of the RTPC target cell (40 cm), combined with  
 647 the good vertex resolution of the SBS spectrometer, will provide additional suppression  
 648 of accidental events by a factor of 10.

649 The probability of protons to be accidentally detected in coincidence with the DIS  
 650 electrons can be calculated as  $P_{acc} = f_{prot} \times \tau \times (2.5\sigma_z/L)$ , where  $f_{prot}$  is the singles proton  
 651 rate ( $\sim 10$  MHz),  $\tau$  is the timing cut/window (20 ns),  $\sigma_z$  is the vertex resolution (0.8  
 652 cm) and  $L$  is the length of the target (40 cm). The resulting total accidental probability  
 653 is expected, then, to be **0.01** per electron. As shown in Fig. 13, the fraction of DIS  
 654 events with protons within the detector acceptance with momentum  $< 400$  MeV/c is  
 655  $\sim 1\%$ , this implies a signal to accidental ratio of  $\sim 1$ . However, we want to detect the  
 656 lowest momentum protons that can be reasonably separated from the background. It is  
 657 expected that we can extract the signal from the background for signal to accidental ratio  
 658 of **1/10**, this implies that we can then measure proton rates as low as 0.1% of the DIS rate  
 659 (shown by the magenta line in Fig. 13). This corresponds to protons with momentum as  
 660 low as  $\sim 200$  MeV/c as can be seen from Fig. 13. The feasibility of extracting the signal  
 661 from the background for signal to accidental ratio of 1/10 is discussed below and shown  
 662 in Fig. 14.

663 **Deuterium Case** For the deuterium target at the same electron-nucleon luminosity  
 664 of  $2.9 \times 10^{36}$  cm<sup>-2</sup>/s, there will be a large additional background rate coming from photo-  
 665 disintegration protons. The estimated rate based on the photon flux is  $\sim 90$  MHz in the  
 666 momentum range below 250 MeV/c. Moreover, there will be an even larger rate of the  
 667 quasi-elastically produced protons, estimated to be  $\sim 250$  MHz. For detailed estimates  
 668 see the discussion of background simulations in Sec. 2.5, of this proposal. This combined  
 669 estimated rate of 340 MHz complicates investigation of TDIS from the neutron at low  
 670 proton momenta. However, in the proton momentum range above 200 MeV/c the rate of  
 671 protons drops dramatically. Therefore we calculate the accidental probability for several  
 672 different bins of the forward ( $30 < \theta_p < 70$ ) proton momentum. Moreover, the vertex  
 673 resolution when detecting backward protons is about a factor of 2 better ( $\sigma_{z2} \sim 0.4$  cm).  
 674 The rate for backward protons ( $100 < \theta_p < 140^\circ$ ) in the  $p_p = 70 - 200$  MeV/c range is  $\sim$   
 675 200 MHz, which leads to a probability for accidental coincidence of **0.1** per electron.

676 For the triple coincidence between the electrons, forward protons and backward pro-  
 677 tons, the probability of the protons to be accidentally detected in coincidence with the  
 678 DIS electrons can be calculated as  $P_{acc}^{(2)} = f_{prot1} \times \tau_1 \times f_{prot2} \times \tau_2 \times (2.5\sigma_{z1}/L) \times (2.5\sigma_{z2}/L)$ ,  
 679 where  $f_{prot1}, f_{prot2}$  are the singles proton rate for the forward and backward going protons,  
 680  $\tau_1, \tau_2$  are the timing cut/window (20 ns),  $\sigma_{z1}$  and  $\sigma_{z2}$  are the forward and vertex proton  
 681 vertex resolution (0.8 and 0.4 cm respectively) and  $L$  is the length of the target (40 cm).  
 682 The resulting total accidental probability for different bins of the forward proton momen-  
 683 tum is shown in Table. 1. These probabilities are in all ranges better than those for the  
 684 Hydrogen target.

685 The projected level of the signal to accidental rate is illustrated in Fig. 14. The event  
 686 distribution over  $dz = z_p - z_e$  after other cuts are applied for a level of signal to background  
 687 ratio of 1/10. The  $\delta z$  range represents the 40 cm target length, and it is important to  
 688 note that the background events will be produced evenly along the target. In contrast,  
 689 the data will be produced at a single vertex that we propose to measure with an accuracy

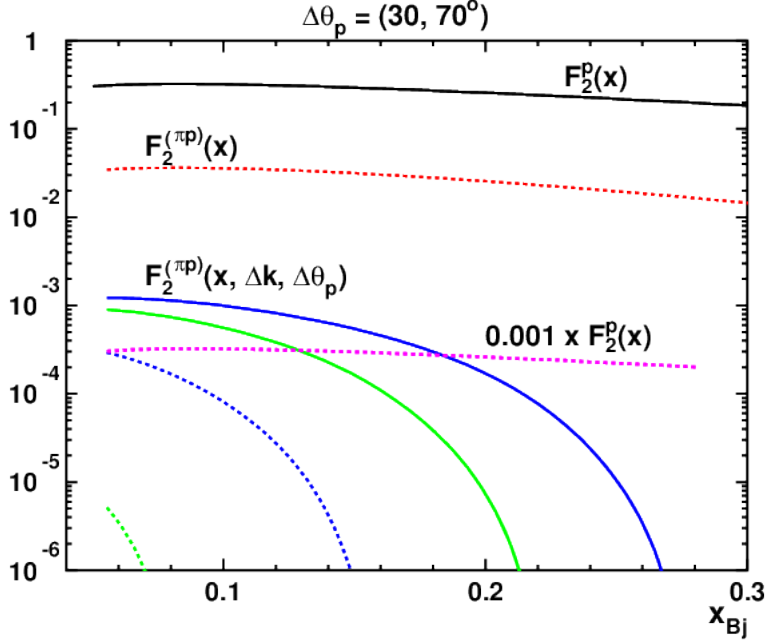


Figure 13: The proton SF  $F_2^p$  (black), the pion related part  $F_2^{(\pi p)}$  (red dashed), and the fraction  $F_2^{(\pi p)}(\Delta k, \Delta \Theta_h)$  vs  $x$  for the proton momentum intervals,  $\Delta k$ : in MeV/c - green dashed (60-100), blue dashed (100-200), green (200-300), blue (300-400) and the cut on the angle between the proton and the virtual photon momentum directions,  $\Theta_p$ , between  $30^\circ$  and  $70^\circ$ . The dashed magenta line shows the level of signal for which signal to accidental ratio is 1/10, demonstrating the range of proton momentum that can be reasonably separated from the backgrounds. It also shows the  $x$  range over which the mesonic contribution to DIS could be measured.

Forward proton momentum (MeV/c)	forward proton rate (MHz)	accidental coincidence probability
200-250	14	0.0015
250-300	7	0.008
300-350	4	0.0005
350-400	3	0.0003

Table 1: The total accidental probability for triple coincidence for backward ( $100 < \theta_p < 140^\circ$ ) proton rate, in the  $p_p = 70 - 200$  MeV/c range, of 200 MHz.

690 of 8 mm.

691 For verification of the analysis procedure and measurement at higher  $x$  up to 0.16 where  
692 the expected rate of e-p events is smaller (see Fig. 5), we plan to reduce the luminosity  
693 to  $\lesssim 1 \times 10^{36}$  cm<sup>-2</sup>/s and collect data for an additional period of 5 days. It is at these  
694 kinematics that the projected drop in the meson cloud distribution, and consequently in  
695 the fracture function, should be most apparent.

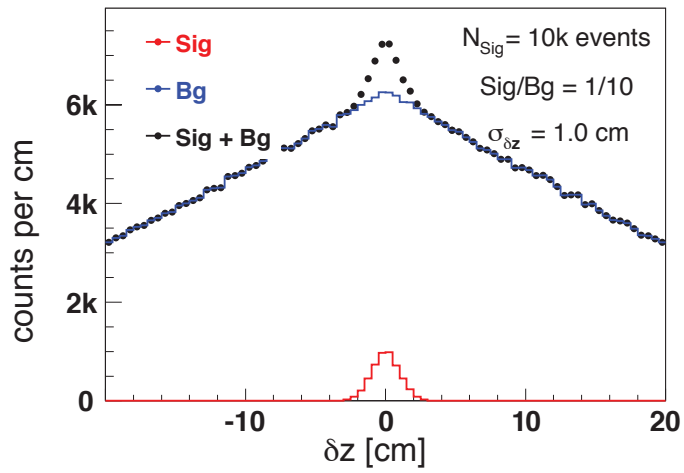


Figure 14: The projected event distribution over  $\delta z = z_p - z_e$  for a ratio of signal to background of 1/10 (in the "2- $\sigma$ " area).

## 2.3 Recoil Detector

Detection of a soft nucleon is complicated by a large intensity of the secondary electrons, photons, and soft nucleons produced in the interaction of the high energy electron beam with the target. A proton detection option as employed by the BONUS and CLAS eg6 experiments has several essential advantages over neutron detection:

- The ionization density in the soft proton track for the momentum range 60-400 MeV/c is very high, which allows effective suppression of the secondary electron and soft photon induced signals.
- The protons of interest (2.0 - over 30 MeV kinetic energy) have a momentum component perpendicular to the beam direction much larger than the typical perpendicular momentum of the secondary electrons, which allows use of magnetic separation of the proton and electron background using a solenoidal magnet.
- The proton track allows for reconstruction of the event vertex and direction, which are powerful means for rejection of accidental events.
- The proton detector readout segmentation could be on the level of  $10^5$  or above, which is at least a factor of 100 times higher than practical for a neutron detector.

The recoil detector will be fundamentally the same as the cylindrical RTPC being developed for the experiment to measure the structure function of the free neutron (E12-06-103, or BONUS-12), the latter being based on the very successful cylindrical RTPCs that were employed for the BONUS and CLAS eg6 experiments as pictured in Fig. 15. The proposed RTPC will, however, utilize a different solenoid. This is an existing solenoid, shown in Fig. 16, with a 400-mm warm bore, a total length of 152.7 cm, and a superconducting coil that operates with a 47 kG magnetic field in the center of the magnet. This solenoid belongs to the UVa collaborators on this proposal, and is currently being used for tests of LHC detector electronics. Any stray field of the solenoid on the asymmetric iron of the SBS, could be symmetrically balanced with an iron yoke. While this approach certainly needs a full analysis for exact design, we note that this is reasonably standard, and that a solenoidal field surrounded by an iron yoke is typical for collider geometry. The heating of the superconducting coil is not expected to be an issue for this proposal because of the relatively small luminosity and the coil being immersed in liquid He.

Simulation studies have shown that increasing the radial drift region by a factor of 2 compared to the BONUS and eg6 RTPC detectors can provide at least a 50% relative improvement in the momentum resolution, as well as extending the momentum range of the detector. The larger bore of this magnet will facilitate the RTPC having a larger radial drift distance than that proposed for BONUS-12. The enhanced drift region will facilitate measurements of proton momenta up to 400 MeV/c with a resolution of 3%. The length of this magnet is also a help, allowing us to use a longer (40 cm) target for improved background rejection and luminosity.

The proposed TDIS RTPC will be 40 cm long and consist of an annulus with inner radius of 5 cm and an outer radius of 15 cm. The amplification of the drifting electrons will be achieved by three layers of cylindrical Gas Electron Multiplier (GEM, see Ref. [61])

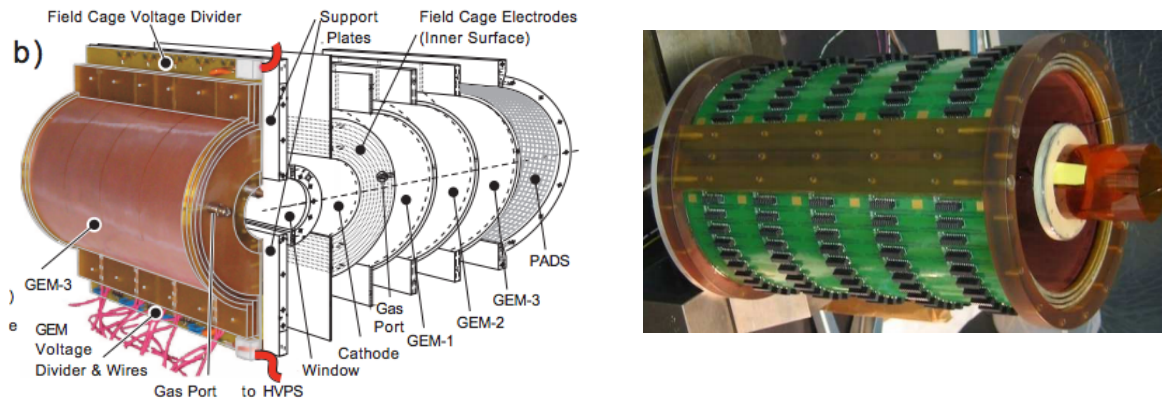


Figure 15: (left) Photograph of the BoNuS RTPC, showing the left module with the readout padboard removed and a complementary exploded view exposing the components of the right module. (right) Photograph of the eg6 RTPC during assembly.

737 foils at radii of 15 cm. This will be surrounded by a cylindrical readout surface featuring  
 738 elongated pads. GEMs are  $50\ \mu\text{m}$  thick polyamide foils coated on both sides with a  $5\ \mu\text{m}$   
 739 copper layer and punctured with  $70\ \mu\text{m}$  holes. The distance between these holes is about  
 740  $140\ \mu\text{m}$ . By applying a voltage in the range of 200 V to 300 V across the two copper layers  
 741 a very high electric yield is formed inside the holes. Ionized electrons from the maximally  
 742 ionizing low momentum protons drifting towards the GEM foil produce an avalanche of  
 743 secondary electrons when captured and accelerated through the holes. The total gain in  
 744 GEM will be of the order of  $10^3$ , which is far below the limit of gain achievable with GEM-  
 745 based detectors. The electrons are transferred to the next GEM foil and, after passing  
 746 three GEM foils, the resulting electron pulse will be detected on the readout plane. The  
 747 full length of the RTPC could be closer to 60 cm to accommodate protons emitted at  
 748 angle as small as  $30^\circ$  relative to the beam direction.

749 As with BONUS and CLAS eg6, materials between the target and the sensitive detec-  
 750 tor volume have to be minimized to prevent energy loss of the protons and to minimize  
 751 the interaction of background particles which reduce efficiency of magnetic confinement  
 752 of the low energy background. The tracking region will be formed by a set of light weight  
 753 straws, a set of wires, and the GEM. The straws will hold a  $2\ \mu\text{m}$  gold plated kapton  
 754 film cylinder. The wires will be used to increase the electrical field at a larger radius. To  
 755 further minimize background events, a thin wall Be tube will be used for the first 50 cm  
 756 of the beam line downstream from the target. After that a larger, standard Al pipe will  
 757 provide connection to the exit beam line through the SBS magnet to the beam dump.  
 758 The window between the low pressure, cold RTPC and atmosphere will be made from a  
 759 pre-deformed 0.5 mm aluminum plate with a supporting grid of steel bars. The recent  
 760 design of a cylindrical GEM chamber at INFN Frascati for the KLOE experiment [62]  
 761 will be explored for potential improvements.

762 The RTPC will be filled with a He based mixture which allows reduction of the sec-  
 763 ondary background in the chamber due to low energy photon induced signals. A study  
 764 of GEM operation with low pressure He-based mixtures has been demonstrated in the  
 765 reference [63]. For this proposal we assumes an average electric field of  $E = 500\ \text{V/cm}$ ,



Figure 16: Photograph of the available 5T solenoid.

766 an average magnetic field of  $B = 4.7$  T, and a temperature of  $T = 77$  K. The operating  
 767 pressure for the RTPC would be approximately  $p = 0.2$  atm. Since the drift gas properties  
 768 go as  $E/p$ , this situation is equivalent to the case of 2500 V/cm at 1 atm. The drift gas  
 769 assumed here is 90% He and 10% CH<sub>4</sub> as the quencher. The vapor pressure of CH<sub>4</sub> at  
 770 77 K is sufficient to get this concentration in the mixture. The information given here  
 771 is based on the extensive simulations done and data compiled by Sauli and Sharma and  
 772 by Sharma and Assran [64]. The mixture could also be further optimized as needed. If  
 773 it turns out that more stability is needed, it could be achieved by increasing the amount  
 774 of CH<sub>4</sub> in the gas mixture, for example, by increasing the operating temperature of the  
 775 RTPC. Increased temperature increases the vapor pressure of CH<sub>4</sub>, resulting in a higher  
 776 amount of CH<sub>4</sub> in the mixture.

777 The drift velocity for above operating conditions is approximately 2 cm/s. At the 500  
 778 V/cm electric field, the drift velocity is at a relative plateau region, where it changes by  
 779 only about 10% for a 25% change in either the electric field or the pressure. Given the  
 780 drift distance of 10 cm in the RTPC, the drift time range would be approximately  $5\mu s$ .  
 781 The Lorentz angles for He based gas mixtures is about a factor of 3 smaller than the  
 782 corresponding Lorentz angles for Ar based mixtures. For the proposed E and B fields,  
 783 the Lorentz angle would be around 35-degrees for the proposed gas mixture.

784 The longitudinal diffusion is approximately  $350 \mu m/cm^2$ . For the  $\sim 10$  cm drift from  
 785 the furthest cluster the maximum longitudinal diffusion is expected to be  $\sim 1mm$  (with  
 786 a time spread of 50 ns); however, the relevant quantity for background suppression is the  
 787 signal time with respect to the trigger, which is determined by the cluster closest to the  
 788 readout, with a drift distance of about 1 cm. For these cluster the dispersion would be  
 789 approximately  $350 \mu m$ , with a time spread of approximately 15 ns. This is sufficient to  
 790 achieve the desired 10 ns time resolution. The transverse diffusion is approximately  $225$   
 791  $\mu m/cm^2$ . For the 10 cm drift from the furthest cluster, the maximum transverse diffusion

792 would be approximately  $750\ \mu\text{m}$ ; which is less than the readout pitch of 1 mm and has  
793 no significant effect on the position resolution.

794 The readout will be in a pad configuration with each pad having dimensions of 1 mm  
795 (azimuthal) x 21.25 mm (z). The readout is a 2D u-v strip readout with a strip pitch of  
796 1 mm in either direction. With this strip pitch we assume a  $300\ \mu\text{m}$  position resolution  
797 from the RTPC. Given this high resolution from the RTPC, the limiting factor for the  
798 vertex reconstruction is the electron vertex from the SBS. The overall vertex resolution  
799 is assumed to be 8 mm. In order to reduce the per channel occupancy, each strip in  
800 both u and v layers is separated into 21 mm segments. Each strip segment is individually  
801 bridged by a via to a  $50\ \mu\text{m}$  wide connection strip on the back of the readout plane. This  
802 connection strip connects the strip segment to its own readout channel. The connection  
803 strips for u strips and for v strips will be on two different layers insulated from each other  
804 on the back of the readout plane. The outermost cylindrical layer of the detector will be  
805 the readout board made out of a flexible circuit board, with traces that will connect to  
806 front end electronic cards located at the end(s) of the cylindrical detector. Improvements  
807 in GEM electronics over the last few years will allow for the readout cards to be placed  
808 at the end(s) of the RTPC cylinder. This will allow some further increase in the drift  
809 region as compared to the BONUS and eg6 experiments by removing the need for radial  
810 on-board amplification.

811 To read out signals from the detector, we will use the APV25 chip based Scalable  
812 Readout System (SRS) developed at CERN by the RD51 collaboration. The APV25 chip  
813 is an analog chip developed by the Imperial College London for the CMS experiment  
814 silicon trackers. It has been subsequently adopted by several experiments, such as the  
815 COMPASS trackers at CERN, STAR FGT at BNL and others. It is also planned for the  
816 tracking detectors in the SBS project. The APV25 chip samples 128 channels in parallel  
817 at 20 MHz or 40 MHz and stores 192 analog samples, each covering 50 ns or 25 ns, per  
818 channel. Following a trigger, up to 30 consecutive samples from the buffer are read-out  
819 and transmitted to an ADC unit that de-multiplexes the data from the 128 channels and  
820 digitizes the analog information. Operating in the 20 MHz mode with the 30 sample  
821 readout will give a dynamic time range of  $1.5\ \mu\text{s}$  for the APV readout. This is sufficient  
822 to cover the drift time range of the TPC, which is expected to be approximately  $1\ \mu\text{s}$   
823 corresponding to the increased drift velocity in the He-based gas mixture. Note that the  
824 readout electronics are located outside the cold (77K) region of the detector.

825 The selection of the chip for the readout system will be changed if the drift time exceeds  
826 the capabilities of the APV25. The 25 ns APV readout has been shown to provide timing  
827 resolution better than 8 ns [65]. Given the expected  $5\ \mu\text{s}$  time range required for this  
828 experiment, the APV chip may not be optimal for this experiment. On the other hand,  
829 the DREAM chip, recently developed by the Saclay group, offers the time range we need  
830 and gives the flexibility to optimize parameters as needed for this experiment. A time  
831 resolution as low as 4 ns was recently demonstrated [66] in the LHCb GEM chamber  
832 with a similar readout where the GEM signal was first integrated and then digitized. For  
833 this proposal we have assumed 10 ns timing resolution, and we continue to follow new  
834 improvements being made to both the APV25 and DREAM chips.

835 The SRS system consists of the following components:

- 836 • APV-25 hybrid cards mounted on the detector. These cards contain the 128 chan-

837 nel APV-25 chip which reads data from the detector, multiplexes the data, and  
838 transmits analog to the ADC card.

839 • SRS ADC unit that houses the ADC chips that de-multiplex data and convert into  
840 digital format.

841 • SRS FEC card which handles the clock and trigger synchronization. A single FEC  
842 and ADC card combination has the capability to read data from up to 16 APV  
843 hybrid cards.

844 • Scalable Readout Unit (SRU), an optional component not shown in the figure,  
845 which distributes the clock and trigger synchronization to the FEC cards. One  
846 SRU handles communication between multiple (up to 40) FEC cards and the data  
847 acquisition computer.

848 • The data acquisition computer, which could be part of a larger DAQ system as one  
849 of the readout controllers.

850 Work is currently underway to incorporate the SRS system into the CODA data  
851 acquisition framework at JLab. Our plan is to be as compatible to the existing SBS GEM  
852 tracker module readout as possible.

853 **2.3.1 Target cell**

854 The proposed TDIS target inside the RTPC is significantly different from those previously  
 855 utilized. The target vessel is here a cylinder with an inner radius of 5 mm and 40 cm long.  
 856 It can be considered as a self-supporting balloon. The target will be gaseous Hydrogen  
 857 or Deuterium at 77 °K and 1 atm. In order to minimize the energy loss of the protons  
 858 of interest, we have reduced the material of the target wall as much as possible, down to  
 859 10 micrometers of aluminum. The larger diameter of the cell and the aluminum walls are  
 860 necessary given the high luminosity of the proposed experiment. The lower temperature  
 861 of the target (liquid nitrogen) and increased length of the cell allow reduction of the gas  
 862 pressure in the target (from 7 atm used in BONUS) to 1 atm.

863 The resulting threshold and energy loss for low energy protons are presented in Tab. 2,  
 864 as calculated by our Geant4 Monte Carlo model of the RTPC. This is a modification of  
 865 the Monte Carlo successfully utilized to analyze the BONUS experiment.

p(MeV/c)	50	75	100	150	225	325
$E_{kin}$ (MeV)	1.33	3.00	5.31	11.9	26.6	54.7
90 deg						
at TargetWall	1.24	2.95	5.28	11.9	26.6	54.7
after TargetWall	0.75	2.71	5.13	11.8	26.6	54.7
after Cathode		2.43	4.97	11.7	26.5	54.6
at 1st GEM			4.47	11.6	26.4	54.6
45 deg						
at TargetWall	1.21	2.93	5.27	11.9	26.6	54.7
after TargetWall	0.45	2.59	5.06	11.8	26.5	54.6
after Cathode		2.11	4.82	11.7	26.5	54.6
at 1st GEM				11.4	26.4	54.6

Table 2: Monte Carlo results for kinetic energy loss of protons starting at the indicated momenta on top line, presented for various positions as the protons encounter structures while radially traversing the RTPC.

866 The actual energy loss through the target gas and walls, as well as through the various  
 867 materials in Tab. 2, depends on the proton track angle when encountering the material.  
 868 Fig. 17 depicts Monte Carlo results for protons escaping the target, demonstrating this  
 869 angular dependence for initial proton angles as well as the minimum momentum threshold  
 870 ( $\gtrsim 56$  MeV/c) for the experiment. These threshold particles just barely penetrate the  
 871 cathode.

872 **2.3.2 RTPC Calibration**

873 The proposed measurement of the tagged DIS cross section will require good knowledge of  
 874 the various detector acceptances and efficiencies. The fully inclusive electron-proton and  
 875 electron-deuteron cross sections are well known from experiments in this kinematic regime  
 876 at Jefferson Lab and SLAC [67]. Comparing our untagged DIS measurements with these

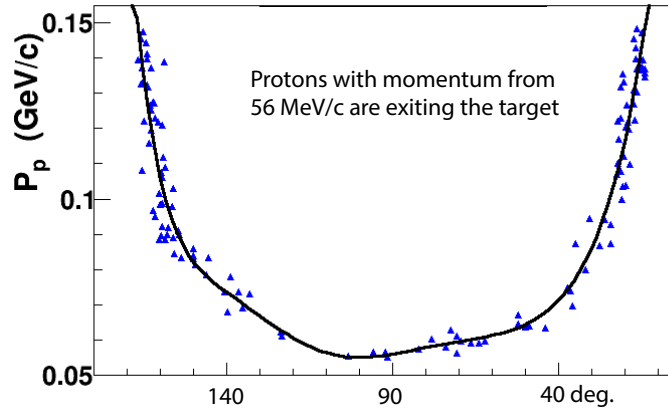


Figure 17: Minimum proton momentum as a function of angle for protons exiting the RTPC target.

877 data will allow for precision checks of the acceptance, efficiency, and other corrections  
 878 used for the SBS electron spectrometer analysis.

879 The RTPC will also require study and calibration. The BONUS experiment was not  
 880 able to make precise acceptance and efficiency corrections to the RTPC data to measure  
 881 the neutron cross section directly using the tagging technique, but rather had to simulate  
 882 as well as normalize to a model  $F_2^n/F_2^d$  ratio for an assumed-known kinematics within the  
 883 data set. This contributed significantly to the uncertainty of the measurement [68]. We  
 884 could perhaps employ a similar approach, but suggest also that different quantities may  
 885 be used as well to extract the RTPC acceptance and efficiency.

886 Some initial calibration can be done by using the copious proton tracks from elas-  
 887 tic electron-proton scattering. At production luminosity there will be several accidental  
 888 elastic proton tracks distributed evenly along the target for in every  $e - p$  DIS event.  
 889 These protons are well separated from the protons of interest because, to be at the same  
 890 momentum but generated by elastic events, they are necessarily kinematically directed  
 891 almost perpendicular to the beam.

892 It will be particularly productive to use quasi-elastic electron scattering from the  
 893 deuteron for the RTPC calibration. The energy and direction of the spectator proton may  
 894 be determined in a quasi-elastic reaction using a scattered electron in the SBS in combi-  
 895 nation with a neutron measured with the (relocated) SBS Hadron Calorimeter (HCAL).  
 896 The move-able HCAL detector would not be a part of the SBS for this experiment, and  
 897 could be placed beam right at optimum kinematics to record neutrons for this calibration  
 898 measurement. In such a way we can predict the distribution of protons of energy, for  
 899 instance 5-27 MeV (100-225 MeV/c), in the directions required for the RTPC calibra-  
 900 tion. A comparison between the measured proton spectra and the proton distributions  
 901 expected in the RTPC from quasi-elastic neutrons in HCAL will provide a check on the  
 902 RTPC proton acceptance and efficiency corrections. If the suggested quasi-elastic HCAL  
 903 neutron measurement is for some reason not available to the proposed measurement, it  
 904 will be possible though not optimal to work through simulation and geometry as was done  
 905 for the CLAS6 experiments.

906 The proposed calibration will be performed at an electron-nucleon luminosity of  $0.3 \times$   
 907  $10^{36}$  Hz/cm<sup>2</sup> with an electron beam energy 4.4 GeV and SBS angle at the same angle of  
 908 12 degrees as during the production TDIS run. The projected rate of electron-neutron  
 909 quasi-elastic events in SBS is around 1000 Hz. The average neutron momentum will be  
 910 970 MeV/c. Using HCAL located at a distance of 15 meters (60 degrees relative to the  
 911 beam direction) we estimated that the coincidence  $e - n$  rate will be approximately 70-  
 912 80 Hz. Neutron momentum will be within a cone with an average angle relatively the  
 beam of 60° an opening of  $\pm 4^\circ$ . At such a low luminosity the spectator protons will be

### Electron arm – SuperBigbite

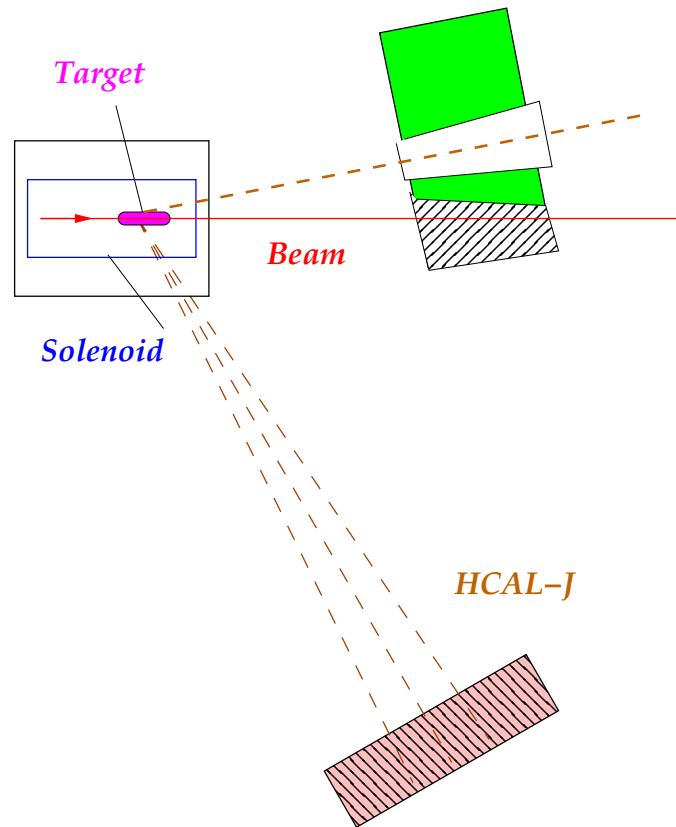


Figure 18: Setup for RTPC calibration

913 easy to identify and use for RTPC calibration. One day of such a measurement provides  
 914 more than 6 million tagged proton events which would allow detailed study of RTPC.  
 915

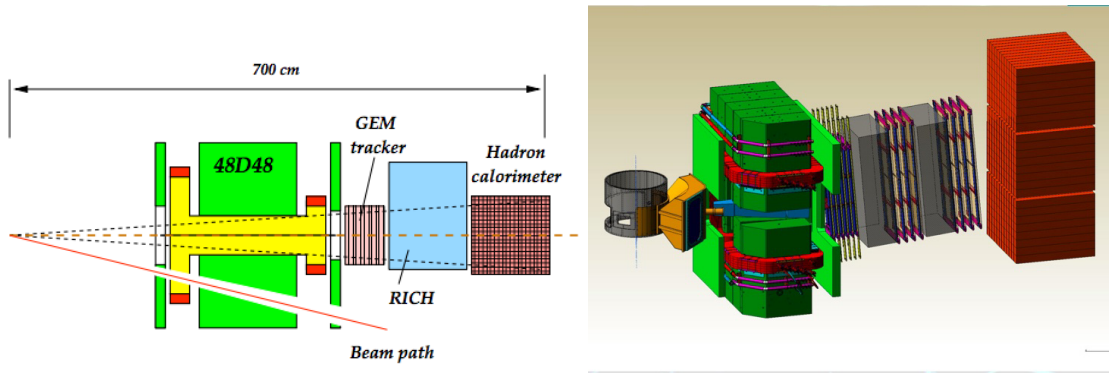


Figure 19: A schematic (left) and a CAD drawing (right) of the Super Bigbite Spectrometer

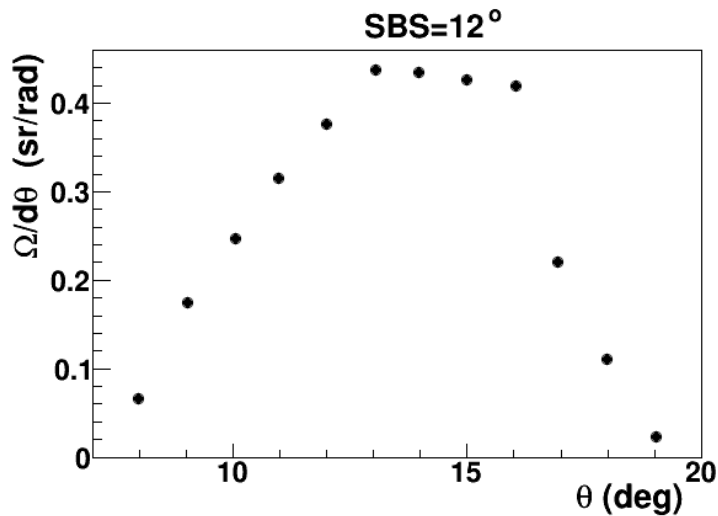


Figure 20: Solid angle vs. polar angle at the 12° SBS position.

## 916 2.4 The Super Bigbite Spectrometer

917 The Super Bigbite Spectrometer (SBS), currently under construction and fully funded by  
 918 DOE NP, consists of a dipole and a modular detector package. An important feature of  
 919 the SBS is a beam path through the opening in the right side yoke of the magnet, which  
 920 allows it to be placed at forward angles as small as 3.5°. For the proposed experiment  
 921 the SBS magnet (front face of the yoke) will be placed 2.0 m from the target allowing  
 922 for a 50 msr solid angle around a 12° central angle. The large out-of-plane angle of SBS  
 923 provides significant coverage in azimuthal angle (about 20% of  $2\pi$ ). Figure 20 shows  
 924 the spectrometer solid angle vs. scattering angle for such a setting. In the proposed  
 925 experiment we plan to use the large GEM-based chambers currently under construction  
 926 for the SBS  $G_E^p$  experiment polarimeter as the main tracking planes. We plan to use five  
 927 out of ten constructed planes and concentrate the readout electronics of all ten planes in  
 928 those five. These chambers will each cover a 60 cm x 200 cm area, and the concentrated  
 929 electronics will then allow reading of every readout strip. These chambers were tested in

930 such a configuration and a spatial resolution of 60-70  $\mu\text{m}$  was obtained.

931 The combination of an electromagnetic calorimeter (the CLAS-6 Large Angle Calorimeter  
932 or LAC) and threshold gas Cherenkov counter (the HERMES RICH or GC-SBS) will  
933 be used for trigger and particle identification purposes. The LAC is discussed in some  
934 detail below. The Gas Cherenkov will be a straightforward modification of the existing  
935 ring imaging Cherenkov (RICH) detector planned to be utilized in the approved SBS  
936 experiment E12-09-018 - basically filling the tank with  $\text{CO}_2$ . The combination of these  
937 two detectors will be sufficient for the electron particle identification purposes of this  
938 experiment.

#### 939 2.4.1 CLAS6 Large Acceptance Calorimeter

940 The SBS was originally designed to be a hadron spectrometer. In order to use SBS as  
941 an electron spectrometer with good pion rejection capability we will replace the hadron  
942 calorimeter with the safely salvaged Large Acceptance Calorimeter (LAC) from the CLAS6  
943 detector.

944 The conceptual drawing of the internal structure of the LAC is shown in Fig. 21.  
945 The LAC module has a rectangular shape with a sensitive area of  $217 \times 400 \text{ cm}^2$  and  
946 consists of 33 layers, each composed of a 0.20 cm thick lead foil and 1.5 cm thick NE110A  
947 plastic scintillator bars. The total thickness is about 12.9 radiation lengths or 1 hadronic  
948 absorption length. Each scintillator layer is protected from contact with the lead by 0.02  
949 cm thick Teflon foils. The width of the scintillators is roughly 10 cm and increases slightly  
950 from the inner layers toward the outer layers to provide a focusing geometry. Scintillators  
951 in consecutive layers are rotated by 90 degrees to form a  $40 \times 24$  matrix of cells with  
952 area approximately  $10 \times 10 \text{ cm}^2$ . The module is vertically divided into two groups: an  
953 inner (first 17 layers) and an outer (16 layers) groups. Each group has its own light  
954 readouts. Scintillators lying one on top of the other with the same orientation form a  
955 stack. For each stack the light is collected at both ends separately using light guides  
956 coupled to EMI 9954A photomultiplier tubes. For each module there are 128 stacks and  
957 256 photomultipliers [70].

958 The LAC energy resolution for electromagnetic showers is  $7.5 \pm 0.2 \%$  [70]. Combined  
959 with CLAS, the pion contamination is less than 1% for cuts that give a detection efficiency  
960 of 95% for 2 GeV electrons.

961 A Geant4 simulation has been performed to study the LAC for this proposal. Fig. [22]  
962 shows the LAC in this Geant4 program. Our results indicate that grouping the first 17  
963 layers into the inner part should provide a good choice and that the particle identification  
964 be cut should include two parts:  $E_{tot}/P > 0.33$  and  $E_{in}$  cuts. Here,  $E_{tot}/P$  is the fraction  
965 of energy deposited in the LAC compared to the total momentum of the particle, and  
966  $E_{in}$  is the energy deposited in the inner layers only. The optimum cut value for  $E_{in}$  is  
967 momentum dependent. The results indicate that the pion rejection fractions will be 89%,  
968 92%, 95% and 96.5% for particles with momenta 1.0, 2.0, 5.0 and 8.0 GeV/c, respectively.

969 The pion to electron rate in the SBS is shown in Fig. 23, for the proposed hydrogen  
970 target. In the scattered energy range below 3 GeV the combined (RICH and LAC)  
971 pion rejection will be above 10,000, which will reduce the pion contamination to below  
972 1%. For energies above 3 GeV the rejection from the gas Cherenkov will be reduced.

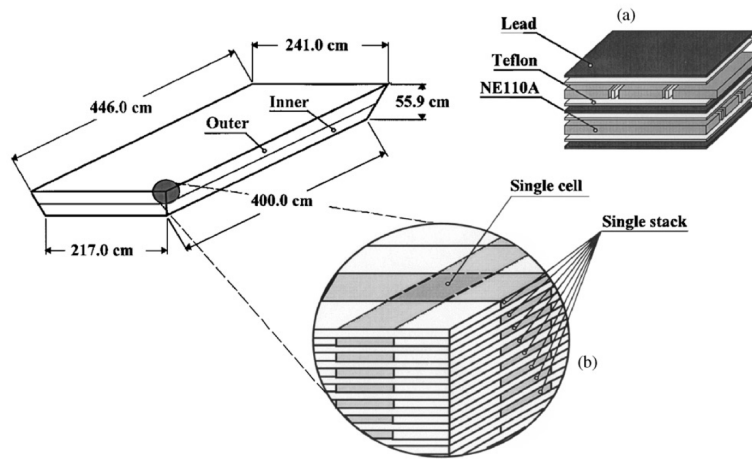


Figure 21: The conceptual drawing of the internal structure of the LAC module.

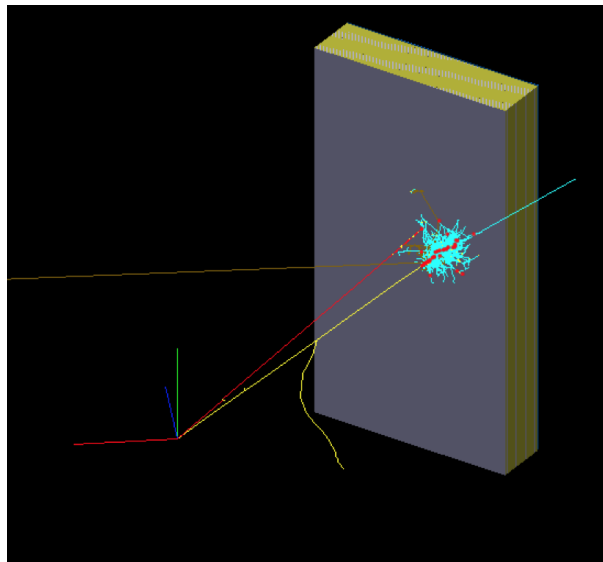


Figure 22: The LAC in the Geant4 Simulation. The red trajectory is a pion and the yellow is an electron.

973 However, rejection in the calorimeter for such energies will be at least a factor of 100  
 974 (when the particle momentum is used in the analysis) and the pi-to-e ratio is also reduced.  
 975 Considering all of the above, the uncertainty on the pion contribution to the final event  
 sample is expected to be on the level of 1% or less.

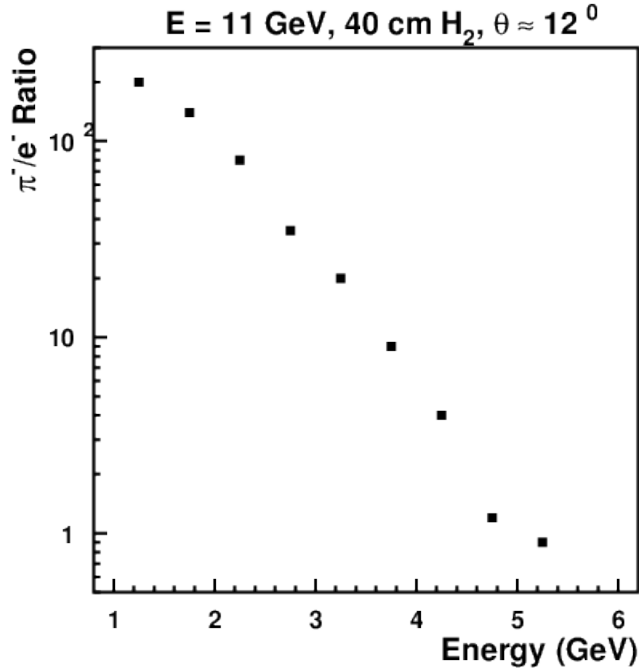


Figure 23: A pion to electron ratio in the SBS spectrometer for the hydrogen target.

976

#### 977 2.4.2 Super Bigbite Trigger and DAQ

978 It is proposed that the Level-1 trigger will be formed using the total energy deposition  
 979 in the LAC and the Level-2 trigger will use correlation between the coordinates of the  
 980 signals in the LAC and GC-SBS and energy deposition information from two layers of  
 981 LAC. The RTPC will be readout for any kind of trigger.

982 **Pipeline Electronics** For the SBS experiment GEP the proton trigger is achieved  
 983 digitally using the Jefferson Lab Lab pipeline electronics. All of the 288 channels of the  
 984 hadron calorimeter (HCAL) are continuously sampled at 250 MHz. The data of each block  
 985 is sent to a crate trigger processor where the clustering algorithm computes the sums of  
 986 16 adjacent blocks and produces a trigger if one cluster is above threshold. This process  
 987 takes about 700 ns. Once the trigger is generated, the data from the FADC is looked  
 988 back up in the pipeline memory to be read out. Since the LAC has only 216 channels we

989 propose to reuse the ECAL trigger electronics and readout to generate the single shower  
990 trigger. The singles shower trigger will also be prescaled in order to study the Cherenkov  
991 counter efficiency. The 288 channels of HCAL would require two crates with multiplexed  
992 analog signals in the overlap region.

993 **Large Angle Calorimeter** The Large Angle Calorimeter is constituted of layers of  
994 scintillator and lead. For this experiment the sensitive area will be limited to 1.8m x  
995 3.6m to match the SBS acceptance. The detector is arranged in two parts, the front part  
996 containing 16 layers and the back part containing 17 layers. This corresponds to a total  
997 number of 256 PMTs. For the LAC PMTs summing we plan to reuse electronics of the  
998 ECAL calorimeter (an electron arm of the GEP experiment). The energy deposited in  
999 two layers of the calorimeter will be estimated by summed signals of adjacent paddles.  
1000 First, we produce the overlapping sums in the both layers. It would be 58 signals for  
1001 the layer-1 and 58 for the layer-2. Then the signals of two layers will be combined. The  
1002 resulting  $19(X) + 39(Y)$  analog signals will be discriminated and form (via logical OR) a  
1003 Level-1 trigger. These 58 logical signals will be used in the FPGA scheme for geometrical  
1004 matching of the pulses in GC-SBS and LAC as a part-1 of the Level-2 trigger. The 19  
1005 analog signals from each layer will be analyzed by using the three FADC modules for  
1006 suppression of the charge pion events as a part-2 of the Level-2 trigger.

1007 **SBS Cherenkov Detector** In order to suppress the trigger rate originated by pions  
1008 and photons, we are planning to modify the RICH counter under commissioning for the  
1009 SBS transversity experiment. It will require removal the aerogel (or blocking light from  
1010 it) and substituting with  $\text{CO}_2$  and using it as a threshold Cherenkov detector. The RICH  
1011 counter has an array of 2000 PMTs as it will be used in the approved SBS transversity  
1012 experiment. A 8(x2) channel amplifier discriminator board was developed by Glasgow  
1013 University based on the NINO chip. Using discriminated signals provided by this board,  
1014 with the amplitude over threshold of the signal integrated in the width of the logic signal,  
1015 we would need 125 boards. The resulting 250 logical pulses will be used in the FPGA  
1016 scheme for summed areas of geometrical match.

1017 **GEM Tracker Electronics** The GEM signals for the multiple SBS tracking planes  
1018 will be read using the APV25 readout and the SRS system as described above. This will  
1019 be used for the RTPC in the same way that it is currently planned for the GEM trackers  
1020 of Super Bigbite.

## 2.5 Simulations of the Radial Time Project Chamber

The impact of beam-related background processes on the RTPC operation has been assessed using a simulation based on a recent release of Geant-4 (4.10.0.p03) [71]. The simulation considers (Fig. 24) a “straw” target of radius 5 mm and length 400 mm, held in a 10  $\mu\text{m}$  thick Al cylinder, with 20  $\mu\text{m}$  Al end windows, and filled with 1 atm of  $\text{H}_2$  or  $\text{D}_2$  gas. This cell is surrounded by the He gas of the RTPC, at a pressure of 0.15 atm, contained within a volume of 150 mm radius. Both the straw target and the He volume are maintained at a temperature of 77°K.

A ring of 127  $\mu\text{m}$  radius, gold-plated Al field wires divides the He volume into an insensitive region (He-inner) at radii  $r < 50$  mm and a sensitive region (He-outer) at radii  $50 < r < 150$  mm. The electrons of ionization produced in He-inner region are swept to the target cell and the ions collected by the wire ring. Ionization produced in He-outer is moved by the radial electric field to an outer ( $r > 150$  mm) triple GEM detector with pixel readout. Calculations have also been made for a target pressure of 2 atm and temperature 25°K which provide projected luminosity of experiment. The density of the He gas in the RTPC has been fixed at  $9.75 \times 10^{-5}$  g/cm<sup>3</sup> which corresponds to a pressure of 0.15 atm at 77°K. Essentially backgrounds have been found to scale with the thickness of the target.

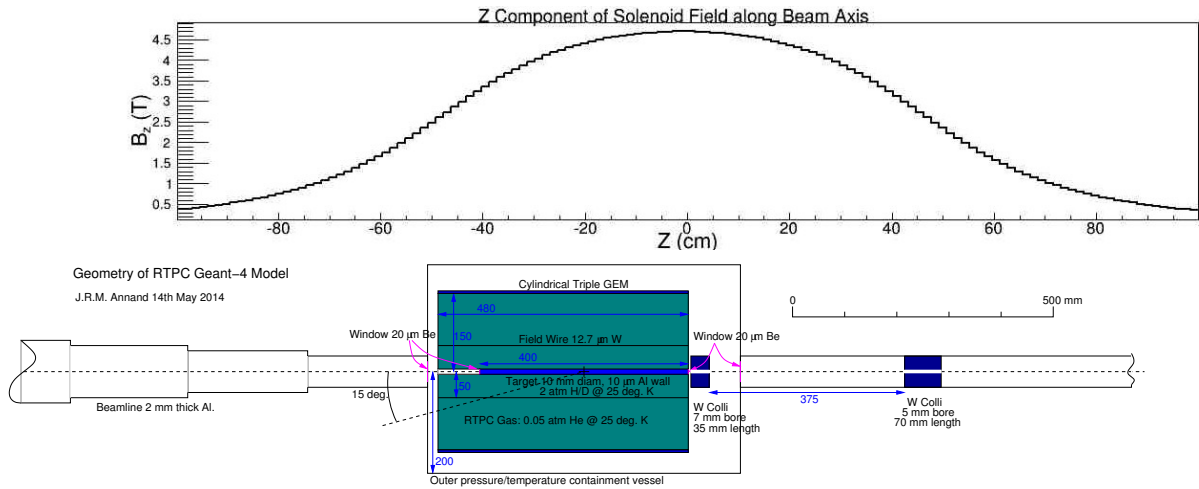


Figure 24: Top: the  $z$ -dependence of the longitudinal component of the S3 solenoid magnetic field  $B_z$ . Bottom: Geometry of the MC simulation of background processes. **Note:** the direction of the electron beam from the right to the left.

Operating with the target at 77°K and 1 atm, an electron beam current of  $\sim 60 \mu\text{A}$  will produce a luminosity  $2.9 \times 10^{36} \text{cm}^{-2}\text{s}^{-1}$ . The largest background will be observed in the vicinity of the target. This comes mainly from Møller scattering of the incident electrons, with smaller contributions from bremsstrahlung and pair production. Most of the background electrons have low energy and are confined inside the insensitive region of the RTPC (He-inner) by the solenoid magnetic field.

Figure 25(A) shows the radial distribution of energy deposited in the target and RTPC for different magnetic field strengths. The calculation has been made with  $8 \times 10^8$  incident 11 GeV electrons, for uniform fields of 1.0, 2.0, and 4.0 T, as well as the “S3” solenoid

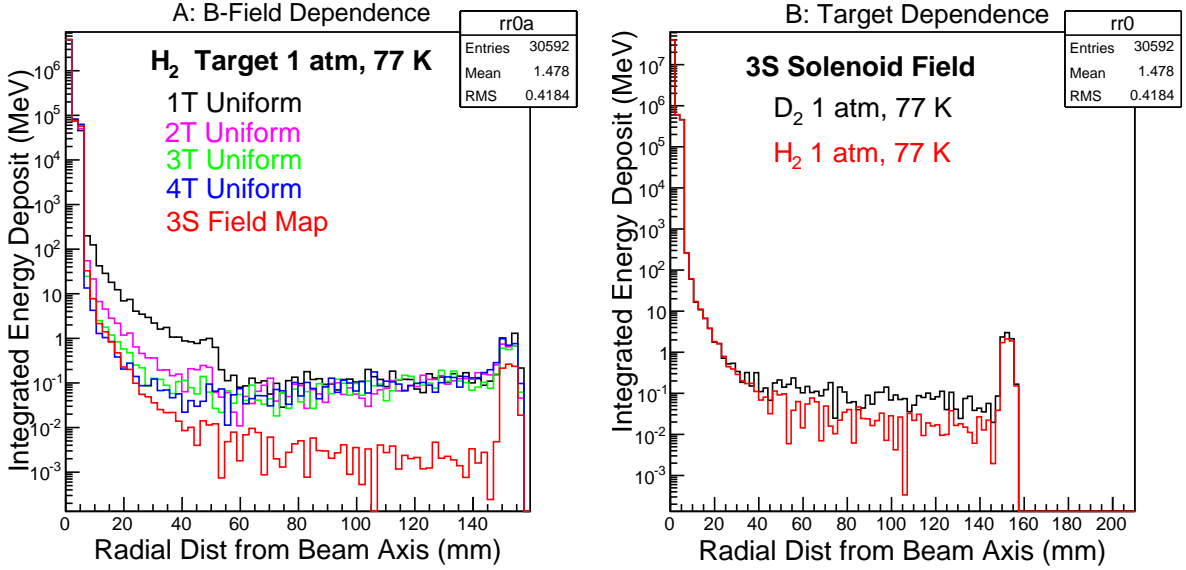


Figure 25: A: confinement of Møller energy deposit for a 1 atm, 77K target and various magnetic field configurations. B: S3 solenoid field map and different targets. Simulations have  $8 \times 10^8$  incident electrons of 11 GeV energy.

1047 field map (Fig.24) calculated in TOSCA. In the region of the target the maximum S3  
 1048 longitudinal field is in excess of 4 T.

1049 As the field strength is increased the radial rate of decrease of the energy loss becomes  
 1050 steeper, in the He-inner. However, there remains a background in He-outer which is not  
 1051 suppressed by increasing the field strength. A small fraction,  $\sim 5\%$ , of this can be at-  
 1052 tributed to intermediate bremsstrahlung in the target region, followed by pair production.  
 1053 But, most originate from interactions of the beam downstream from the target (Fig.24).

1054 It is thus important that the magnetic field extends sufficiently in  $z$  and that the beam  
 1055 line has sufficiently large diameter to accommodate the increasing lateral spread in the  
 1056 exit beam. Note that the larger backgrounds observed with uniform fields, compared to  
 1057 S3, is largely due an unphysical sharp cutoff at the boundary of the uniform field.

1058 The present calculations have been made both with the field-map centered on the  
 1059 target and with the field map displaced 200 mm upstream (as shown in Fig. 24). The exit  
 1060 beam line is stepped periodically to larger radii, traveling downstream from the target.  
 1061 Increasing the expansion of the exit beam line beyond that depicted in Fig. 24 has an  
 1062 insignificant effect on the He-outer background if an electron beam radius of 0.5 mm  
 1063 is used. The integrated energy loss in He-outer has some dependence on the beam-line  
 1064 material, but 2-4 mm thickness Al gives reasonable results. Upstream from the target a  
 1065 dual W collimator is installed to suppress increased background produced by an off-axis  
 1066 beam.

1067 Figure 25(B) compares the radial energy distribution, calculated with the S3 field  
 1068 map, for 1-atm H<sub>2</sub> and D<sub>2</sub> targets. The mean energy losses per incident 11 GeV electron  
 1069 are given in Table 3 for a 1 atm, 77°K target. A column “ $r \leq 50$  mm” gives the mean  
 1070 energy loss in the target and He-inner and column “ $50 < r \leq 150$  mm” the mean energy

1071 loss in He-outer. There appears to be no significant penalty (in terms of electromagnetic  
 1072 background) from substituting Al for Be as the window material or from moving the  
 1073 solenoid magnet 200 mm upstream.

1074 The MC generated data have also been analyzed on an event-by-event basis and column  
 1075 “Rate” of Table 3 gives the rate at a luminosity of  $2.9 \times 10^{36} \text{ cm}^{-2}\text{s}^{-1}$  of electron events in  
 1076 the sensitive region which produce a mean  $dE/dx$  along the track exceeding 0.1 keV/mm.  
 1077 Protons of interest would be expected to produce a larger  $dE/dx$ . Detectable rates in  
 1078 the sensitive area of 22.8 MHz and 40.8 MHz for the H<sub>2</sub> and D<sub>2</sub> targets respectively will  
 1079 contribute to the occupancy of the readout pads in the GEM detector, but the electron  
 1080 track loci are quite different from those produced by protons .

Target	Mean $E_{dep}$ (MeV)	Mean $E_{dep}$ (MeV)	Rate
	$r \leq 50 \text{ mm}$	$50 < r \leq 150 \text{ mm}$	(MHz)
H <sub>2</sub>	0.0509	$0.377 \times 10^{-8}$	22.8
D <sub>2</sub>	0.0509	$0.831 \times 10^{-8}$	40.8

Table 3: Electromagnetic background calculations for H<sub>2</sub> and D<sub>2</sub> targets operated at 1 atm and 7K. The magnetic field is S3 solenoid offset by 200 mm, as in Fig. 24. The target windows are 20 μm Al.

1081 Figure 26 compares the transverse distribution of energy deposited by secondary elec-  
 1082 trons (A) and protons (B). In the panel A, outside of the central region, there are  $\sim 5$   
 1083 tracks which would reconstruct as originating from the target, with a radius of curvature  
 1084 consistent with  $p \sim 250 \text{ MeV}/c$  and negative charge. The outer ring of energy deposit is  
 1085 from photon conversion in the GEM detector. In B the photo proton tracks originate from  
 1086 the target region. For the deuterium target relatively large numbers of low momentum  
 1087 protons are produced as shown by the tightly curved tracks of radius a few cm.

1088 Although electromagnetic processes are the dominant, potential source of background,  
 1089 electrons are effectively contained by the solenoid field and those impinging on the He-  
 1090 outer sensitive region generally have a relatively low  $dE/dx$ , compared to the low-momentum  
 1091 protons of interest to recoil tagging. Photo nuclear processes, on the other hand, have  
 1092 much lower cross sections, but at small electron scattering angles the high flux of quasi-  
 1093 real photons will produce large numbers of highly-ionizing protons in a similar momentum  
 1094 range to those of interest. Protons of momentum above  $\sim 50 \text{ MeV}/c$  will reach the He-  
 1095 outer sensitive region.

1096 Calculations of the momentum spectrum and angle dependence of photo protons was  
 1097 made using parametrized models. Code based on a fit to SLAC photo nuclear data [69]  
 1098 has commonly been used at JLab to calculate hadronic backgrounds produced in DIS.  
 1099 However the kinematic region spanned by the “Wiser fit” does not extend to the low  
 1100 momenta of interest here. The present calculations are largely based the EPC code [74],  
 1101 and model of various photonuclear processes for the materials in the path of the electron  
 1102 beam:

- 1103 • <sup>1</sup>H: elastic e-p scattering has been calculated (not in EPC) from the Mott cross  
 1104 section and the Kelly parametrization [75] of the Sachs form factors.

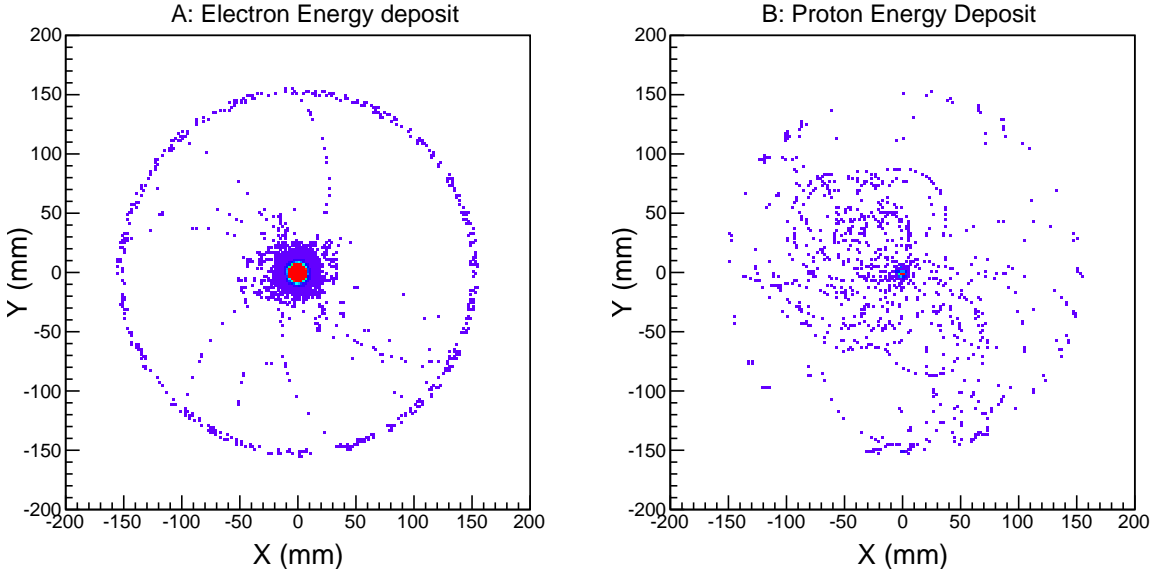


Figure 26: A: radial dependence of integrated energy loss for electrons, B: for photo protons.

- 1105 •  $^2\text{H}$  and  $^{27}\text{Al}$ : nucleon recoil after quasi-free electron scattering.
- 1106 •  $^2\text{H}$  and  $^{27}\text{Al}$ : deuteron (or quasi-deuteron) photodisintegration by quasi-real photons.
- 1107
- 1108 •  $^1\text{H}$ ,  $^2\text{H}$  and  $^{27}\text{Al}$ : recoiling nucleons after pion photoproduction via  $\Delta$  excitation.

1109 EPC is quoted [74] as valid for 0.5 - 5 GeV electrons, but its predictions compare reasonably with forward angle charged particle production by an 18 GeV electron beam at SLAC. It was used to generate a grid of cross section values  $\sigma(p_p, \cos\theta_p)$ ,  
 1110  $p_p = 50 - 1000$  GeV/c,  $\cos\theta_p = -1.0 - +1.0$ , which were stored in a ROOT 2D histogram incorporated into the Geant-4 RTPC model. Photo proton events were generated  
 1111 by sampling  $p_p$  and  $\cos\theta_p$  randomly, using the 2D histogram, and then tracked through the Geant-4 model of the RTPC. The 3S field map was employed.  
 1112  
 1113  
 1114  
 1115

1116 Fig. 27 displays the angle and momentum dependence of photo proton intensity for  $^1\text{H}$  and  $^2\text{H}$  targets. Relative to  $^1\text{H}$ ,  $^2\text{H}$  produces large numbers of low momentum protons and this intense background extends to all angles. The dark rectangles indicate  
 1117 the kinematic region of interest for recoil tagging. Fig. 28 compares the momentum dependence of the rate of photo protons produced in the  $^1\text{H}$  and  $^2\text{H}$  targets, at a luminosity  
 1118 of  $2.9 \times 10^{36} \text{ cm}^{-2}\text{s}^{-1}$ , integrated over angle ranges of interest for TDIS. Both Fig. 28 and  
 1119 27 refer to protons which reach the sensitive He-outer region of the RTPC. Histograms have been filled using reconstructed values of  $p_p, \cos\theta_p$  on arrival at He-outer.  
 1120  
 1121  
 1122  
 1123

1124 Table 4 gives the proton rates in the sensitive region of the RTPC, computed using the procedure described above, at a luminosity of  $2.9 \times 10^{36}$ . For  $^2\text{H}$  The high rates at low  
 1125 momentum are mainly due to quasi-free scattering and quasi-deuteron processes. For  $^1\text{H}$   
 1126 the cuts in angle remove elastic scattering events and the remaining rate arises from pion  
 1127

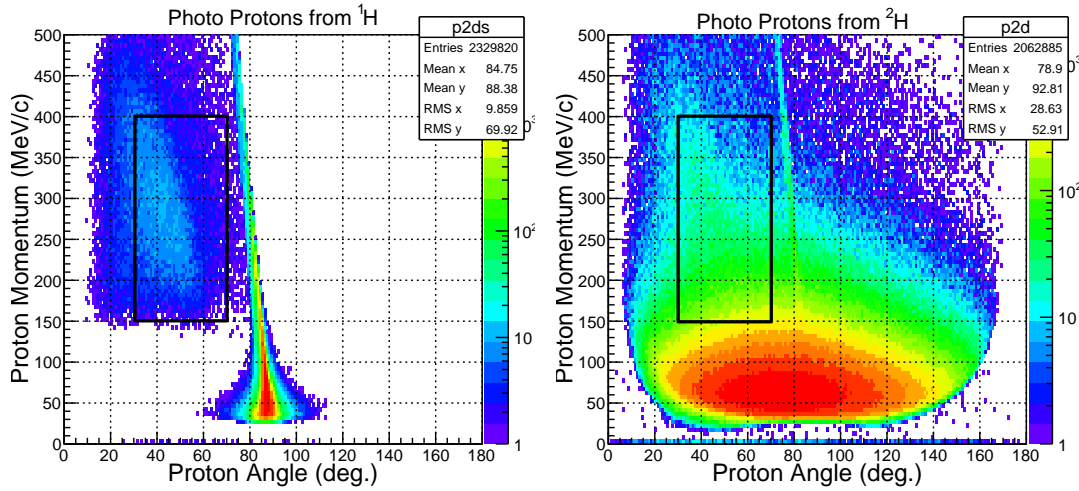


Figure 27: Comparison of momentum and angle dependence of photo protons produced in  $H_2$  and  $D_2$  targets and detected in He-outer. The targets were at 1 atm,  $77^\circ\text{K}$ . The rectangles denote the kinematic regions of interest for recoil tagging.

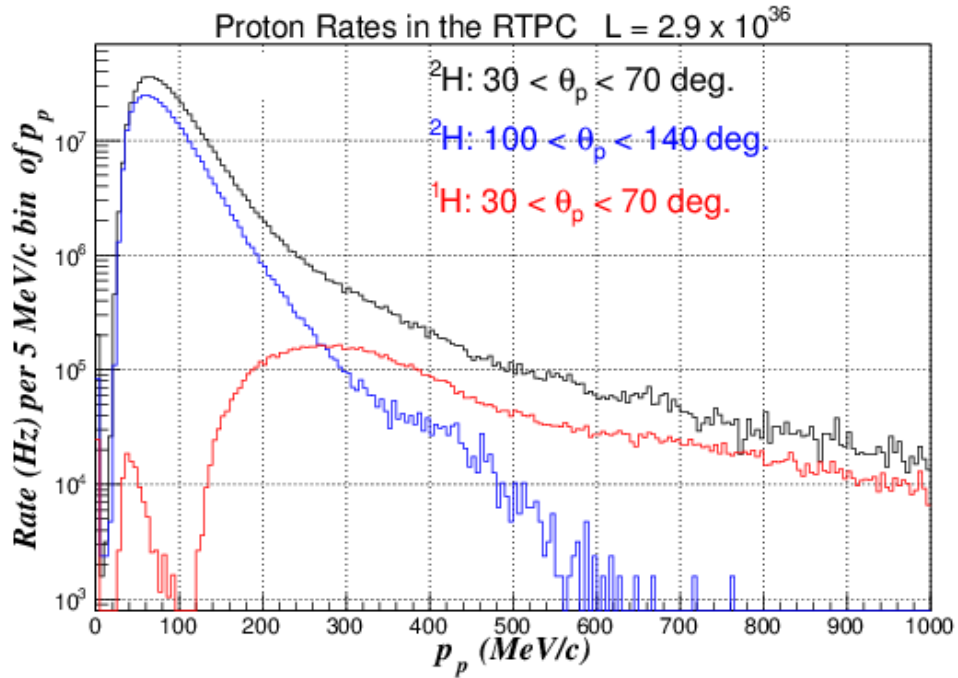


Figure 28: Rate dependence on momentum for protons produced in  $^1H$  and  $^2H$  targets by photo nuclear processes and detected in He-outer. Black:  $^2H$ , proton angle range  $30 - 70^\circ$ . Blue:  $^2H$ , proton angle range  $100 - 140^\circ$ . Red:  $^1H$ , proton angle range  $30 - 70^\circ$ . The luminosity is  $2.9 \times 10^{36} \text{ cm}^{-2} \text{ s}^{-1}$ .

1128 photoproduction. For the  $^{27}\text{Al}$  windows, after a vertex cut to remove events reconstructed

1129 as originating  $< 10$  mm from the windows, the predicted rates in the kinematic regions  
 1130 of interest are relatively small.

Target	$\theta_p$ (deg.)	$70 < p_p < 250$ (MHz)	$p_p > 250$ (MHz)	$150 < p_p < 400$ (MHz)
$^1\text{H}$	30 - 70	2.3	7.4	6.3
$^2\text{H}$	30 - 70	357	20.1	64
$^2\text{H}$	100 - 140	204	3.1	—
$^{27}\text{Al}$	30 - 70	0.37	0.0	0.05
$^{27}\text{Al}$	100 - 140	0.10	0.0	—

Table 4: Proton Rates in the sensitive region of the RTPC after cuts have been made on proton angle and proton momentum.

1131 **Particle Identification** Analysis of step-by-step information along particle tracks pro-  
 1132 duced by the simulation have been analyzed to determine  $dE/dx$  in the RTPC gas  
 1133 for  $p$ ,  $\pi^+$ ,  $K^+$ ,  $e$ . Particles have been produced at angles  $\theta = 30 - 70^\circ$ , at position  
 1134  $z = 0.0 \pm 5$  mm, and at momenta  $p_{inc}$  of  $100 \pm 1$ ,  $250 \pm 1$  and  $400 \pm 1$  (MeV/c). Fig.29 dis-  
 1135 plays the resulting distributions at 250 MeV/c, for tracks with a total length greater than  
 1136 50 mm. The dotted line shows the position of the cut used to select proton events. Mean  
 1137 and rms values for  $dE/dx$  distributions are given in Tab. 5, along with the particle accep-  
 1138 tance after the conditions  $dE/dx > 0.5, 0.09, 0.05$  keV/mm for  $p_{inc} = 100, 250, 400$  MeV/c  
 1139 respectively have been applied. These thresholds lead to a  $K^+$  acceptance fraction of 1%.

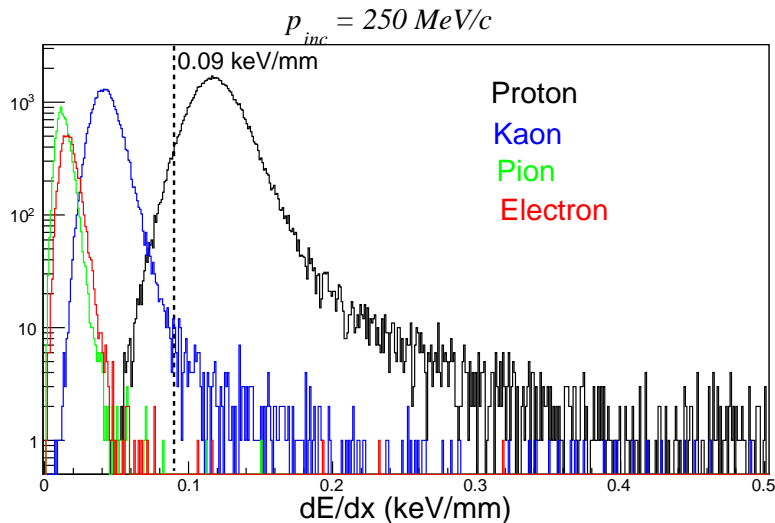


Figure 29:  $dE/dx$  for particles of momentum 250 MeV/c detected in the outer He volume of the RTPC.

1140

Particle	$p_{inc}$ (MeV/c)	$dE/dx$ Thresh. (keV/mm)	$p$	$\kappa^+$	$\pi^+$	$e$
Mean $dE/dx$ (keV/mm)	100	–	0.666	0.202	0.030	0.019
RMS $dE/dx$ (keV/mm)	100	–	0.130	0.046	0.008	0.006
Acceptance Factor (%)	100	0.5	100	1.0	0.04	0.00
Mean $dE/dx$ (keV/mm)	250	–	0.122	0.044	0.014	0.018
RMS $dE/dx$ (keV/mm)	250	–	0.028	0.012	0.005	0.006
Acceptance Factor (%)	250	0.09	95.5	1.0	0.02	0.07
Mean $dE/dx$ (keV/mm)	400	–	0.057	0.024	0.012	0.018
RMS $dE/dx$ (keV/mm)	400	–	0.015	0.008	0.005	0.006
Acceptance Factor (%)	400	0.05	68.2	1.0	0.19	0.22

Table 5: Particle-detection mean and rms  $dE/dx$  and acceptance after a cut on  $dE/dx$  has been applied.

1141 **2.5.1 Kinematics**

1142 The kinematics reach of the experiment was studied using an event generator built for  
 1143 the Geant4 Monte Carlo simulation. The event generator used a flat distribution in  $E_{e'}$   
 1144 from 0 – 11.0 GeV, and a flat distribution in  $\theta_{e'}$  from 5 to 45 degrees and  $\phi_{e'}$  of  $\pm 12$   
 1145 degrees, governed by the SBS acceptance. The  $x_{bj}$  and the  $Q^2$  is then calculated for the  
 1146 generated electrons. For the initial nucleon, the generator started with a proton at rest  
 1147 in the case of the  $^1\text{H}$  target target and a neutron with initial momentum based on the  
 1148 momentum distribution inside the Deuteron, in the case of the  $^2\text{H}$  target. The transverse  
 1149 momentum,  $P_T$  and  $z_p = \frac{q \cdot P'}{q \cdot P}$  of the recoil proton was generated with a flat distribution  
 1150 between 50 - 500 MeV/c and 0 - 1, respectively and a flat  $\phi$  distribution across  $2\pi$ . Finally  
 1151 the momentum and scattering angle of the recoil proton (s), the  $t$ ,  $y$  and  $x_\pi = x_{bj}/(1 - z_p)$   
 1152 were calculated for the generated events. The DIS cross section is calculated as a function  
 1153 of  $x_{bj}$  and  $Q^2$  using the proton/neutron parton distributions functions in CERNLIB. The  
 1154 TDIS cross section was calculated using the phenomenological pion structure function  
 1155 described in Appendix A and using the relation  $\sigma_{TDIS} = \sigma_{DIS} \times (f_2^{\pi N}/f_2^p)$ .

1156 Figs. 30 and 31 show the projected kinematics of the proposed experiment for Hydro-  
 1157 gen and Deuterium targets, where all plots have been weighted by the TDIS cross section.  
 1158 As noted earlier, the x range is determined by the low t range of interest, through the  
 1159 variables  $z_p$  and the low spectator momentum. This x range is, moreover, optimized for  
 1160 observation of pions events in the meson cloud. Once the x range is fixed, the  $Q^2$  range  
 1161 obtainable with the 11 GeV beam is also determined. While the latter is not very high,  
 1162 the kinematics are nonetheless clearly in the deep inelastic scattering regime – with  $W^2$   
 1163 values typically between 9 and 16  $\text{GeV}^2$ .

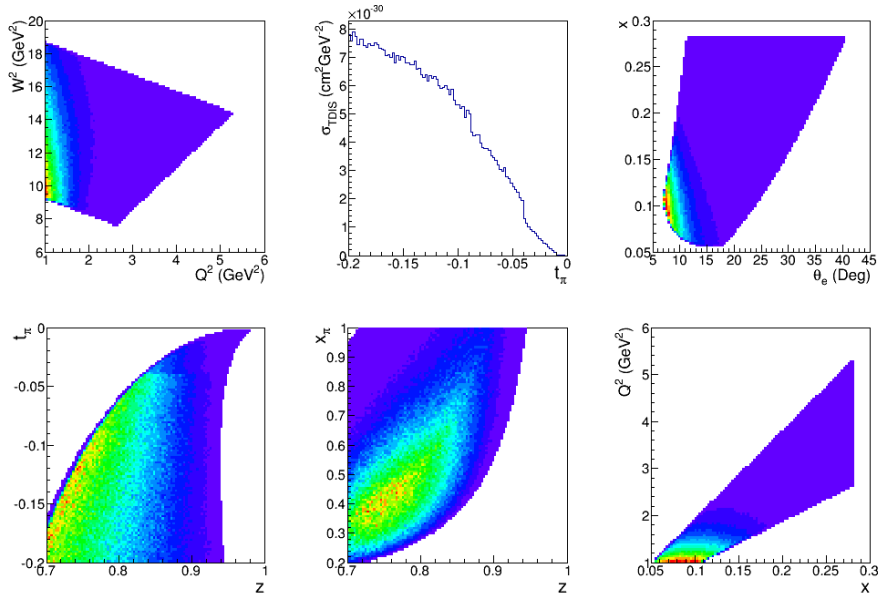


Figure 30: Kinematic coverage weighted by the TDIS cross section for a Hydrogen target.

1164 Figs. 32 shows the projected momentum and angular range of the recoil proton for the  
 1165 Hydrogen target and the Deuterium target. All plots have been weighted by the TDIS

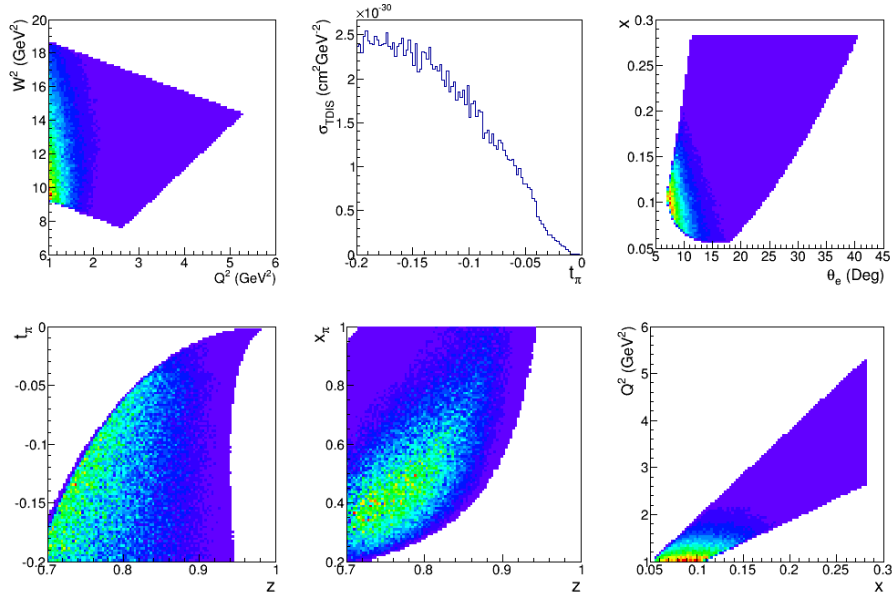


Figure 31: Kinematic coverage weighted by the TDIS cross section for a Deuterium target.

1166 cross section.

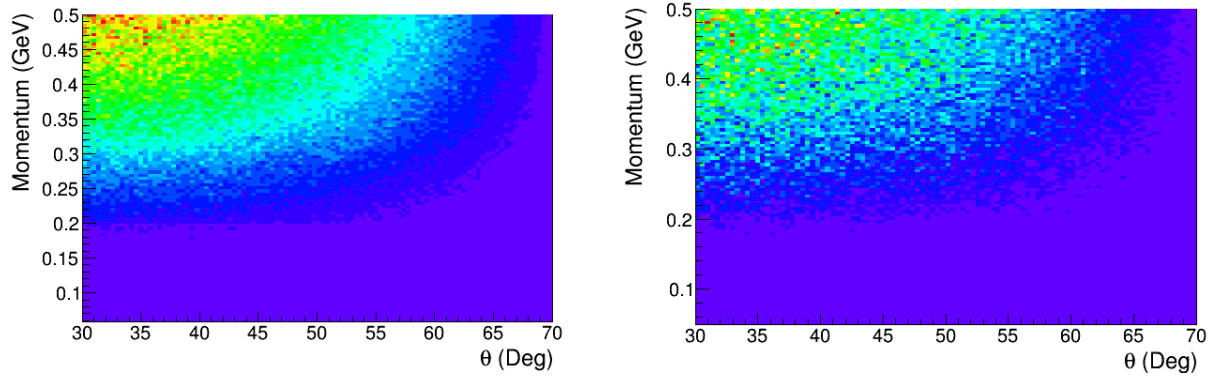


Figure 32: Recoil proton momentum vs angle weighted by the TDIS cross section, for the Hydrogen (left) and the Deuterium (right) targets.

1167 In Figs. 33 and 34 we have shown the TDIS yield in  $x$  vs  $z_p$  bins for 10 days of beam  
 1168 on a Hydrogen and a Deuterium target. As described in Sec. 3.1, the beam time request  
 1169 is based on being able to collect  $\sim 1\%$  statistics (after accounting for backgrounds) in the  
 1170  $x, z_p$  bin with the lowest yield.

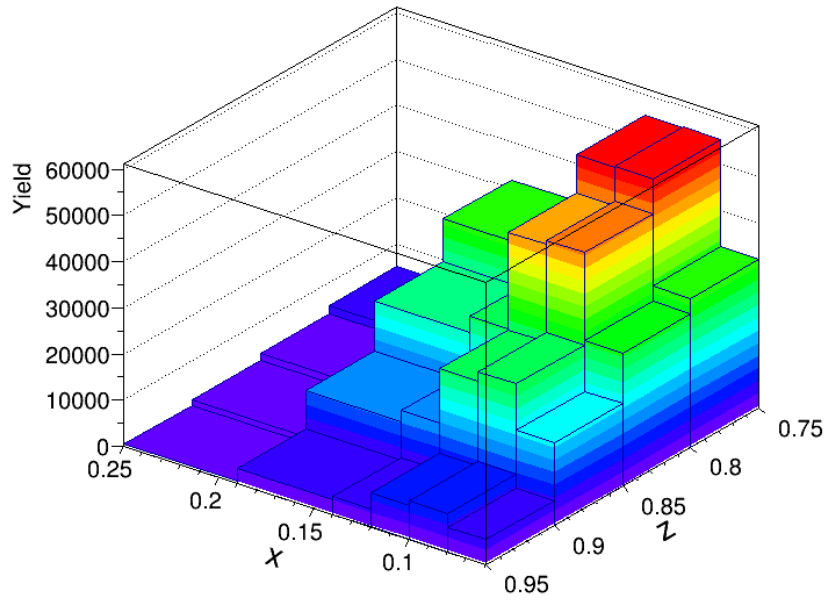


Figure 33: TDIS yields in  $x, z_p$  bins with 10 days of beam on the Hydrogen target.

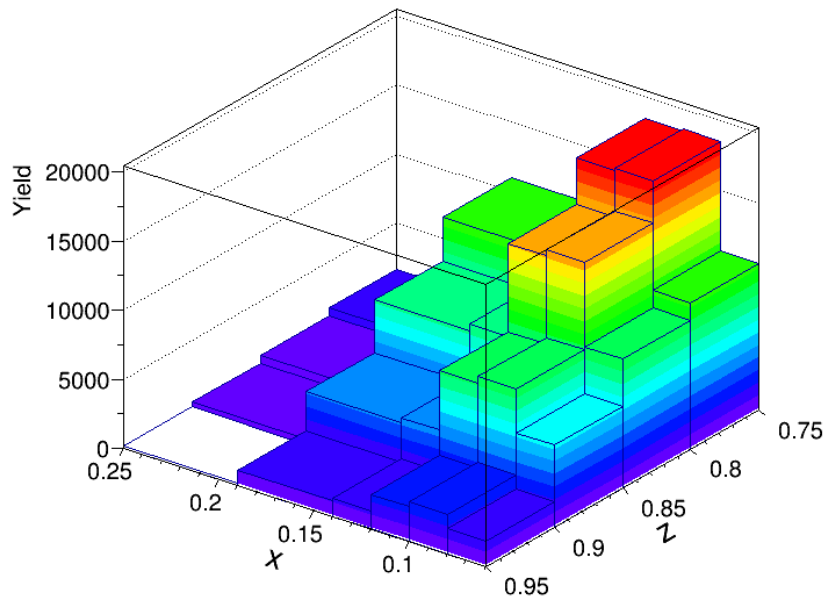


Figure 34: TDIS yields in  $x, z_p$  bins with 10 days of beam on the Deuterium target.

### 3 Projected Results

1171

1172 Fig. 35 shows the ratio of semi-inclusive structure function  $F_2^{(\pi p)}(x, \Delta|\mathbf{k}|, \Delta\theta_{p'})$  to the  
 1173 inclusive nucleon structure function  $F_2^p$  for the neutron (left) and proton (right) and with  
 1174 projected data from this proposal added. The statistical uncertainty on the projected  
 1175 data is between 12% and less than 0.5% with the larger error being at the smallest cross  
 1176 section values where  $F_2^{(\pi p)}(x, \Delta|\mathbf{k}|, \Delta\theta_{p'})$  dramatically turns down in  $x$ . The data will be  
 1177 binned in both  $x$  and proton momentum bins.

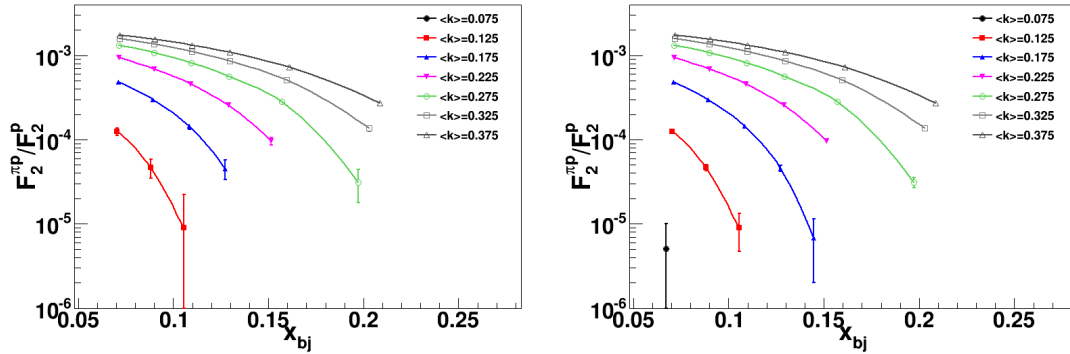


Figure 35:  $x$  dependence of the ratio of the semi-inclusive structure function  $F_2^{(\pi p)}(x, \Delta|\mathbf{k}|, \Delta\theta_{p'})$  to the inclusive nucleon structure function  $F_2^p$  for the neutron (left) and proton (right). The solid curves follow from varying the integration range of  $\Delta|\mathbf{k}|$ , they correspond to;  $\Delta|\mathbf{k}| = [60, 100]$  MeV (black),  $\Delta|\mathbf{k}| = [100, 150]$  MeV (red),  $\Delta|\mathbf{k}| = [150, 200]$  MeV (blue),  $\Delta|\mathbf{k}| = [200, 250]$  MeV (magenta),  $\Delta|\mathbf{k}| = [250, 300]$  MeV (green),  $\Delta|\mathbf{k}| = [300, 350]$  MeV (light grey), and  $\Delta|\mathbf{k}| = [350, 400]$  MeV (grey). The points are projections for this experiment.

1178 Using the momentum bins of Fig. 35, Fig. 36 depicts the potential reach in  $t$  of  
 1179  $F_2^{(\pi p)}(t, \Delta x)$  towards the pion pole for a number of different  $x$  bins. Here, the low mo-  
 1180 mentum reach of the RTPC detector is critical to define the downward-turning shape of  
 1181 the curve.

1182 Fig. 37 is similar to Fig. 6, presenting the same structure function quantities for  
 1183 the neutron as were just shown for the proton, but with a comparison instead to the  
 1184 strength of other physics channels, the tagged structure functions for  $(\pi^- p)$ ,  $(\rho^- p)$ , and  
 1185  $(\pi^0 \Delta^0 + \pi^- \Delta^+)$ , rather than to the measured momentum range components. The statisti-  
 1186 cal uncertainty on the projected data is included, and ranges between 0.4 and 1.3%, with  
 1187 the larger error being at the smaller cross section, larger  $x$  values. Here, a momentum  
 1188 range from 250 – 400 MeV only is shown rather than the full requested range down to  
 1189 150 MeV/c. It is not anticipated that we will measure below 150 MeV/c, due to the  
 1190 increased background constraints. The expected statistical uncertainty for the deuterium  
 1191 measurement in the momentum bin  $150 < k < 200$  MeV/c is 15%, moving to nearly  
 1192  $\sim 1\%$  in the highest momentum bin. As with the hydrogen data, multiple bins in both  
 1193 momentum and  $x$  will be obtained.

1194 The proposed experiment will provide access to the pion structure function via the  
 1195 Sullivan process, where the coincidence of the DIS-scattered electron and the low momen-

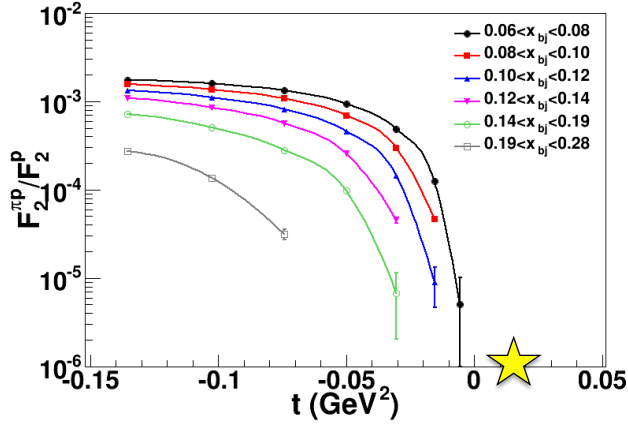


Figure 36:  $t$  dependence of the ratio of  $F_2^{(\pi p)}(t, \Delta x)$  to  $F_2^p$  for momentum between 150 and 400 MeV/c, for a varying ranges in  $x$ , they correspond to  $0.06 < x < 0.08$  (black),  $0.08 < x < 0.10$  (red),  $0.10 < x < 0.12$  (blue),  $0.12 < x < 0.14$  (magenta),  $0.14 < x < 0.19$  (green) and  $0.19 < x < 0.28$  (grey). The points are projected data from this proposal with the statistical error bars included, but difficult to see on the log scale. The yellow star shows the location of the pion pole.

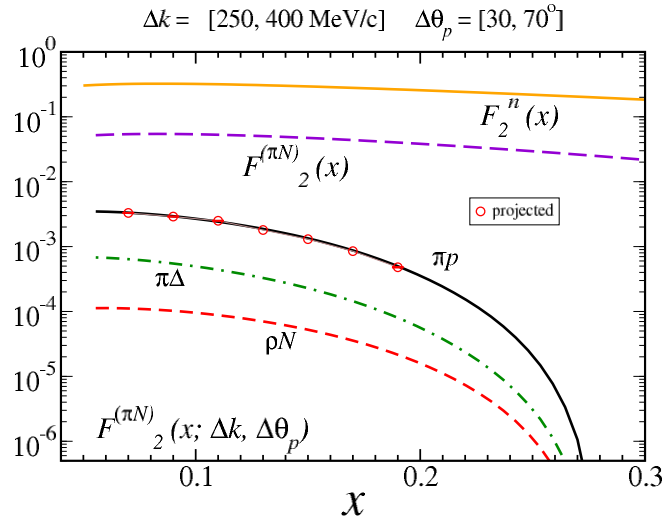


Figure 37: Structure functions as in Fig. 6 for the neutron-tagged target, with the  $x$  dependence of  $F_2^{(\pi p)}(x, \Delta|\mathbf{k}|, \Delta\theta_p)$  for charge-exchange in, e.g., the  $n \rightarrow \pi^- p$  process. The tagged semi-inclusive structure function for  $(\pi^- p)$  (black, solid),  $(\rho^- p)$  (red, dashed), and  $(\pi^0 \Delta^0 + \pi^- \Delta^+)$  (green, dot-dashed) are compared with the inclusive structure function of the neutron  $F_{2n}(x)$  (orange), and the fully-integrated  $(\pi^- p)$  contribution  $F_2^{\pi N}(x)$  (violet, dashed). Projected data are shown, with statistical error bars included.

1196 tum recoil proton will tag a pion target event. Experimental knowledge of the partonic  
1197 structure of the pion is currently very limited due to the lack of a pion target, and most

1198 of the current knowledge of the pion structure function in the valence region is obtained  
 1199 primarily from pionic Drell-Yan scattering [23]-[25].

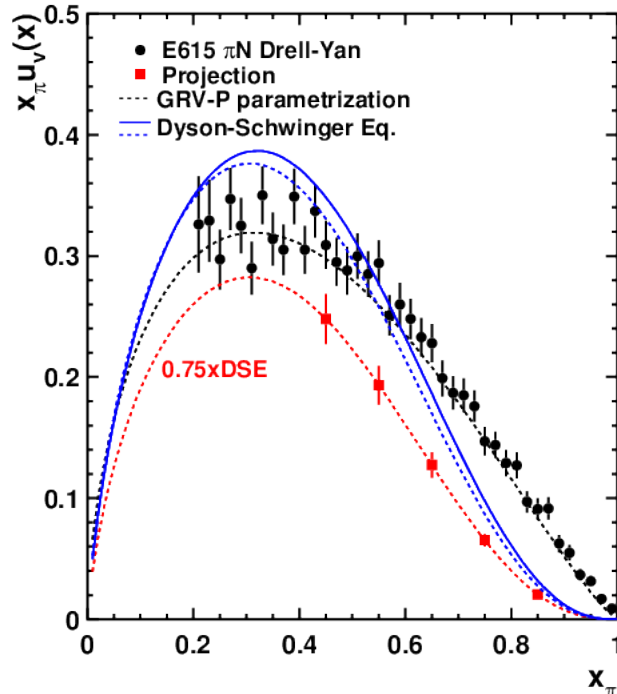


Figure 38: Projected pion structure function results. Also shown are the results from the pionic Drell-Yan experiment E615, the GRV-P parametrization and a Dyson-Schwinger equation based calculation from Ref. [26]. The projected points are shown along a curve which is  $0.75 \times \text{DSE}$ , in order to demonstrate the potential for shape discrimination.

1200 Fig 38 shows the projected pion structure function that can be extracted from this  
 1201 experiment. A 5% systematic uncertainty in the pion flux is assumed (to be achieved by  
 1202 comparing to pionic Drell-Yan data at  $x_\pi = 0.5$ ), and a total systematic uncertainty of  
 1203 8.4% is used. The projected results are shown along with the existing pionic Drell-Yan  
 1204 data from E615 and the GRV-p parametrization of the pion structure function, and a  
 1205 calculation based on the Dyson-Schwinger equation [26]. There are several theoretical  
 1206 calculations of the pion structure in the valence region, however they tend to disagree  
 1207 with each other – underscoring that it is essential to measure the pion structure function  
 1208 over a wide range of  $x$ .

1209 As can be seen in Fig. 38, the proposed data nicely complement the Drell-Yan data  
 1210 and will fill in the heretofore unprobed moderate  $x$  range. Moreover and importantly,  
 1211 measurements of pion parton distributions using the Drell-Yan process are limited to  
 1212 charged pions, while the proposed experiment will also include the neutral pion and  
 1213 provide a check of the validity of isospin symmetry and any dynamical effects that differ  
 1214 between neutral and charged pions.

### 1215 3.1 Beam Time Request

1216 We propose to measure the semi-inclusive reactions  $p(e, e'p)X$  and  $D(e, e'pp)X$  using a  
 1217  $50\mu\text{A}$  beam on a 1 atm, cooled straw, gaseous hydrogen target with radius of 5 mm and  
 1218 length of 40 cm, for a total luminosity of  $3 \times 10^{36} \text{ cm}^{-2}\text{s}^{-1}$ . The well-known DIS cross  
 1219 section was used as the initial basis for calculation [67], in conjunction with the rate due  
 1220 to the pionic contribution (from the calculations presented in Sec. 1.1) is given by:

$$1221 \text{Rate}(\text{DIS}_{\pi N}) = \text{Rate}(\text{DIS}) \times (F2_{\pi N}/F2_n).$$

1222 The Tagged-DIS rate on hydrogen is given by:

$$1223 \text{Rate}(\text{TDIS}_{\pi N}) = \text{Rate}(\text{DIS}) \times \text{eff}_{\text{RTPC}} \times \text{eff}_{\text{SBS}},$$

1224 using a conservative combined RTPC efficiency and acceptance of 40% and SBS efficiency  
 1225 of 90%. The  $x$  range  $0.06 < x < 0.2$  will be divided into 5 bins and, for *each* bin in  $x$ ,  
 1226 the recoil proton momentum  $k$  will be divided into at least another 6 bins. The requested  
 1227 beam time is estimated with the goal of better than 1% statistical uncertainty on average  
 1228 for the recoil momentum  $k$  bins within each  $x$  bin. The worst case scenario is the lowest  
 1229 rate, highest  $x$  bin, where we estimate that 10 days of beam time is needed to obtain  
 1230 adequate statistical precision. Due to the large acceptance of the SBS and RTPC, all of  
 1231 the other remaining data displayed and projected will be obtained *simultaneously* with  
 1232 this bin and so require no additional beam time request.

1233 Table 6 shows the estimated electron cross section within the SBS acceptance, the  
 1234  $F2_{\pi N}/F2_n$ , the projected TDIS rate, and the yield in each  $x$  bin for 10 days of beam on  
 1235 a hydrogen target. Table 6 also shows the yield in each  $x$  bin for 10 days of beam on a  
 1236 deuterium target. The expected statistical uncertainty for the deuterium measurement in  
 1237 the momentum bin  $150 < k < 200 \text{ MeV}/c$  is 15%, moving to nearly  $\sim 1\%$  in the highest  
 1238 momentum bin. The requirement of two low momentum protons detected in vertex and  
 1239 time coincidence (one backward and one more forward) requires double-accounting for the  
 1240 RTPC efficiency when using the deuterium target – which is very conservatively estimated  
 1241 here. Each kinematic  $E', \theta, \phi$  bin must pass cuts on the SBS acceptance, and an electron  
 1242 trigger energy  $< 6 \text{ GeV}$ , and threshold  $> 1 \text{ GeV}$  are required. There are also kinematic  
 1243 cuts employed to ensure  $W > 2$  and  $Q^2 > 1 \text{ GeV}^2$ .

1244 Table 7 shows the estimated statistical uncertainty,  $\delta\sigma/\sigma$  in percent, for the proton  
 1245 momentum bins ( $\Delta k$ , top) to be measured *within an  $x$  bin* around  $0.1 \pm 0.01$  for the  
 1246 hydrogen target, as an example for the momentum range and breadth of data expected  
 1247 within *each* of the  $x$  bins in Table 6. The range of momentum bins will directly pro-  
 1248 vide a corresponding range of  $t$  bins for each  $x$ . Here, the electron and proton yields,  
 1249  $N_{e,e'}$  and  $N_{e,e'p}^{\text{good}}$ , are subject to the same cuts and efficiency assumptions as in Table 6,  
 1250 above. The electron yields,  $N_{e,e'}$ , are based on well known DIS cross section [67], the  
 1251 yields for the protons of interest is estimated as  $N_{e,e'p}^{\text{good}} = N_{e,e'} \times (F2_{\pi N}^p/F2_n^p)$ , the accidental  
 1252 proton yields  $N_{e,e'p}^{\text{acc}}$ , are based on the background simulation described in Sec. 2.5 and are  
 1253 estimated as described in Sec. 2.2.1. Finally the statistical uncertainty is estimated as  
 1254  $\delta\sigma = \sqrt{N_{e,e'p}^{\text{good}} \times (1 + B/S)}$ , where  $S/B$  is the signal to background ratio.

1255 In addition to 10 days of 11 GeV beam on hydrogen and 10 days on deuterium, we  
 1256 request also 5 days on a hydrogen target at a reduced luminosity in order to validate  
 1257 the background subtraction procedure. It will be necessary to commission the RTPC,  
 1258 the new SBS electron detection system, as well as to verify the vertex and reconstruction

x range	$\sigma_e$ in SBS (nb)	$F_2^{\pi N}/F_2$ ( $\times 10^{-5}$ )	TDIS $\pi N$ Rate (Hz)	Yield H <sub>2</sub> 10 days (k)	Yield D <sub>2</sub> 10 days (k)
0.06 - 0.2	1.84	116	2.31	1993	798
0.06 - 0.08	0.22	336	0.80	688	276
0.08 - 0.10	0.29	230	0.71	614	246
0.10 - 0.12	0.30	137	0.45	390	156
0.12 - 0.14	0.29	69	0.21	184	74
0.14 - 0.19	0.67	13	0.10	83	34

Table 6: Rates and expected yields for this experiment in the proposed  $x$  bins. All of the data will be obtained simultaneously for each target within the acceptance(s) of the SBS and RTPC without changing settings. Multiple proton momentum bins will be obtained within each  $x$  bin, as shown in the example below.

$\Delta k$ (MeV/c)	150-200	200-250	250-300	300-350	350-400
$\Delta T$ (MeV)	9	12	15	17	20
$N_{e,e'} (\times 10^6)$	710	710	710	710	710
$N_{e,e'p}^{good} (\times 10^3)$	59	159	267	354	413
$N_{e,e'p}^{acc} (\times 10^3)$	380	510	640	724	852
S/B	1/6.4	1/3.2	1/2.4	1/2	1/2
$\delta\sigma/\sigma$ (%)	1.1	0.5	0.4	0.3	0.3

Table 7: Statistical uncertainty for this experiment in an example  $x$  bin around  $0.1 \pm 0.01$  for the hydrogen target. It is planned that each proposed  $x$  bin will be broken down into such  $k$  bins, and that all of the data will be obtained simultaneously for each target within the acceptance(s) of the SBS and RTPC.

1259 optics. We request 2 beam days (mixed evenly between the the hydrogen and deuterium  
1260 targets), also at 11 GeV, for these requisite preparations. We note that the collaboration  
1261 anticipates some advance detector pre-commissioning of the RTPC and SBS detectors  
1262 using radioactive sources, cosmic rays, and possibly the low energy proton beam at TUNL  
1263 as was done in advance for BONUS. Lastly, two shifts of beam time at 4.4 GeV will  
1264 be required for measuring the RTPC acceptance and efficiency using elastic neutrons  
1265 measured in HCAL, as described above. The two shifts are planned to take place one  
1266 at the start of the deuterium running and one at the end to track any time-dependent  
1267 systematic effects. This will require two half-shift beam energy changes, where target  
1268 gas changes will take place concurrently. The total beam time request of 27 days is  
1269 summarized in Table 8.

Target	Current ( $\mu\text{A}$ )	Beam Energy (GeV)	Beam Time (hrs)	Notes
Hydrogen	50	11	240	includes 1 day for commissioning
Deuterium	25	11	240	
Hydrogen	5	11	120	RTPC calibration with HCAL Beam Energy Changes
Deuterium	5	4.4	48	
			8	
Total			656	27 days

Table 8: Summary of beam time request.

## 3.2 Expected Experimental Accuracy

1270 **3.2 Expected Experimental Accuracy**  
 1271 An overall systematic uncertainty of 5% in the cross section measurements is assumed  
 1272 for this experiment, building on the CLAS-6 BONUS and eg6 experience utilizing the  
 1273 RTPC [68]. We believe this to be highly reasonable for the following reasons. First,  
 1274 CLAS-6 had a large ( $> 5\%$ ) uncertainty associated with the  $E, \theta$  dependent CLAS trigger  
 1275 efficiency. The SBS is a far simpler device, and is expected to have a very small trigger  
 1276 efficiency uncertainty and only a 3% overall systematic uncertainty. In BONUS, moreover,  
 1277 4.2% of the 8.7% overall systematic uncertainty came from the inclusive  $F_2^d/F_2^p$  model  
 1278 dependence in the ratio measurement performed – largely in the resonance region. We  
 1279 are here proposing a cross section measurement, with no ratio normalization technique  
 1280 to be employed. SBS inclusive results can be verified against the well-known proton  
 1281 DIS cross section. Moreover, the better spatial resolution of the proposed GEM readout,  
 1282 combined with the increased drift distance, will improve tracking and vertex resolution  
 1283 in the RTPC as compared to BONUS. We also propose not only to use a Monte Carlo  
 1284 for the RTPC acceptance and efficiency, but to carefully measure it using the HCAL  
 1285 elastic neutron technique described above. We have analyzed the background which is  
 1286 due to real coincidence between the DIS electron and secondary mesons misidentified as  
 1287 protons. As mentioned earlier, the uncertainty on the pion contribution to the electron  
 1288 sample is expected to be on the level of 1% or less. Secondary mesons misidentified as  
 1289 protons can be determined with a 10% uncertainty, which implies a 1% uncertainty in  
 1290 the true coincidence counts. The anticipated impact on the systematic uncertainty due to  
 1291 backgrounds is expected to be small due to several available methods which are proposed  
 1292 to evaluate them. For example, a coincidence time cut and a vertex ( $\delta z$ ) cut will be used.  
 1293 Low luminosity data taking ( 5 PAC days requested for these studies) will also be used  
 1294 to verify the simulations and calculations from the higher rate data. This is included in  
 1295 the systematic uncertainty table below (Table 9).

## 4 Summary

1296 **4 Summary**  
 1297 We propose a pioneering measurement technique for probing the elusive mesonic content  
 1298 of the nucleon structure function. The technique involves detecting a low-momentum

Source	Uncertainty
Accidental background subtraction	5%
DIS electron cross section (Targ. density, beam charge, acceptance, det. efficiency)	3%
RTPC absolute efficiency	2%
RTPC deadtime	1%
RTPC momentum resolution	< 1%
RTPC angular acceptance	1%
Beam position	< 1%
Total	6.5 %

Table 9: Table to systematic uncertainties

1299 recoil proton (pair of protons) in coincidence with a deeply inelastically scattered elec-  
1300 tron from a hydrogen (deuterium) target. By tagging events from bound objects in the  
1301 target, this technique provides a probe of the meson cloud component in the nucleon,  
1302 and thereby access to the meson structure function. Additionally, this experiment will  
1303 measure for the first time the tagged DIS cross section for proton and neutron targets in  
1304 the target fragmentation region. The measurement will be performed in the  $Q^2$  range of  
1305 0.5 to 6  $(\text{GeV}/c)^2$  at very low proton momenta in the range of  $(60 - 400)$  MeV/c. The  
1306 experiment will use the Super Bigbite Spectrometer to detect the scattered electrons and  
1307 a low mass radial time projection chamber (RTPC, a BONUS-like detector) to detect the  
1308 low momentum proton(s) in time and vertex coincidence with a DIS electron. In this  
1309 experiment a  $50\mu$  A, 11 GeV beam will be incident on a 5 mm radius, 40 mm long straw  
1310 tube target with 1 atm cool hydrogen (deuterium) gas. We request a total of 22 days  
1311 of beam time, with 10 days of production  $50 \mu\text{A}$  beam on the hydrogen target, 5 days  
1312 production on the deuterium target, 2 days for optics and detector commissioning, and  
1313 an additional 5 days of  $5 \mu$  A beam on the hydrogen target for background checks.

# A A Phenomenological Model of Tagged Deep Inelastic Scattering

We review the predictions of pion cloud models for contributions to the structure functions of the nucleon, firstly for the inclusive DIS case, and then to the "tagged" semi-inclusive cross sections, which we study as a function of several kinematic variables [46, 47, 48].

## A.0.1 Meson Cloud Contributions to Inclusive DIS

As pointed out by Sullivan [3], the contribution to the inclusive  $F_2$  structure function of the nucleon from scattering off a virtual pion emitted from the nucleon can be written as

$$F_2^{(\pi N)}(x) = \int_x^1 dz f_{\pi N}(z) F_{2\pi}\left(\frac{x}{z}\right), \quad (12)$$

where  $z = k^+/p^+$  is the light-cone momentum fraction of the initial nucleon carried by the interacting pion. In the infinite momentum frame this coincides with the longitudinal momentum fraction, while in the rest frame of the target nucleon, which we will use in the following,  $z$  is expressed as  $z = (k_0 + |\mathbf{k}| \cos \theta)/M$ , where  $M$  is the mass of the nucleon,  $k_0 = M - \sqrt{M^2 + \mathbf{k}^2}$  is the pion energy, and  $\theta$  is the angle between the vector  $\mathbf{k}$  and the  $z$ -axis (which is equal to the angle between the recoil proton momentum  $\mathbf{p}'$  and the photon direction). For ease of notation, we also suppress the explicit dependence of the structure functions on the scale  $Q^2$ .

The function  $f_{\pi N}(z)$  gives the light-cone momentum distribution of pions in the nucleon,

$$f_{\pi N}(z) = c_I \frac{g_{\pi NN}^2}{16\pi^2} \int_0^\infty \frac{dk_\perp^2}{(1-z)z} \frac{G_{\pi N}^2}{(M^2 - s_{\pi N})^2} \left( \frac{k_\perp^2 + z^2 M^2}{1-z} \right), \quad (13)$$

where  $k_\perp$  is the transverse momentum of the pion,  $g_{\pi NN}$  is the  $\pi NN$  coupling constant, and the isospin factor  $c_I = 1$  for  $\pi^0$  ( $p \rightarrow p\pi^0$  or  $n \rightarrow n\pi^0$ ) and  $c_I = 2$  for  $\pi^\pm$  ( $p \rightarrow n\pi^+$  or  $n \rightarrow p\pi^-$ ). The function  $G_{\pi N}$  parametrizes the momentum dependence of the  $\pi NN$  vertex function, which, due to the finite size of the nucleon, suppresses contributions from large- $|\mathbf{k}|$  configurations. Similar expressions (though somewhat more involved) can be written for other contributions, such as from  $\rho$  mesons or with  $\Delta$  baryons in an intermediate state. However, because of the small mass of the pion, the  $\pi N$  configuration is expected to be the dominant one. In Eq. (13) the variable  $s_{\pi N} = (k_\perp^2 + m_\pi^2)/z + (k_\perp^2 + M^2)/(1-z)$  represents the total squared center of mass energy of the intermediate  $\pi N$  system, and is related to the pion virtuality  $t$  by  $t - m_\pi^2 = z(M^2 - s_{\pi N})$ .

The form factor  $G_{\pi N}$  (or more generally  $G_{MN}$  for a meson  $M$ ) can be constrained by comparing the meson cloud contributions with data on inclusive  $pp \rightarrow nX$  scattering, as performed by Holtmann *et al.* [47]. For the purpose of this proposal, we use the parametric form

$$G_{\pi N} = \exp \left[ (M^2 - s_{\pi N})/\Lambda^2 \right], \quad (14)$$

where  $\Lambda$  is the form factor cutoff parameter. (Note that in Ref. [47] a parametrization of the form  $\exp[(M^2 - s_{\pi N})/2\Lambda^2]$  is used, so that the corresponding cutoffs there are smaller by a factor of  $\sqrt{2}$ .) An illustration of the typical spectra for the differential cross section

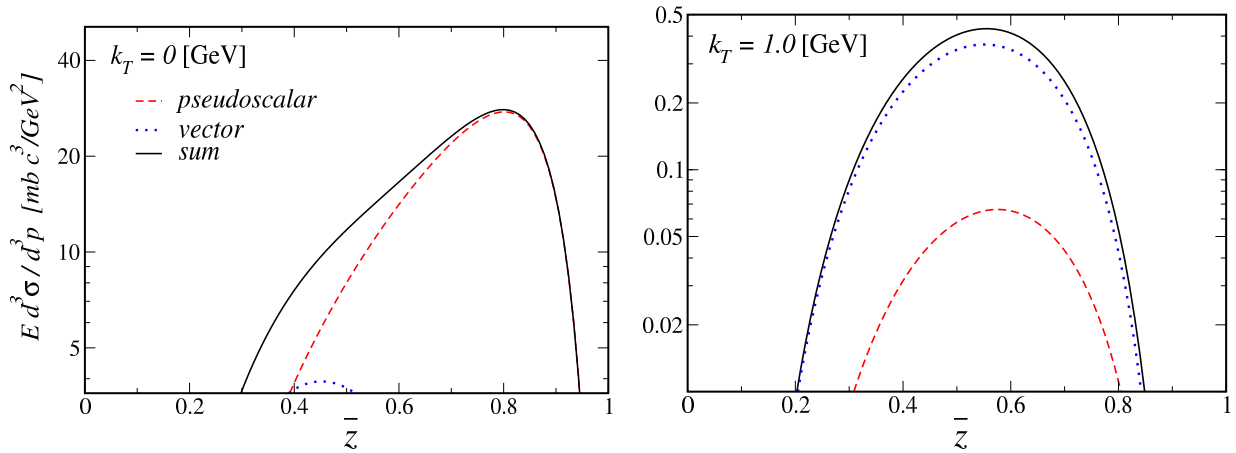


Figure 39: Typical spectra for the differential cross section  $E d^3 \sigma / d^3 p'$  in the  $pp \rightarrow nX$  reaction for transverse momentum  $k_{\perp} = 0$  (left panel) and  $k_{\perp} = 1$  GeV (right panel), as a function of the light-cone momentum fraction  $\bar{z} \equiv 1 - z$ . The pseudoscalar  $\pi$  (red dashed lines) and vector  $\rho$  (blue dotted lines) contributions, and their sum (black solid lines), are indicated explicitly.

1349  $E d^3 \sigma / d^3 p'$  in the  $pp \rightarrow nX$  reaction arising from  $\pi$  and  $\rho$  exchange is shown in Fig. 39 as  
 1350 a function of the light-cone momentum fraction  $\bar{z} \equiv 1 - z$  carried by the final nucleon,  
 1351 for two values of the transverse momentum  $k_{\perp}$ . For small  $k_{\perp}$  the  $\pi$  exchange contribution  
 1352 clearly dominates the  $\rho$  at all  $\bar{z}$ , while at larger momenta the contributions from heavier  
 1353 mesons such as the  $\rho$  become more important.

1354 Using the cutoff parameters constrained by the inclusive hadronic  $pp \rightarrow nX$  data,  
 1355 which were found in Ref. [47] to be  $\Lambda_{\pi N} = \Lambda_{\rho N} = 1.56 \pm 0.07$  GeV and  $\Lambda_{\pi \Delta} = \Lambda_{\rho \Delta} =$   
 1356  $1.39 \pm 0.07$  GeV, the light-cone momentum distributions  $f(z)$  are shown in Fig. 40. The  
 1357 principal model uncertainty in these results comes from the ultraviolet regulator  $G$  used  
 1358 to truncate the  $k_{\perp}$  integrations in the distribution functions. Various functional forms  
 1359 have been advocated in the literature aside from the  $s$ -dependent exponential form factor  
 1360 in Eq. (14), and we compare several of these, including  $s$ - and  $t$ -dependent dipole forms,  
 1361 in Fig. 41. For the  $s$ - and  $t$ -dependent forms in particular, the differences are noticeable  
 1362 mostly at small values of  $z$ , where the  $t$ -dependent parametrization (of the form  $G \sim$   
 1363  $1/(t - \Lambda^2)^2$ ) tends to give somewhat larger distributions that are peaked at smaller  $z$ ,  
 1364 compared with the  $s$ -dependent form, which tend to be broader.

1365 Convoluting the light-cone distributions with the structure function of the meson as  
 1366 in Eq. (12), the resulting contributions from the  $\pi N$  and  $\rho N$  intermediate states to the  
 1367 inclusive  $F_2$  structure function of the proton is illustrated in Fig. 42. For the meson  
 1368 structure function we use the parametrization from GRV, and assume that  $F_{2\pi}(x) \approx$   
 1369  $F_{2\rho}(x)$ . The results are plotted for fixed values of the scattering angle of the final state  
 1370 electron  $\theta_e$ , which determines the  $Q^2$  dependence of the contribution at a given  $x$ . For  
 1371 angles between  $\theta_e = 15^\circ$  and  $40^\circ$  the  $Q^2$  dependence is rather negligible due to the  
 1372 mild  $Q^2$  dependence of the meson structure function. For the fully integrated results  
 1373 of Fig. 42, the model uncertainties are greatest for the lowest accessible values to the  
 1374 proposed experiment of  $x \sim 0.05$ .

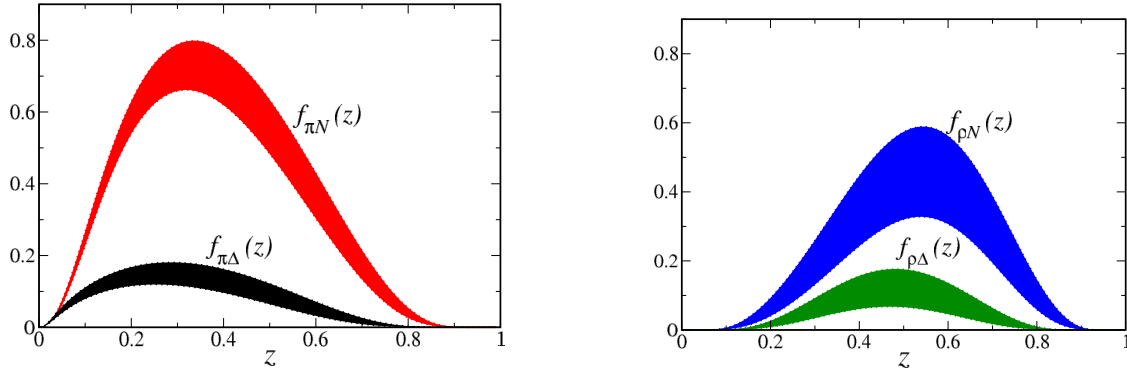


Figure 40: Light-cone momentum distributions of the pion,  $f_{\pi N}$  and  $f_{\pi\Delta}$  (left panel) and the  $\rho$  meson,  $f_{\rho N}$  and  $f_{\rho\Delta}$  (right panel), as a function of the meson light-cone momentum fraction  $z$ . The error bands correspond to the cutoff parameter ranges as given in the text.

### 1375 A.0.2 Tagged Structure Functions

1376 While the inclusive reactions require integration of the pion momentum over all possible  
 1377 values, detecting the recoil proton in the final state allows one to dissect the internal  
 1378 structure with significantly more detail and increase the sensitivity to the dynamics of  
 1379 the meson exchange reaction. In general, we will be interested in the relative contributions  
 1380 of the semi-inclusive reaction with respect to the inclusive process. In practice, the semi-  
 1381 inclusive structure function will be given by the unintegrated product

$$F_2^{(\pi N)}(x, z, k_\perp) = f_{\pi N}(z, k_\perp) F_{2\pi}\left(\frac{x}{z}\right), \quad (15)$$

1382 where the unintegrated distribution function  $f_{\pi N}(z, k_\perp)$  is defined by

$$f_{\pi N}(z) = \frac{1}{M^2} \int_0^\infty dk_\perp^2 f_{\pi N}(z, k_\perp^2). \quad (16)$$

1383 The dependence of the tagged structure functions on the kinematical variables that are  
 1384 measured experimentally can be studied by relating the magnitude of the 3-momentum  
 1385  $\mathbf{k}$  of the exchanged pion in the target rest frame to the pion's transverse momentum  $k_\perp$   
 1386 and light-cone fraction  $z$ ,

$$\mathbf{k}^2 = k_\perp^2 + \frac{[k_\perp^2 + (1 - [1 - z]^2)M^2]^2}{4M^2(1 - z)^2}. \quad (17)$$

1387 Experimentally, the quantities most readily measured are the momentum of the produced  
 1388 proton,  $\mathbf{p}'$ , which in the rest frame is  $\mathbf{p}' = -\mathbf{k}$ , and the scattering angle  $\theta_{p'} = \theta$  of the  
 1389 proton with respect to the virtual photon direction. In the limit  $k_\perp^2 = 0$ , the magnitude  
 1390 of  $\mathbf{k}$  becomes

$$|\mathbf{k}|_{k_\perp^2=0} = \frac{zM}{2} \left( \frac{2 - z}{1 - z} \right), \quad (18)$$

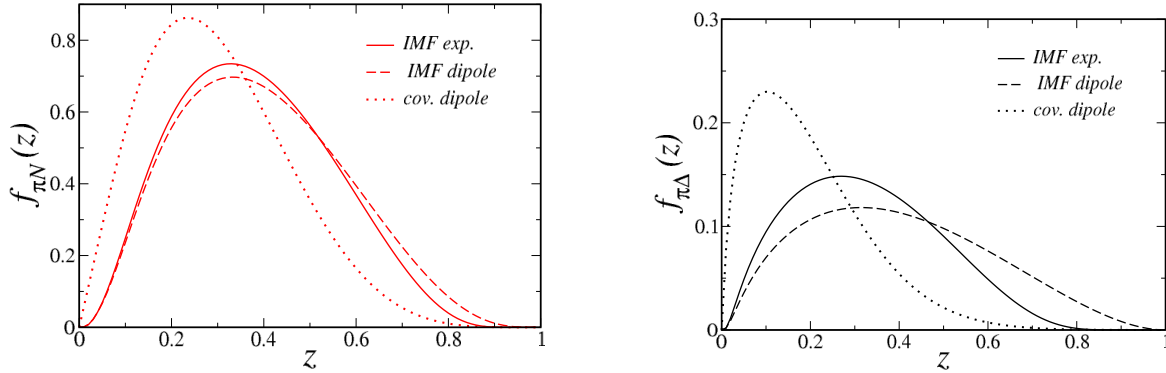


Figure 41: Light-cone momentum distributions for the  $\pi N$  (left panel) and  $\pi \Delta$  (right panel) intermediate states, for several different functional forms of the form factor  $G$  in Eq. (13): “IMF” refers to  $s$ -dependent forms such as in Eq. (14), while “cov” denotes a form factor that depends only on the variable  $t$ .

1391 which imposes the restriction  $z \lesssim |\mathbf{k}|/M$ . This relation is illustrated in Fig. 43 for values  
 1392 of  $z$  up to 0.2.

1393 This is a critical guiding parameter for the proposed experiment. Since we seek to mea-  
 1394 sure the low momentum region where pseudo scalar production dominates, the region of  
 1395 interest becomes  $z \lesssim 0.2$ . This corresponds to the measurable proton range,  $60 \lesssim \mathbf{k} \lesssim 400$   
 1396 MeV/c, of the radial time projection chamber discussed in detail below. It is important  
 1397 to note that, since  $x < z$ , this also determines both the  $x$  and  $Q^2$  (given the maximum  
 1398 beam energy) of the experiment.

1399 The kinematic restrictions on  $|\mathbf{k}|$  for a given  $z$  can also be illustrated by considering  
 1400 the unintegrated light-cone distribution functions as a function of the variable  $t$ . This is  
 1401 relevant since one way of identifying the pion exchange mechanism is through its charac-  
 1402 teristic  $t$  dependence, which is pronounced near the pion pole at  $t = +m_\pi^2$ . The production  
 1403 of a physical proton (or  $\Delta$  baryon) in the final state restricts the maximum value of  $t$ ,  
 1404 however (corresponding to the minimum transverse momentum,  $k_\perp = 0$ ), to

$$t_{\min}^N = -\frac{M^2 z^2}{1-z}, \quad t_{\min}^\Delta = -\frac{(M_\Delta^2 - (1-z)M^2)z}{1-z}, \quad (19)$$

1405 for nucleon  $N$  and  $\Delta$  final states, respectively. Implementing these limits, the  $t$ -dependence  
 1406 of the distributions for  $\pi$  exchange with a nucleon or  $\Delta$  recoil is illustrated in Fig. 44.  
 1407 Note that at the larger  $z$  value there is a considerable gap between the values of  $t$  at which  
 1408  $\Delta$  production is possible compared with  $N$  production.

1409 Experimentally, the semi-inclusive cross sections will be measured in specific bins of  
 1410 recoil proton momentum  $|\mathbf{p}'| = |\mathbf{k}|$  and scattering angle  $\theta_{p'}$  (or equivalently  $z$  and  $k_\perp$ ). We  
 1411 therefore define the partially integrated semi-inclusive structure function  $F_2^{(\pi N)}(x, \Delta z, \Delta k_\perp^2)$ ,

$$F_2^{(\pi N)}(x, \Delta z, \Delta k_\perp^2) = \frac{1}{M^2} \int_{\Delta z} \int_{\Delta k_\perp^2} f_{\pi N}(z, k_\perp) F_{2\pi}\left(\frac{x}{z}\right), \quad (20)$$

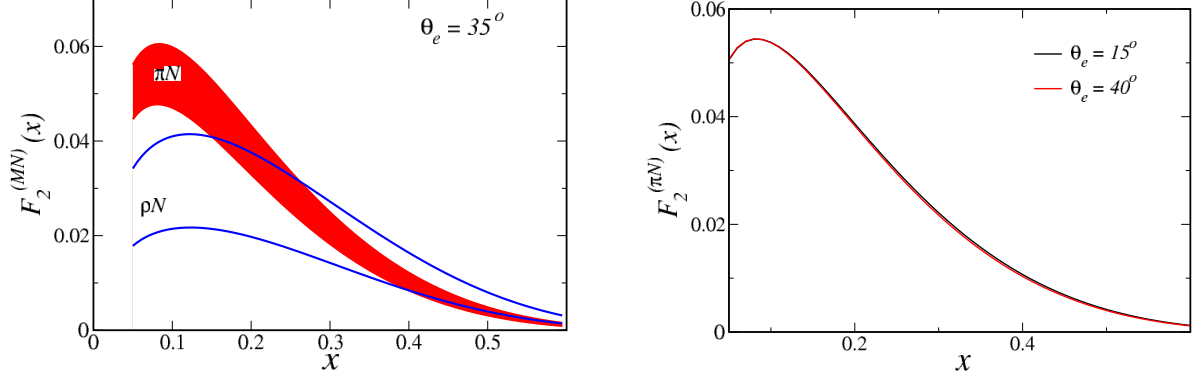


Figure 42: Contributions from  $\pi N$  and  $\rho N$  intermediate states to the inclusive  $F_2$  structure function of the proton for fixed electron scattering angle  $\theta_e = 35^\circ$  (left panel), and at two different angles,  $\theta_e = 15^\circ$  and  $40^\circ$  (right panel) for the  $\pi N$  contributions.

1412 integrated over the range  $\Delta z = [z_{\min}, z_{\max}]$  and  $\Delta k_{\perp}^2 = [k_{\perp \min}^2, k_{\perp \max}^2]$ . Alternatively, one  
 1413 can define an analogous semi-inclusive structure function integrated over other variables,  
 1414 such as  $|\mathbf{k}|$  and  $\theta_{p'}$ , by  $F_2^{(\pi N)}(x, \Delta|\mathbf{k}|, \Delta\theta_{p'})$ . The proposed experiment will probe the  
 1415 ranges of kinematics  $0.05 \lesssim z \lesssim 0.2$  and  $60 \lesssim |\mathbf{k}| \lesssim 400$  MeV, and angles  $30 \lesssim \theta_{p'} \lesssim 160^\circ$ ,  
 1416 with  $x$  in the vicinity of  $x \sim 0.05 - 0.2$ .

1417 Fig. 45 shows the semi-inclusive structure functions  $F_2^{(MN)}(|\mathbf{k}|; \Delta x, \Delta\theta_{p'})$  for  $p \rightarrow \pi^0 p$   
 1418 and  $p \rightarrow \rho^0 p$ , as a function of the momentum  $|\mathbf{k}|$ , integrated over  $x$  between 0 and 0.6,  
 1419 and over all angles  $\theta_{p'}$  from 0 to  $\pi$ . The structure functions rise with increasing  $|\mathbf{k}|$  in  
 1420 the experimentally accessible region  $|\mathbf{k}| \lesssim 0.5$  GeV, where The  $\rho$  contribution is clearly  
 1421 suppressed relative to the pion contribution. At larger momenta the effects of the meson–  
 1422 nucleon form factors become more important, which suppress the contributions from  
 1423 high- $|\mathbf{k}|$  tails of the distributions. The peak in the  $\pi$  distribution occurs at  $|\mathbf{k}| \approx 0.6$  GeV,  
 1424 while the  $\rho$  distribution peaks at higher momenta,  $|\mathbf{k}| \approx 1.2$  GeV, and has a slower fall-off  
 1425 with  $|\mathbf{k}|$ .

1426 To further illustrate the capability for an experiment at the proposed kinematics to  
 1427 minimize effects from the  $p \rightarrow \rho p$  process, Fig. 46 gives the  $x$  dependence of the semi-  
 1428 inclusive structure function  $F_2^{(MN)}(x, \Delta|\mathbf{k}|, \Delta\theta_{p'})$  for  $p \rightarrow \pi^0 p$  and  $p \rightarrow \rho^0 p$ , integrated  
 1429 over the momentum range of this experiment for all angles  $\theta_{p'}$ . The  $\rho$  channel is nearly  
 1430 two orders of magnitude smaller.

1431 The angular dependence of  $F_2^{(MN)}$  as shown in Fig. 47 again shows the dominance  
 1432 of the  $\pi$  over the  $\rho$ . The angular dependence will, moreover, prove to be important to  
 1433 removing the experimental background arising from low energy  $e-p$  scattering. Elastically  
 1434 scattered protons in a comparable energy range to the TDIS recoil protons are essentially  
 1435 confined around  $90^\circ$ , allowing for a separation between these and the TDIS recoil protons  
 1436 of interest.

1437 The effect of the pion–nucleon form factors was studied, and found to be relatively mild  
 1438 in this momentum interval. It is only for larger momenta ( $|\mathbf{k}| \gtrsim 0.5$  GeV) that the form

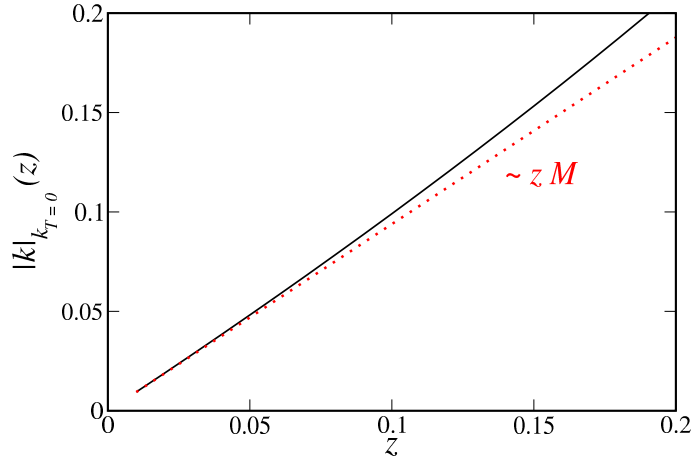


Figure 43: Pion momentum  $|\mathbf{k}|$  as a function of the light-cone fraction  $z$  for  $k_{\perp} = 0$  (black solid). The linear approximation  $\sim zM$  (red dotted) is shown for comparison.

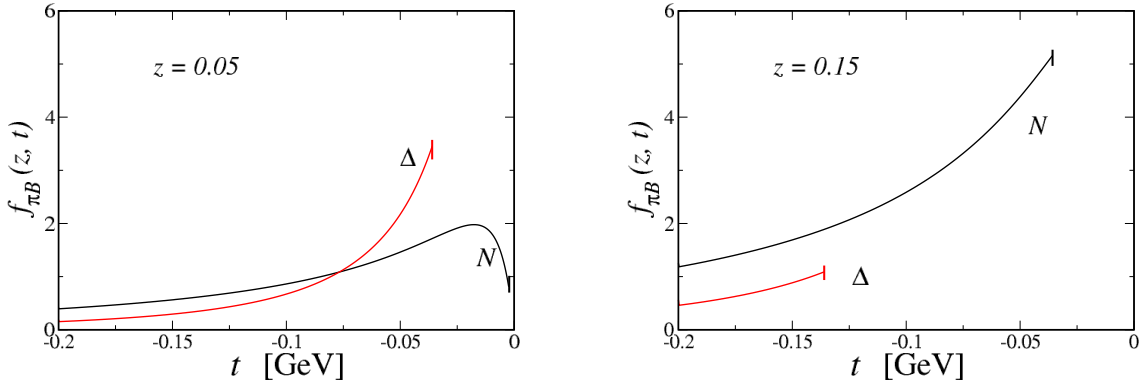


Figure 44: Unintegrated light-cone distribution functions for  $\pi N$  (black solid) and  $\pi\Delta$  (red solid) states as a function of  $t$ , for fixed values of  $z = 0.05$  (left) and  $z = 0.15$  (right).

1439 factor model becomes significant. The dependence of the semi-inclusive structure function  
 1440  $F_2^{(\pi N)}(x, \Delta|\mathbf{k}|, \Delta\theta_{p'})$  on the pion structure function parametrization was also studied using  
 1441 the GRV parametrization [77] of the pion parton distribution functions as compared with  
 1442 the MRS parametrization [78] with different amounts of sea, ranging from 10% to 20%.  
 1443 The pion structure function parameterizations are all similarly constrained by the pion-  
 1444 nucleon Drell-Yan data at Fermilab at intermediate and large values of  $x$ . The variation  
 1445 in the computed semi-inclusive proton structure function from uncertainties in the pion  
 1446 distribution functions is therefore smaller than the uncertainties from the pion-nucleon  
 1447 vertex form factor dependence.

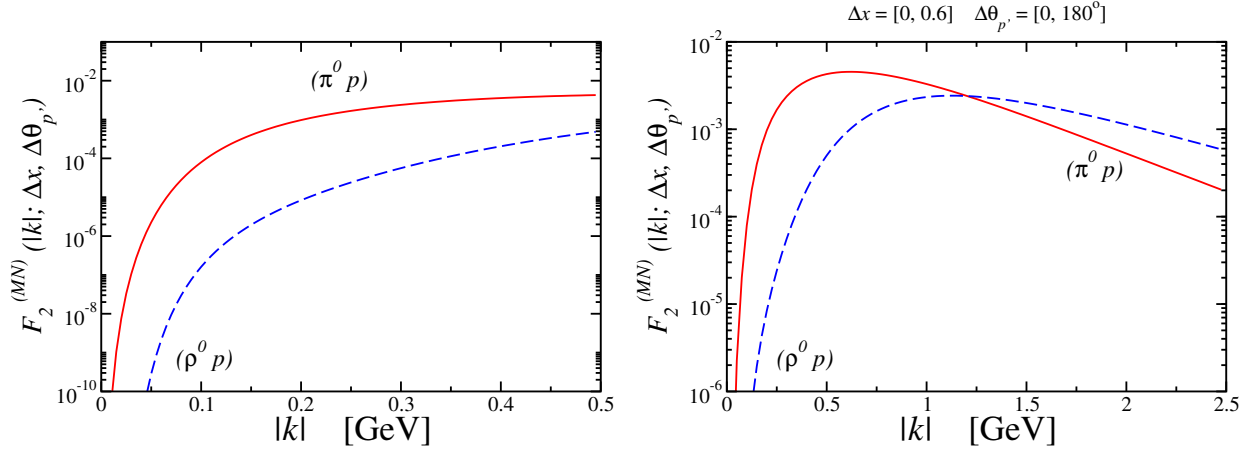


Figure 45: Semi-inclusive structure functions  $F_2^{(MN)}(|\mathbf{k}|; \Delta x, \Delta\theta_{p'})$  for the  $p \rightarrow M p$  process, with  $M = \pi^0$  (red solid) and  $M = \rho^0$  (blue dashed), as a function of the recoil proton momentum  $|\mathbf{k}|$ , integrated over  $\Delta x = [0, 0.6]$  and all angles  $\theta_{p'}$ . The left panel shows the function over the experimentally accessible range for  $|\mathbf{k}|$  up to 0.5 GeV, while the right panel shows the extended range up to  $|\mathbf{k}| = 2.5$  GeV.

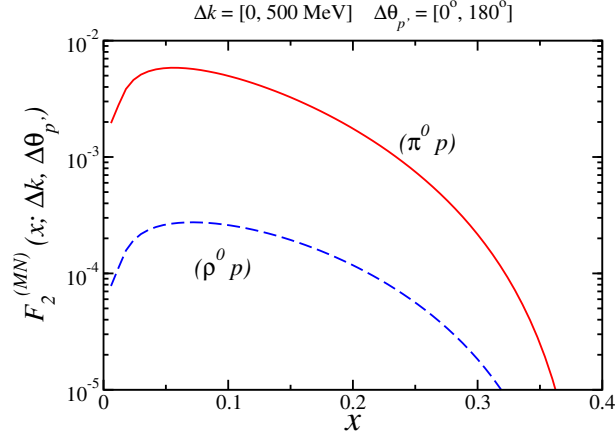


Figure 46:  $x$  dependence of the semi-inclusive structure function  $F_2^{(MN)}(x, \Delta|\mathbf{k}|, \Delta\theta_{p'})$  for  $p \rightarrow \pi^0 p$  (red solid) and  $p \rightarrow \rho^0 p$  (blue dashed), integrated over the momentum range  $\Delta|\mathbf{k}| = [0, 500]$  MeV and over all angles  $\theta_{p'}$ .

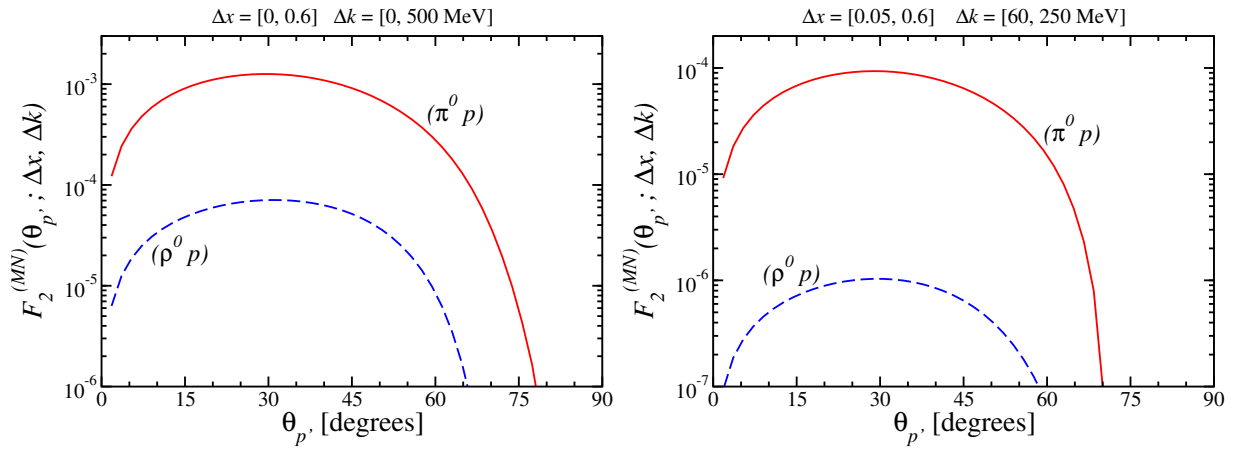


Figure 47:  $\theta_{p'}$  dependence of the tagged structure function  $F_2^{(\pi p)}(\theta_{p'}, \Delta x, \Delta|\mathbf{k}|)$  for neutral exchange in  $p \rightarrow \pi^0 p$  (red, solid) and  $p \rightarrow \rho^0 p$  (blue, dashed). The left panel plots the more inclusive integration ranges  $\Delta x = [0, 0.6]$  and  $\Delta|\mathbf{k}| = [0, 500]$  MeV, whereas the right panel show the same, but for the more constrained integration ranges  $\Delta x = [0.05, 0.6]$  and  $\Delta|\mathbf{k}| = [60, 250]$  MeV, appropriate for the proposed measurement.

## References

- 1448
- 1449 [1] Frisch and Stern, Zeits. f. Physik 85, 4 (1933); Estermann and Stern, Zeits. f. Physik  
1450 85, 17 (1933).
- 1451 [2] E. Fermi, L. Marshall, Phys.Rev. 72 1139-1146 (1947).
- 1452 [3] J.D. Sullivan, Phys. Rev. **D5**, 1732 (1972).
- 1453 [4] J. Speth and A.W. Thomas, Adv. Nucl. Phys. 24, 83 (1998).
- 1454 [5] P.L. McGaughey, J.M. Moss, and J.C. Peng, Ann. Rev. Nucl. Part. Sci. 49, 217  
1455 (1999).
- 1456 [6] S. Kumano, Phys. Rep. 303, 183 (1998).
- 1457 [7] A.W. Thomas, Phys. Lett. 126B, 97-100 (1983).
- 1458 [8] NMC Collaboration, P. Amaudruz et al, Phys. Rev. Lett. **66**, 2712 (1991); P. Amaudruz  
1459 *et al.*, Phys. Rev. **D 50**, R1 (1994)
- 1460 [9] K. Gottfried, Phys. Rev. Lett. **18**, 1174 (1967).
- 1461 [10] A. Baldit *et al*, Phys. Lett. **B 332**, 244 (1994).
- 1462 [11] E866 Collaboration, E. A. Hawker *et al.*, Phys. Rev. Lett. **80**, 3715 (1998).
- 1463 [12] E866 Collaboration, J. C. Peng *et al.*, Phys. Rev. **D 58**, 092004 (1998).
- 1464 [13] E866 Collaboration, R. S. Towell *et al.*, Phys. Rev. **D 80**, 3715 (1998).
- 1465 [14] HERMES Collaboration, K. Akerstaff *et al.*, Phys. Lett. **B 464**, 123 (1999).
- 1466 [15] F. M. Steffens and A. W. Thomas, Phys. Rev. **C55**, 900 (1997).
- 1467 [16] S. Kumano, Phys. Rep. **303**, 183 (1998).
- 1468 [17] J. P. Speth and A. W. Thomas, Adv. Nucl. Phys. **24**, 83 (1998).
- 1469 [18] G. T. Garvey and J. C Peng, Prog. Part. Nucl. Phys. **47**, 203 (2001).
- 1470 [19] R. Holt and C. Roberts, Rev. of Mod. Phy. **82**, 2991 (2010).
- 1471 [20] S. C. Pieper and R. B. Wiringa, Ann. Rev., Nucl. Part. Sci. **51**, 53 (2001).
- 1472 [21] R. B. Wiringa, Phys. Rev. **C73**, 034317 (2006).
- 1473 [22] P. Maris, C. D. Roberts, P. C. Tandy, Phys. Lett. **B420**, 287 (1998).
- 1474 [23] J. S. Conway *et al.*, Phys Rev. D **39**, 39 (1989).
- 1475 [24] J. Badier *et al.*, Z. Phys. **C18**, 281 (1983).

- 1476 [25] B. Betev *et al.*, Z. Phys. **C28**, 9 (1985).
- 1477 [26] M. B. Hecht, C. D. Roberts, and S. M. Schmidt, Phys. Rev. **C63**, 025213 (2001).
- 1478 [27] HI Collaboration, C. Adloff *et al.*, Eur. Phys. J. **C6**, 587 (1999); V. Andreev *et al.*,  
1479 arxiv:1312.4821.
- 1480 [28] G. R. Farrar and D. R. Jackson, Phys. Rev. Lett. **35**, 1416 (1975).
- 1481 [29] X. Ji, J.-P. Ma, and F. Yuan, Phys. Lett. **B610**, 247 (2005).
- 1482 [30] S. J. Brodsky, M. Burkardt, and I. Schmidt, Nucl. Phys. **B441**, 197 (1995).
- 1483 [31] P. Maris and C. D. Roberts, Int J. Mod. Phys. **E12**, 297 (2003).
- 1484 [32] J. C. R. Bloch, C. D. Roberts, S. M. Schmidt, A. Bender, and M. R. Frank Phys  
1485 Rev. **C60**, 062201 (1999).
- 1486 [33] J. C. R. Bloch, C. D. Roberts, and S. M. Schmidt, Phys Rev. **C61**, 065207 (2000).
- 1487 [34] T. Frederico and G. A. Miller, Phys. Rev, **D50**, 210 (1994).
- 1488 [35] A. Szczepaniak, C.-R. Ji, and S. R. Cotanch, Phys. Rev. **D49**, 3466 (1994).
- 1489 [36] T. Shigetani, K. Suzuki, and H. Toki, Phys. Lett. **B308**, 383 (1993).
- 1490 [37] R. M. Davidson, and E. Ruiz Arriola, Phys. Lett. **B348**, 163 (1995).
- 1491 [38] H. Weigel, E. Ruiz Arriola, and L. P. Gamberg, Nucl. Phys. **B560**, 383 (1999).
- 1492 [39] W. Bentz, T. Hama, T. Matsuki, and K. Yazaki, Nucl. Phys. **A651**, 143 (1999).
- 1493 [40] S. D. Drell, and T.-M. Yan, Phys. Rev. Lett **24**, 181 (1970).
- 1494 [41] G. B. West, Phys. Rev. Lett. **24**, 1206 (1970).
- 1495 [42] W. Melnitchouk, Eur. Phys. J. **A17**, 223 (2003).
- 1496 [43] K. Suzuki and W. Weise, Nucl. Phys. **A634**, 141 (1998).
- 1497 [44] Nikolaev *et al.*, Phys. Rev. **D60**, 014004 (1999).
- 1498 [45] See, for example, Hall A PR01-110 and Hall B LOI-01-001.
- 1499 [46] T. J. Hobbs et al., "A study of fracture functions for semi-inclusive electroproduction  
1500 of low-momentum baryons" (2014, in preparation), arXiv:1411.2216.
- 1501 [47] H. Holtmann, A. Szczurek and J. Speth, Nucl. Phys. **A 596**, 631 (1996).
- 1502 [48] W. Melnitchouk and A. W. Thomas, Z. Phys. A **353**, 311 (1995).
- 1503 [49] Z. F. Ezawa, Nuovo Cim. **A 23**, 271 (1974).

- 1504 [50] L. Chang, C. Mexrag, H. Moutarde, C. D. Roberts, J. Rodriguez-Quintero, P. C.  
1505 Tandy, Phys. Lett. **B420**, 267 (2014).
- 1506 [51] C. Merzag, L. Chang, H. Moutarde, C. D. Roberts, J. Rodriguez-Quintero, F.  
1507 Sabatie, S. M. Schmidt, arXiv:1411.6634, Phys. Lett. **B741**, 190 (2015).
- 1508 [52] C. D. Roberts, private communication.
- 1509 [53] B.Z. Kopeliovich, I.K. Potashnikova, B. Povh, Ivan Schmidt, Phys.Rev. **D85**, 114025  
1510 (2012).
- 1511 [54] Yu. M. Kazarinov *et al.*, Sov. Phys. JETP **43**, 598 (1976).
- 1512 [55] U. D' Alesio and H. J. Pirner Eur. Phys. J. A **7**, 109 (2000).
- 1513 [56] V. Stoks Nucl. Phys. A **629**, 205c (1998); V. Stoks and Th. A. Rijken, Phys. Rev. C  
1514 **59**, 3009 (1999).
- 1515 [57] K. Golec-Biernat, J. Kwiecinski and A. Szczurek, Phys. Rev. **D56**, 3955 (1997).
- 1516 [58] B. Kopeliovich, B. Povh and I. Potashnikova, Z. Phys. **C73**, 125 (1996).
- 1517 [59] K.A. Olive *et al.* (Particle Data Group), Chin. Phys. **C38**, 090001 (2014).
- 1518 [60] T. Hobbs, W. Melnitchouk, private communication
- 1519 [61] F. Sauli, Nucl. Instrum. Meth. **A386**, 531 (1997).
- 1520 [62] Gianfranco Morello, talk at Exploring Hadron Structure with Tagged Structure Func-  
1521 tions workshop at Jefferson Lab (2014).
- 1522 [63] S.K. Das *et al.*, Nucl. Instrum. Meth. A **625**, 39-42 (2011).
- 1523 [64] A. Sharma and F. Sauli, Nucl. Instrum. Meth. A **334**, 420 (1993); Y. Assran and A.  
1524 Sharma, Arxiv:1110.6761 (2011).
- 1525 [65] M. J. French *et al.*, Nucl. Inst. and Meth. **A466**, 359 (2001).
- 1526 [66] Dead-timeless Read-out Electronics ASIC for Micromegas.
- 1527 [67] L. W. Whitlow, E. M. Riordan, S. Dasu, S. Rock and A. Bodek, Phys. Lett. B **282**,  
1528 475 (1992).
- 1529 [68] S. Tkachenko *et al.* [CLAS Collaboration], Phys. Rev. C **89**, 045206 (2014).
- 1530 [69] D.E. Wiser, Ph.D. Thesis, University of Wisconsin-Madison (1977) (unpublished).
- 1531 [70] B. A. Mecking *et al.*, Nucl. Inst. and Meth. **A503**, 513 (2003).
- 1532 [71] S. Agostinelli *et al.*, Nuclear Instruments and Methods in Physics Research A 506,  
1533 (2003), p.250.

- 1534 [72] Geant-4 Physics Reference Manual, [http://geant4.cern.ch/support/](http://geant4.cern.ch/support/userdocuments.shtml)  
1535 [userdocuments.shtml](http://geant4.cern.ch/support/userdocuments.shtml).
- 1536 [73] *Applications of the Photonuclear Fragmentation Model to Radiation Protection Prob-*  
1537 *lems*, P. V. Degtyarenko, computer code DINREG, Proc. SATIF2, CERN, Oct. 1995
- 1538 [74] *Modeling single arm electron scattering and nucleon production from nuclei by GeV*  
1539 *electrons*, J. W. Lightbody and J. S. O'Connell, Computers in Physics 2, (1988),  
1540 p.57.
- 1541 [75] J.J. Kelly, Phys. Rev. C 70, (2004), p.068202.
- 1542 [76] V. Sapunenko, *et al.*, Nucl. Instr. and Meth. A, to be submitted.
- 1543 [77] M. Glück, E. Reya, A. Vogt, Z. Phys. C **53**, 651 (1992).
- 1544 [78] A. D. Martin, R. G. Roberts, W. J. Stirling and P. J. Sutton, Phys. Rev. D **45**, 2349  
1545 (1992).